IPP-Report

Max-Planck-Institut für Plasmaphysik

Steffen Potzel

Experimental classification of divertor detachment

IPP 10/44
Dezember, 2012

Experimental classification of divertor detachment

Von der Universität Bayreuth
zur Erlangung des Grades eines
Doktors der Naturwissenschaften (Dr. rer. nat.)
genehmigte Abhandlung

von

Steffen Potzel

aus Kulmbach

1. Gutachter: Prof. Dr. Michael Kaufmann
2. Gutachter: Prof. Dr. Arthur Peeters

Tag der Einreichung: 15. Mai 2012
Tag des Kolloquiums: 10. Juli 2012

Abstract

Avoiding damage of the divertor material by keeping the power load below a certain threshold is a major challenge for the operation of future fusion devices such as ITER. For Tungsten, the foreseen ITER divertor target material, the power load must be kept below $5\,\mathrm{MW/m^2}$ in continuous operation. This can in ITER only be achieved with the plasma being detached or partially detached from the divertor.

Divertor detachment is characterized by a strong reduction of the ion flux to the target. With a reduction of the temperature, achieved by increasing the main plasma density or by seeding additional impurities, volumetric processes such as charge exchange collisions and recombination become dominant. These processes lead to a strong reduction of the ion flux and plasma pressure in front of the divertor target. Although the single physical mechanisms leading to detachment seem to be understood, it was not yet possible to theoretically simulate detachment correctly with respect to experimental observations. This means that some understanding of this process is still missing.

In the detached regime, the region of high electron density is retracted from the target and a knowledge of the electron density distribution in the divertor volume is necessary to understand the detachment process. In this context, a diagnostic determining the electron density in the divertor volume, based on the spectroscopic measurement of the Stark broadening of the Balmer lines, has been installed at ASDEX Upgrade. Initial problems with reflected stray-radiation have been solved and first measurements were successfully compared for consistency with other diagnostics.

The detachment process was then investigated with an extensive set of density ramp discharges with different heating powers, fuelling species and magnetic field directions. The density measurements in the divertor volume were combined with all other available divertor diagnostics and a consistent picture of the detachment process was obtained. It was found that detachment is not a continuous evolution but undergoes three different states. During one of these states radiative fluctuations close to the X-point and high densities far away from the separatrix occur. This is a situation which is not described by present day theoretical models. Furthermore, it was shown that the conditions of both the inner and outer divertor are strongly coupled and that the inner divertor even influences the outer divertor. This effect was not shown yet, neither experimentally nor by theoretical simulations.

It was further discovered how additional puffing of nitrogen into the divertor, which removes power via radiation, changes the detached divertor conditions and may even change the confined plasma conditions. The effect of an additional magnetic perturbation field on the detachment process has also been investigated. Finally, an unstable situation was found, during which the divertor plasma oscillates between two detachment states back and forth.

Zusammenfassung

Eine große Herausforderung für den Betrieb zukünftiger Fusionsreaktoren wie ITER ist eine Beschädigung des Divertors zu verhindern. Dies kann nur gewährleistet werden, indem der Leistungsfluss auf das Wandmaterial auf einen tolerierbaren Wert reduziert wird. Im Falle des für ITER vorgesehenen Divertormaterials Wolfram beträgt der Grenzwert des Leistungsflusses bei kontinuierlichem Betrieb $5\,\mathrm{MW/m^2}$. In ITER kann dies nur erreicht werden wenn das Plasma von den Aufprallplatten des Divertors losgelöst, detached, ist.

Divertor Detachment ist durch eine starke Reduktion des Ionenflusses auf die Divertorplatten charakterisiert. In dem, durch Erhöhung der Plasmadichte oder Zufuhr von Verunreinigungen, die Temperatur reduziert wird, gewinnen volumetrische Prozesse, wie Ladungsaustauschstöße oder Rekombination, an Bedeutung. Diese Prozesse führen vor der Divertorwand zu einer starken Reduktion des Ionenflusses und des Plasmadrucks. Obwohl die einzelnen physikalischen Mechanismen, die zu Divertor Detachment führen, verstanden zu sein scheinen, war es bis jetzt noch nicht möglich, experimentell beobachtete Vorgänge des Detachments mit Hilfe theoretischer Simulationen zu reproduzieren. Das lässt darauf schließen, dass die physikalischen Vorgänge beim Übergang zum Detachment noch immer nicht vollständig verstanden sind.

Die Region hoher Elektronendichte ist beim Detachment nicht mehr direkt vor der Divertorwand. Um den Vorgang des Detachments zu verstehen, ist die Kenntnis über die Verteilung der Elektronendichte im Divertor unabdingbar. Deshalb wurde an ASDEX Upgrade eine Diagnostik installiert, mit der man die Elektronendichte im Divertor mit Hilfe der spektroskopischen Messung der Stark Verbreiterung der Balmer Linien bestimmen kann. Anfängliche Probleme durch reflektierte Streustrahlung wurden behoben und die Konsistenz erster Messungen mit anderen Divertor Diagnostiken wurde erfolgreich bestätigt.

Der Vorgang des Detachments wurde dann mittels einer umfangreichen Serie von Entladungen mit Dichterampen untersucht, bei der die Heizleistung, die Ionen Spezies und die magnetische Feldrichtung variiert wurden. Die Dichtemessungen wurden dabei mit allen, zu Verfügung stehenden, Divertor Diagnostiken kombiniert und ein konsistentes Bild des Detachment Vorgangs wurde gewonnen. Dabei konnte festgestellt werden, dass der Vorgang des Detachments nicht kontinuierlich verläuft, sondern in drei verschiedene Phasen unterteilt werden kann. Während einer dieser Phasen treten nahe des X-Punktes hoch-frequente Fluktuationen der Strahlung und hohe Elektronendichten weit entfernt von der Separatrix auf. Diese Situation kann mit gegenwärtigen theoretischen Modellen nicht erklärt werden. Es wurde außerdem gezeigt, dass die Bedingungen im inneren und äußeren Divertor stark gekoppelt sind. Dieser Effekt wurde bisher weder experimentell noch mittels theoretischer Simulationen gezeigt.

Weiterhin wurde gezeigt, wie die Zufuhr von Stickstoff, wodurch Leistung im Divertor abgestrahlt wird, die Eigenschaften des detachten Divertorplasmas und eventuell auch des eingeschlossenen Haupt-Plasmas verändert. Ferner wurde der Einfluss eines zusätzlichen magnetischen Störfeldes auf den Vorgang des Detachments untersucht. Schließlich wurde eine instabile Situation entdeckt, während der das Divertor Plasma zwischen zwei Detachment Phasen oszilliert.

Contents

Chapter 1

Introduction

1.1 Nuclear fusion

The combination of two light atoms into a heavier one is called *nuclear fusion*. As the mass of the final atom is smaller than the sum of the masses of the two initial atoms, energy is released by this process according to Einsteins formula $E = mc^2$. Nuclear fusion is the process which produces the energy in stars. Here, in a so-called proton-proton chain reaction four protons fuse into one He nucleus. The net equation of this reaction is:

$$4\mathrm{p} \rightarrow {}^{4}_{2}\mathrm{He} + 2e^{+} + 2\nu_e + 26.7\,\mathrm{MeV} \tag{1.1}$$

In addition to the helium nucleus, two positrons, two neutrinos ν_e and an energy of 26.7 MeV are produced. This reaction is limited by the weak force combination of p-p, for which rate coefficients are small ($\langle \sigma v \rangle \approx 10^{-45}\,\mathrm{m^3 s}$). This makes the fusion process very slow.

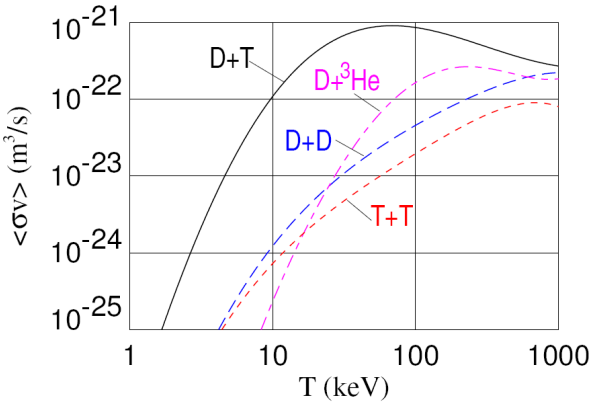

Figure 1.1: Rate coefficients for various fusion reactions versus ion temperature.

In order to realize a fusion power plant on earth, a different fusion reaction must be

employed. In Figure 1.1 rate coefficients for several fusion reactions are shown. The reaction with the highest rate coefficient is the fusion of deuterium and tritium:

$$\mathrm{D} + \mathrm{T} \rightarrow {}^{4}_{2}\mathrm{He} + n + 17.6\,\mathrm{MeV} \tag{1.2}$$

This reaction implies the resonant production of an excited ${}^{5}_{2}$He nucleus, which is the reason for the high rate coefficient. The resulting ${}^{4}_{2}$He nucleus (α-particle) and the neutron n carry approximately 3.6 MeV and 14.1 MeV of the released energy, respectively. Tritium, which is radioactive with a half-life of 12.3 years, is naturally not available and must be bred from lithium via the following processes:

$$n + {}^{6}_{3}\mathrm{Li} \rightarrow {}^{4}_{2}\mathrm{He} + \mathrm{T} + 4.8\,\mathrm{MeV} \tag{1.3}$$

$$n + {}^{7}_{3}\mathrm{Li} \rightarrow {}^{4}_{2}\mathrm{He} + \mathrm{T} + n' - 2.5\,\mathrm{MeV} \tag{1.4}$$

Natural lithium consists of 7.5% ${}^{6}_{3}$Li and 92.5% ${}^{7}_{3}$Li. Reaction 1.4 costs energy but produces another neutron. As deuterium and lithium are highly available all over the world, nuclear fusion can provide a nearly inexhaustible energy source which is free from CO_2 emission.

1.2 Magnetic confinement fusion - the tokamak

Due to the high temperatures necessary for the fusion reaction ($T = 10 - 100\,\mathrm{keV}$[1], Fig. 1.1), all atoms will be fully ionized, creating a plasma. This so-called fourth state of matter can be confined by a magnetic field. The plasma electron and ions will gyrate around the magnetic field lines, which strongly reduces the transport perpendicular to the field lines.

In order to avoid losses at the end of the field line, the field lines must be closed. This is achieved by bending them into a torus, see Figure 1.2. The principal confinement field, which is in the toroidal direction, B_t[2], is produced by toroidal field coils. In a toroidal magnetic field, however, the magnetic field decays radially proportional to $1/R$, with the major radius R being the distance from the symmetry axis. This imposes a particle drift parallel to the torus axis caused by the $\vec{B} \times \nabla\vec{B}$ force, which is in opposite direction for electrons and ions. Hence, an electric field parallel to the torus axis occurs and the resulting $\vec{E} \times \vec{B}$ drift forces the particles to move outwards. This configuration would therefore not be in equilibrium. To compensate for this effect, an additional poloidal magnetic field B_p is applied. The field lines, which form nested flux surfaces, then

[1] Throughout this thesis, the temperature is expressed in eV, with $1\,\mathrm{eV} = 11.600\,\mathrm{K}$. Otherwise SI units are used.

[2] It is common in plasma physics to denote $\vec{B} = \nu_0\vec{H}$ as the magnetic field.

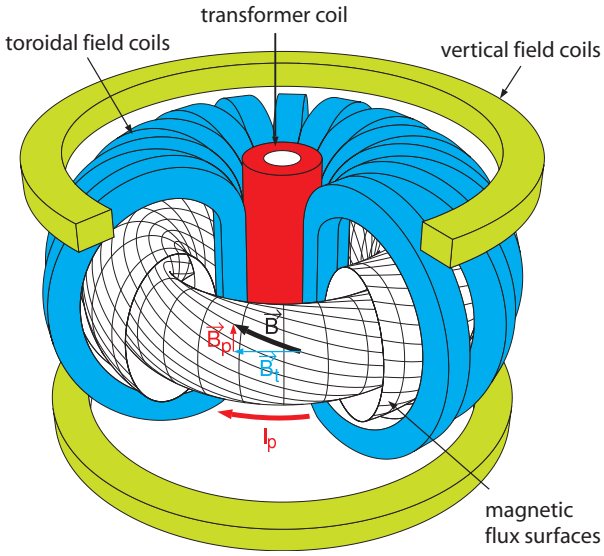

Figure 1.2: Schematic view of the tokamak principle.

wind helically around the torus (Fig. 1.2) and the undesirable drifts are compensated for. In the *tokamak*[3] configuration, the poloidal magnetic field is produced by driving a toroidal current in the plasma. This plasma current is inductively driven by a central transformer coil, see Figure 1.2. Vertical field coils are used for plasma shaping and position control. The disadvantage of this configuration is that due to the finite plasma resistivity, the transformer current must be ramped continuously, allowing only pulsed operation. Non-inductive current drive mechanisms may overcome this problem in the future.

Another configuration imposing a poloidal component to the magnetic field is the *stellarator*. Here, B_p is produced by using a non-planar complex magnetic coil configuration. Contrary to the tokamak, axis symmetry is broken by this configuration.

The Garching Branch Institute of the Max-Planck-Institut für Plasma Physik, IPP, where this thesis was carried out, investigates magnetic confinement fusion with the tokamak concept[4]. Therefore, the focus in the following is only on the tokamak configuration. The basic parameters of the IPP tokamak ASDEX[5] Upgrade, AUG, are listed in table 1.1.

In order to gain net power from the fusion process, the heating of the plasma must be provided mainly by the produced α-particles (eq. 1.2). This implies that the α-particles have to be confined in the plasma long enough to transfer their energy to the plasma electrons and ions. The situation where fusion becomes self-sustained, i.e the

[3]Russian for toroidal chamber with magnetic field coils

[4]The Greifswald Branch Institute of IPP investigates magnetic confinement fusion with the stellarator concept

[5]German for axially symmetric divertor experiment

Table 1.1: Basic parameters of ASDEX Upgrade.

Major radius R_0	1.65 m
Minor radius a	0.5 m
Toroidal magnetic field B_t	≤ 3.1 T
Plasma current I_p	0.4 MA-1.6 MA
Pulse duration	≤ 10 s
Plasma heating	NBI 20 MW
	ECRH 4 MW
	ICRH 8 MW
	ohmic ≤ 1 MW
Main plasma density n	$\leq 2 \cdot 10^{20}\,\mathrm{m}^{-3}$
Main plasma Temperature T	≤ 25 keV
Energy confinement time τ_E	≤ 0.2 s

plasma is heated only by the α-particles, is called ignition. One can define the so-called *triple product* (see e.g. [1]) which must fulfil the following inequality in order to achieve ignition:

$$n_e T_e \tau_E \geq 5 \cdot 10^{21}\,\mathrm{keV\,s\,m^{-3}} \tag{1.5}$$

where τ_E is the energy confinement time and n_e, T_e is the electron density and temperature, respectively.

The ratio of kinetic to magnetic pressure β, which is proportional to $n_e T_e / B^2$, can not exceed a certain limit [2] for stability reasons. The magnetic pressure, which corresponds to the magnetic field strength, is limited by engineering constraints. Thus, the achievable kinetic pressure in a reactor, which is proportional to $n_e T_e$, is limited. In order to fulfil the inequality 1.5, the energy confinement time has to be sufficiently large. The volume of the fusion plasma grows with the third power of the radius of the tokamak, whereas the surface, through which energy is lost, grows with the second power. This makes it necessary to go to larger size devices in order to reach high confinement times. It is expected that, for a fusion reactor to achieve ignition it must have a major radius of about 10 m. The largest present-day fusion experiment, the Joint European Torus, JET, in England has a major radius of about 3 m.

Therefore, a world wide experiment named ITER[6] [3] was planned, having a major radius of 6.2 m. The members of the ITER project are China, Europe, India, Japan, Russia, South Korea and USA and the construction of ITER has recently started in Cadarache,

[6]International Thermonuclear Experimental Reactor

France. The auxiliary heating systems will provide a power of about 50 MW and the pulse duration will last ≥ 500 s. The main goal of ITER is the demonstration of gaining net power, i.e. that the power produced by the fusion process, P_f, exceeds the power which is needed for plasma heating, P_h. ITER is designed to achieve a fusion power of about 500 MW, which results in an energy amplification factor of $Q = P_f/P_h \geq 10$. The research activities of ASDEX Upgrade are focused on questions related to the operation of ITER, meaning the plasma shape, the heating power with respect to the radius, P/R, and the divertor design, discussed in the next section, of ASDEX Upgrade are similar to ITER.

1.3 Divertor configuration

As the magnetic confinement of the plasma is not ideal, plasma particles will reach the surrounding vacuum vessel and erode the wall material. The *sputtered* impurities enter the plasma, where they dilute and cool it. This effect can be reduced with the *divertor* configuration. Figure 1.3 shows the poloidal cross section of the magnetic flux surfaces with the divertor configuration of ASDEX Upgrade.

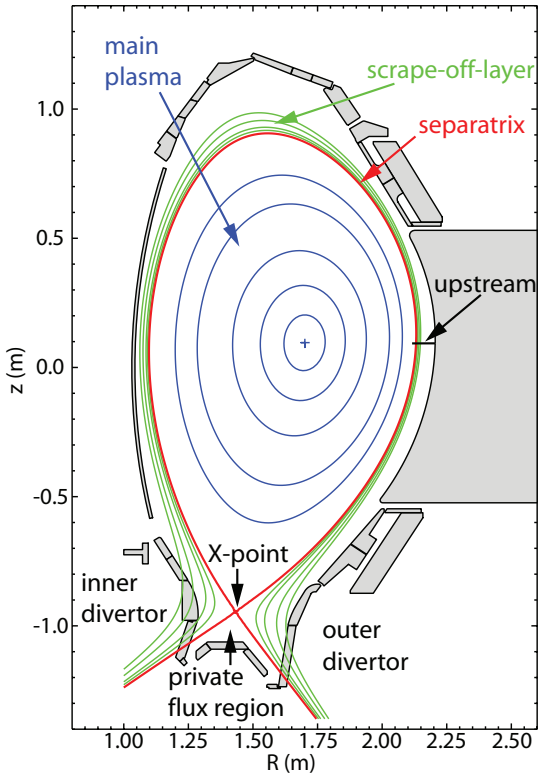

Figure 1.3: Poloidal cross section of the magnetic flux surfaces in an ASDEX Upgrade divertor configuration.

With additional coils in the toroidal direction, a *separatrix* is formed, which separates

the closed flux surfaces of the *confined* or *main plasma* from the open flux surfaces in the so-called *scrape-off-layer*, SOL. The region below the X-point and the separatrix is called the *private flux region*, see Figure 1.3. Plasma particles escaping from the main plasma into the SOL will travel along the field lines as the parallel particle and heat transport is much stronger than the perpendicular one (see chapter 2), and impact the vessel surfaces in the remote area below the X-point which is called *divertor*. The points where the separatrix intersects the surface are referred to as the *strike points* and the area in the vicinity of the strike points is referred to as the *divertor target*. It is helpful to define here the following quantities: the *upstream* position is the region where the plasma particles enter the SOL, usually taken at the outer mid-plane position (see Fig. 1.3); the *connection length* L_c is the distance from the upstream position along the field lines to the target. Due to the helicity of the magnetic field lines (especially at the vicinity of the X-point the toroidal magnetic field is much larger than the poloidal one), L_c is much larger than it might be expected from the poloidal projection of Figure 1.3. In ASDEX-Upgrade, L_c is typically of the order of 50 m.

With the divertor configuration, the impurities are mainly eroded from the divertor walls where most of them are pumped out. Their probability of reaching the main plasma is strongly reduced compared to the non-divertor, circular magnetic configuration called limiter configuration, and a cleaner main plasma can be achieved.

In the following, unless explicitly mentioned, plasma ions and neutrals are assumed to be of the main fuelling species deuterium[7]. The plasma ions, impacting the divertor target, will form neutrals on the surface and release other neutrals from the wall. These released neutrals will enter the SOL where they are ionized and flow back to the target. This particle cycle is called *recycling*. The only possibility to reduce the power, which is deposited on the plasma facing walls, is to remove power in the SOL via radiation. Based on the recycling process, a reduction of the power flux density to the targets can be achieved with the divertor configuration. When the main plasma density is increased while keeping the heating power constant, the level of recycling increases. Due to the remote structure of the divertor, the recycled neutrals will be ionized in front of the divertor targets and remove power via radiation. A similar effect is achieved when puffing (also called *seeding*) additional impurities into the divertor plasma via gas valves. As a consequence of this power removal, the density in front of the targets increases and the temperature drops. If the temperature is sufficiently low, CX collisions between ions and neutrals become dominant with respect to the ionization. This process removes momentum from the plasma and therefore reduces the ion flux to the target. The plasma flow velocity towards the target is also decreased, which, in combination with the low temperatures, increases the probability of ions recombining before reaching the target.

[7] As tritium is radioactive and the physics of D-T and D-D plasmas are similar, nowadays fusion experiments are typically done with deuterium only as main ion species

The plasma is then *detached* from the target and the power flux to the target, which is proportional to the ion flux to the target, is strongly reduced.

The reduction of the power flux density with the divertor configuration allows for higher heating powers. At ASDEX, the high confinement mode, *H-mode*, was discovered in 1982 [4]. The H-mode is characterized by strong reduction of the perpendicular particle and energy transport within a narrow region of the order of a few centimetres inside the separatrix. This results in steeper density and temperature gradients and in a better energy confinement with respect to the low confinement mode, *L-mode*. The H-mode is achieved when the heating power exceeds a certain threshold, which depends amongst others on the main plasma density [5]. The H-mode regime, however, comes along with the occurrence of so-called *Edge Localized Modes* [6], which repetitively expel particles and energy from the main plasma into the SOL.

1.4 Aim of this work

Carbon, a widely used divertor target material, has the disadvantage of forming hydrocarbons which are stored in the material. The amount of radioactive tritium stored in the wall material would therefore rapidly reach unacceptable values. Thus, the foreseen ITER divertor target material is tungsten. In order to ensure a safe operation of the ITER divertor in terms of damage on the material, i.e. avoiding tungsten melting, the peak power load must be kept below $q = 5\,\mathrm{MW/m^2}$ in continuous operation. In order to achieve the necessary low target power densities, the ITER divertor must be operated in the detached regime [7]. Therefore, one must be able predict the ITER divertor performance, which is only possible with two dimensional code simulations. Although the physical mechanisms leading to detachment seem to be understood, neither a qualitative nor a quantitative agreement between theoretical modelling and experimental observations of divertor detachment has been achieved yet [8].

This work is an experimental investigation of the detachment process. The plasma density and temperature in the divertor are routinely measured at ASDEX Upgrade by Langmuir probes embedded in the divertor targets. These probes provide a local determination of density and temperature in front of the target. Since the region of high electron density is retracted from the target in detached divertor plasmas, information of the value and distribution of the electron density in the divertor volume itself is necessary. In this context, a new diagnostic has been built and verified (by comparison with other diagnostics) at ASDEX Upgrade, which is based on the spectroscopic measurement of the Stark broadening of the Balmer lines. This effect is proportional to the density and can, therefore, be used as a measurement of this parameter.

The temporal evolution of the detachment process has been investigated in the inner and

outer divertor regions simultaneously. The density measurements in the divertor volume were compared to several other parameters, such as e.g. the ion flux to the target and the total radiation distribution in the divertor. With this, a consistent picture of divertor detachment in ASDEX Upgrade was obtained.

This thesis is structured as follows. In chapter 2, an introduction to divertor physics is given. The atomic processes valid in a plasma, which for example determine the radiance of a spectral line, are discussed chapter 3. Also in this chapter, a method is derived which enables the determination of hydrogen flux densities in attached and detached conditions by measuring the radiance of a Balmer line. Thereafter, in chapter 4, the theory of Stark broadening in a plasma is reviewed, the setup of the new diagnostic is presented, and initial measurements are compared with other diagnostics for consistency. The experimental results concerning divertor detachment are presented in chapter 5. These results are summarized and discussed in chapter 6 and, finally, conclusions are given in chapter 7.

Chapter 2

Divertor physics

In this chapter an introduction to the physics of divertor plasmas is given which is based on extensive reviews given by [9, 10, 11]. In section 2.1 the interaction of the plasma with the facing surfaces[1] is discussed. After this, in section 2.2 the different divertor operating regimes are described in a simplified picture. Extensions to this simple picture will be given in section 2.3. Finally, in section 2.4 the current understanding of the detached divertor regime, which is the main focus of this work, will be summarized.

2.1 Plasma-wall transition, the *sheath*

Plasma particles and energy, diffusing out of the confined plasma, will be transported along the open magnetic field lines in the SOL until they finally hit the divertor targets. In section 2.1.1 the effects of the particle flux on the target will be introduced. An expression for the heat, which is deposited on the target, will be derived in section 2.1.2.

2.1.1 Particle outflux from the plasma to the surface

In a simplified picture, the plasma away from the surface is quasineutral ($n_e = n_i$) and the plasma potential is $V_p = 0$. Assuming thermal equilibrium, the thermal velocity of the electrons is much higher compared to the ions, since $v_e = \sqrt{m_i/m_e}\, v_i$. Therefore, the surface will receive a higher flux of electrons and become negatively charged, thus lowering the potential on the surface. As a consequence, the surface will attract the ions and repel the electrons. Within a narrow region close to the surface, called the *sheath*, quasineutrality is broken and $n_i > n_e$. The width of the sheath is of the order of one Debye length, $\lambda_D = \sqrt{\epsilon_0 k_B T_e / e^2 n_e}$, which, for typical AUG parameters is of the order of 10^{-5} m. The potential distribution is described by the Poisson equation:

[1] If not explicitly mentioned, *surface* is in the following referred to as the surface of the plasma facing wall.

$$\frac{\mathrm{d}^2 V}{\mathrm{d}x^2} = -\frac{e}{\epsilon_0}\left(n_i - n_e\right) \tag{2.1}$$

The velocity of the ions which are accelerated by the potential drop is:

$$v_i = -\sqrt{2eV/m_i} \tag{2.2}$$

With the continuity equation $j_i = n_i v_i = \text{const}$, the ion density can be written as:

$$n_i = n_{i,s}\sqrt{\frac{V_s}{V}} \tag{2.3}$$

where $n_{i,s}$ and V_s are the ion density and the potential at the sheath entrance (at a distance of $\approx \lambda_D$ from the surface), respectively. The potential at the sheath entrance is, contrary to the upstream region (at a distance of $\gg \lambda_D$ from the surface), not zero anymore. The electrons, in contrast, are reflected by the potential in the sheath. The electron density is given by the Boltzmann relation:

$$n_e = n_{e,s}\exp\left[\frac{e(V - V_s)}{k_B T_e}\right] \tag{2.4}$$

At the sheath entrance quasineutrality still holds and $n_{i,s} = n_{e,s} = n_s$. Inserting equations 2.3 and 2.4 into equation 2.1 and making a Taylor expansion at $x = x_s$ yields:

$$\frac{\mathrm{d}^2(V_s - V)}{\mathrm{d}x^2} \approx \frac{e n_s}{\epsilon_0}\left[\frac{e}{k_B T_e} - \frac{1}{2V_s}\right](V_s - V) \tag{2.5}$$

To get a non oscillatory physical solution for V, the expression in the brackets must be negative: $V_s \geq -(k_B T_e)/(2e)$. Combined with equation 2.2 this gives a constraint on the ion velocity at the sheath entrance:

$$v_{i,s} \geq \sqrt{\frac{k_B T_e}{m_i}} \tag{2.6}$$

For $T_i = 0$ this is the ion sound speed c_s, which is defined as:

$$c_s = \sqrt{\frac{Z k_B T_e + \alpha k_B T_i}{m_i}} \tag{2.7}$$

where Z is the ion charge and $\alpha = 1$ for isothermal flow, $\alpha = 5/3$ for adiabatic flow with isotropic pressure and $\alpha = 3$ for one dimensional adiabatic flow [12]. Hence, the ions are accelerated to at least sound speed at the sheath entrance. This constraint is called the Bohm criterion [13] which was also derived earlier by Langmuir [14]. Another consequence of equation 2.6 is, as mentioned above, that the potential at the sheath entrance is not zero, meaning that there is already a potential drop in the SOL upstream

of the sheath. Assuming no ion-neutral collisions, the so-called pre-sheath potential is, for isothermal flow, approximately:

$$V_s \approx -0.7 \frac{k_B T_e}{e} \tag{2.8}$$

This potential forces the ions to flow from upstream ($V = 0$) towards the divertor surfaces, the so-called *divertor sink action*. The pre-sheath potential V_s is small compared to the potential at the surface ($V_{surf} \approx -3 k_B T_e/e$ for typical divertor conditions) which is caused by the potential drop in the sheath. However, the particle and power outflow rate to the surface is determined entirely by V_s, thus by the forces in the plasma and not in the sheath. Finally the particle flux density on the surface is introduced:

$$\Gamma_s = n_{e,s} v_{e,s} = n_{e,s} c_s \tag{2.9}$$

As it is assumed that there is no particle source or sink in the sheath, the flux density is equal at the surface and the sheath entrance, $\Gamma_s = \Gamma_{surf}$.

It should be noted here that, due to the magnetic field present in a tokamak, a so-called *magnetic pre-sheath* exists in front of the sheath. This magnetic pre-sheath is formed due to the gyration of the charged plasma particles around the magnetic field lines together with non perpendicular incident angles of the field lines on the target. However, the above derived basic properties of the sheath are not changed by the presence of the magnetic pre-sheath [15].

2.1.2 Power deposited on the surface

Here, the power deposited on the surface by the plasma particles will be discussed. As the electron distribution function is Maxwellian, the electron power flux density at the surface can be calculated by integration over the velocity space:

$$q^e_{surf} = \int_0^{-\infty} \left(\frac{m_e v_x^2}{2} \right) v_x f_e(v_x)\, dv_x + k_B T_e = 2 k_B T_e \Gamma_s \tag{2.10}$$

The ions, however, are accelerated by the potential and therefore do not follow a Maxwellian distribution. With the assumption that the ion distribution is a Maxwellian distribution shifted by c_s, the ion power flux density can be calculated similarly:

$$q^i_{surf} = \left(\frac{5}{2} k_B T_i + \frac{m_i c_s^2}{2} \right) \Gamma_s = \frac{7}{2} k_B T_e \Gamma_s$$

here and in the following $T_e = T_i$ is assumed. In addition, the sheath and the pre-sheath transfer energy from the electrons to the ions by an amount of $|eV_{surf}|$ and $|eV_s|$,

respectively. The power density deposited on the plasma surface by electrons and ions can thus be written as:

$$\begin{aligned} q_{surf} &= q^e_{surf} + q^i_{surf} = \left(2k_BT_e + \frac{7}{2}k_BT_e + |eV_{surf}| + |eV_s|\right)\Gamma_s \\ &= \gamma k_BT_e\Gamma_s \end{aligned} \tag{2.11}$$

with the sheath heat transmission coefficient $\gamma \approx 2 + 3.5 + 3 + 0.7 \approx 9.2$. It should be noted that this is just a simplified derivation. If one includes other effects, such as e.g. secondary electron emission [15], there is a strong variation of γ. In ASDEX Upgrade, values of γ between 3 and 8 were found [16]. In a multi machine comparison, γ even varies between 2 and 11 [17].

The power density in equation 2.11 can be referred to as the kinetic energy deposited on the surface. In addition, incoming ions recombine on the surface with electrons to form neutral atoms and incoming neutrals will recombine on the surface with other neutrals to form molecules. These processes release the potential energy, or at least a significant fraction of it, as heat to the surface. For deuterium, the ionization energy is $E^{ion}_{pot} = 13.6\,\text{eV}$ and the molecular dissociation energy is $E^{diss}_{pot} = 4.5\,\text{eV}$. The total power density, including the kinetic and potential energy, $E_{pot} = E^{ion}_{pot} + E^{diss}_{pot} = 18.1\,\text{eV}$, deposited on the surface is then given by:

$$q_{tot} = (\gamma k_BT_e + E_{pot})\Gamma_s \tag{2.12}$$

From equation 2.12 it can be seen that a reduction of the temperature results in a decrease of the deposited power. In present experiments this is usually sufficient for safe operation in terms of melting or damaging the wall material. In larger scale devices such as ITER, however, the particle fluxes to the surface are predicted to be so high that the potential power deposited on the surface becomes important. Thus, for a safe operation not only the temperature but also the particle fluxes to the surface must be reduced. The question how a reduction of both parameters at given input power can be achieved, resulting in different divertor operating regimes, will be addressed in the following section.

2.2 Divertor operating regimes

The divertor plasma is usually described by a fluid approach. The use of a fluid approach is appropriate if the collisional mean-free-paths of electron and ion self-collisions, $\lambda_{ee,ii} \approx 10^{16}T^2_{e,i}/n_{e,i}$, are small compared to the characteristic scale length in the SOL, L_c. For typical AUG parameters ($n_e \approx 1 \cdot 10^{19}\,\text{m}^{-3}$, $T_e \approx 50\,\text{eV}$), $\lambda_{ee} \approx 2.5\,\text{m} \ll L_c \approx 40\,\text{m}$ and

the fluid approach is valid. Here, the plasma parameters such as density and temperature are described by the Fokker-Planck kinetic equation:

$$\frac{\partial f}{\partial t} + \vec{v} \cdot \nabla f + \frac{q}{m}(\vec{E} + \vec{v} \times \vec{B}) \cdot \nabla_{\vec{v}} = S(f) \tag{2.13}$$

where $S(f)$ describes particle sources and sinks due to ionization, recombination or interaction of plasma particles with impurities and $f(\vec{r}, \vec{v}, t)$ is the particle distribution function in position-velocity-time space. The fluid equations of the various plasma parameters, the so-called Braginskii equations [18], are derived by taking the velocity moments of equation 2.13 up to the third order. These result in a set of coupled, non linear differential equations which only can be consistently solved with sophisticated computer codes.

One of the most important processes in the SOL is the heat transport parallel to the field lines to the target. This transport is a combination of a conductive and a convective heat transport. The parallel electron heat flux density $q_{\parallel e}$, derived from the Braginskii equations, is given by:

$$q_{\parallel e} = \frac{5}{2} k_B T_e n_e v_e - \kappa_{0e} T_e^{5/2} \frac{\mathrm{d}T_e}{\mathrm{d}x} \tag{2.14}$$

where the first term on the right hand side describes the convective part and the second one the conductive part. The corresponding ion heat flux density is:

$$q_{\parallel i} = \left(\frac{1}{2} m_i v_i^2 + \frac{5}{2} k_B T_i \right) n_i v_i - \kappa_{0i} T_i^{5/2} \frac{\mathrm{d}T_i}{\mathrm{d}x} \tag{2.15}$$

The electron and ion heat conductivity coefficients, κ_{0e} and κ_{0i} respectively, were derived by Spitzer and Härm [19] and are given in [20] to be:

$$\kappa_{0e,i} = \frac{k_B}{\sqrt{m_{e,i}} \ln \Lambda \, e^4 Z} \tag{2.16}$$

It can be seen that $\kappa_{0i} \propto \sqrt{m_e/m_i}\, \kappa_{0e}$. Thus, the ion heat conduction can be neglected compared to the electron heat conduction, i.e. the power is conducted mainly by the electrons. Assuming $T_e \approx T_i$ and $n_e \approx n_i$, one can combine equations 2.14 and 2.15 and obtain the total heat flux density:

$$q_{\parallel} = \left(\frac{1}{2} m_i v^2 + 5 k_B T \right) n_e v - \kappa_{0e} T_e^{5/2} \frac{\mathrm{d}T_e}{\mathrm{d}x} \tag{2.17}$$

Another important process is that of plasma particle production and flow in the SOL. Plasma ions impacting the surface will release neutrals from the wall. These neutrals will be ionized in the plasma, providing a source of plasma particles. The resulting ions will flow back to the surface and release new neutrals. This particle cycle is called

recycling. The degree of recycling and the region where the ionization of the recycled neutrals occurs strongly affect the divertor plasma conditions. In the following section, simplified relations between upstream and target parameters will be derived with respect to the degree and location of the recycling. From now on, the focus is on the values at the sheath entrance, see section 2.1. These values are called the *target* parameters.

2.2.1 The low recycling regime

If the upstream density at a given heating power is sufficiently low, the divertor is in the low recycling regime and a model can be developed, linking upstream and target parameters, under the following simplified assumptions. The recycling level is low and the particle source due to the ionization of recycled neutrals is assumed to be negligible with respect to the main plasma particle source, i.e. it is assumed that the main plasma is the only particle source. It is further assumed, that the main plasma is the only power source, thus all power and particles enter the SOL at the upstream position s_{up}. Furthermore no cross field transport between different flux tubes is considered. The electrons and ions will flow from upstream due to the divertor sink action (the pre-sheath potential drop V_s, section 2.1.1) towards the target within a flux tube, reaching sound speed, c_s, at the target (see eq. 2.6 and eq. 2.7) and the heat is then convected to the targets. The heat transport to the target is limited only by the heat, which can be transmitted by the sheath. Therefore, this regime is also called the *sheath limited regime*. As a consequence of the heat being convected, the temperature along the field line is approximately constant (assuming $T_e = T_i = T$ and $n_e = n_i = n$):

$$T_u \approx T_t = T \tag{2.18}$$

Throughout this thesis, the indices u and t refer to as the values at the upstream position and target, respectively. With the assumption of no cross-field transport the total pressure $p_{tot} = p_{stat} + p_{dyn}$ is conserved along a field line, with the static pressure $p_{stat} = nk_BT$ and the dynamic pressure $p_{dyn} = nm_ev^2/2$. The plasma is static at the upstream position and is accelerated to sound speed, c_s, at the target (see eq. 2.6 and 2.7). With $\alpha = 1$ for c_s, this yields a relation between upstream and target pressure:

$$\begin{aligned} n_u k_B T &= n_t k_B T + \frac{2 n_t m_e k_B T}{2 m_e} \\ \Rightarrow n_t &= \frac{1}{2} n_u \end{aligned} \tag{2.19}$$

Now, with equations 2.19, 2.11 and 2.7 the temperature along the field line can be approximated as:

$$T \approx \left(\frac{m_e}{(2k_B)^3}\right)^{1/3} \left(\frac{q_\parallel}{\gamma n_u}\right)^{2/3} \tag{2.20}$$

The particle flux density at the target, equations 2.7 and 2.20, finally results in:

$$\Gamma_t = n_t c_s = \left(\frac{1}{16 m_e^2}\right)^{1/6} \left(\frac{q_\parallel n_u^2}{\gamma}\right)^{1/3} \tag{2.21}$$

The target parameters depend now only on the external control parameters n_u and $q_\parallel$ which relate to the main plasma density and the plasma heating power, respectively.

2.2.2 The high recycling regime - the Two-Point-Model

If the upstream density is increased while keeping the heating power constant, the level of recycling increases. It is assumed here, that the particle source due to recycling is much stronger than the main plasma particle source. For simplicity it is assumed that all the recycled neutrals ionize in a very thin layer close to the target and in the same flux tube of the originally impacting ion. As in section 2.2.1 it is further assumed that there is no cross field transport of either particles or heat. The main plasma is the only heat source and all the heat will enter the SOL at the upstream position. In contrast to the low recycling regime, the only particle source is now the region in front of the target where the recycled neutrals ionize, called the *recycling zone*. This is a valid assumption, as the mean free path for electron impact ionization is short enough (sec. 4.4.1) such that the recycling cycle occurs near the target. Thus the plasma in the SOL between upstream and the entrance of the recycling zone is assumed to be stagnant, i.e. there is no particle flux, $\Gamma = 0$. Within the recycling zone the plasma is then accelerated to sound speed at the target, equation 2.6. Hence, the heat between upstream and the recycling zone is now conducted, giving this divertor regime also the name *conduction limited regime*. In order to carry the heat via conduction, temperature gradients have to arise in the SOL which result in lower temperatures at the target relative to the upstream position. In reality, the plasma in the SOL is not completely stagnant and convection still plays a role. In order to account for this, a *convection factor* ($0 < f_{conv} < 1$) which determines the heat fraction carried by convection, $q_{\parallel cond} = (1 - f_{conv}) q_\parallel$ is introduced. Integration of the conduction part in equation 2.17 from $x = 0$ to $x = L_c$ (L_c is the connection length between upstream and the target, defined in section 1.3) yields:

$$T_u^{7/2} = T_t^{7/2} + \frac{7}{2} \frac{(1 - f_{conv})\, q_\parallel L_c}{\kappa_{0,e}} \tag{2.22}$$

Strictly, it should be integrated from upstream to the entrance of the ionization zone as the heat in this zone is then convected. However, as convection is a very effective process and the ionization zone is taken to be very thin, it is assumed that the temperature at

the entrance of the zone is equal to the target temperature (see eq. 2.18). Due to the large exponent for T in equation 2.22, the term $T_t^{7/2}$ can be neglected as soon as T_t becomes even slightly smaller than T_u. Equation 2.22 thus simplifies to:

$$T_u^{7/2} \approx \frac{7}{2} \frac{(1 - f_{conv})\, q_\parallel L_c}{\kappa_{0,e}} \tag{2.23}$$

In order to account for frictional collisions between ions and neutrals, viscous forces and volume recombination, a *momentum loss factor* ($0 < f_{mom} < 1$) is introduced. With this, the pressure conservation (eq. 2.19) modifies to:

$$2 n_t T_t = (1 - f_{mom})\, n_u T_u \tag{2.24}$$

Line radiation in the SOL, either by impurities or recycled neutrals, and charge exchange collisions provide an energy sink for the electrons. These processes can be included by introducing a *power loss factor* ($0 < f_{pow} < 1$), yielding $q_{rad}^{SOL} + q_{cx}^{SOL} = (1 - f_{pow})\, q_\parallel$. The parallel heat flux density at the target, equation 2.11 (in which the potential energy can still be neglected with respect to the kinetic energy), can then be written as:

$$(1 - f_{pow}) q_\parallel = q_t = \gamma k_B T_t \Gamma_t \tag{2.25}$$

The three equations 2.23, 2.24 and 2.25 in the three parameters of interest, n_t, T_t and Γ_t combine to give:

$$T_t = \frac{q_\parallel^2}{n_u^2} \left(\frac{7 q_\parallel L_c}{2 \kappa_{0e}} \right)^{-4/7} \frac{2 m_i}{\gamma^2 e^2} \frac{(1 - f_{pow})^2}{(1 - f_{mom})^2 (1 - f_{conv})^{4/7}} \tag{2.26}$$

$$n_t = \frac{n_u^3}{q_\parallel^2} \left(\frac{7 q_\parallel L_c}{2 \kappa_{0e}} \right)^{6/7} \frac{\gamma^2 e^3}{4 m_i} \frac{(1 - f_{mom})^3 (1 - f_{conv})^{6/7}}{(1 - f_{pow})^2} \tag{2.27}$$

$$\Gamma_t = \frac{n_u^2}{q_\parallel} \left(\frac{7 q_\parallel L_c}{2 \kappa_{0e}} \right)^{4/7} \frac{\gamma e^2}{2 m_i} \frac{(1 - f_{mom})^2 (1 - f_{conv})^{4/7}}{(1 - f_{pow})} \tag{2.28}$$

The simplest case neglecting all loss factors ($f_{conv} = f_{mom} = f_{pow} = 0$) is called the *simple Two-Point-Model* [21]. At moderate upstream densities, which are sufficient to enter the high recycling regime, the target conditions can be fairly well described by the TPM. In this regime the target temperature is now very sensitive on the upstream density ($\propto 1/n_u^2$) and low values can be achieved by increasing the density.

In the simple Two-Point-Model all power entering the SOL is deposited on the surface. As the upstream density is increased, however, the hydrogen recycling is also increased due to the increased particle flux. This high recycling will, via line radiation, remove power from the SOL. Thus the power loss factor f_{pow} is no longer negligible which directly results in a reduction of the target heat flux (eq. 2.25). Another commonly used method

to increase the radiated power in the SOL is the injection of so-called *seeded* impurities such as N_2, He, Ne or Ar. A further effect of the radiation losses is to decrease the target temperature and to increase the target density and particle flux. In order to reduce the target flux, the ratio of conducted to convected heat flux must change, $f_{conv} > 0$, or momentum must be removed from the divertor plasma, $f_{mom} > 0$.

2.2.3 The detached regime

The necessary characteristics of the detached regime are, amongst the reduction of the surface heat load, that the particle flux to the target, Γ_t, decreases and that there is a pressure drop along the field line. It was shown in section 2.2.2, equation 2.24, that this can be achieved when momentum is removed in the SOL, $f_{mom} > 0$. Changing the ratio of conducted to convected heat transport, $f_{conv} > 0$, also reduces the particle flux at the target. The pressure, however, would still be conserved along a flux tube (eq. 2.24). The main mechanisms which remove momentum are elastic ion-neutral collisions (CX-collisions) and recombination. These processes dominate with respect to the ionization at temperatures below $\approx 5\,\mathrm{eV}$ and $\approx 1.5\,\mathrm{eV}$, respectively (see Fig. 3.1). These low temperatures can be achieved by a further increase of the main plasma density, as $T_t \propto n_u^{-2}$. At these temperatures, however, the simplification that the potential energy can be neglected with respect to the kinetic energy in equation 2.12 is no longer valid. Equation 2.25 is now written as:

$$(1 - f_{pow})q_{\parallel} = q_t = (2\gamma k_B T_t + E_{pot})\Gamma_t \tag{2.29}$$

with $E_{pot} = 18.1\,\mathrm{eV}$, section 2.1.2. Combining this equation with equation 2.24 yields an expression for the target temperature:

$$\frac{\sqrt{mk_B T_t}}{(2\gamma k_B T_t + E_{pot})} = 1.01 \frac{n_u}{q_{\parallel}^{5/7}} \left(\frac{\kappa_{0e}}{L_c}\right)^{-2/7} \frac{(1 - f_{mom})}{(1 - f_{pow})} \tag{2.30}$$

This equation can not directly be solved for T_t, but it can be seen that there is a competition between the power loss, necessary to remove the heat flux on the target, and the momentum loss which is needed to reduce the particle flux at the target. In the following, the two basic processes which remove momentum in the SOL are described.

Ion-neutral collisions - the gas target

Assume that in an elastic collision zone in front of the target the temperature is low enough for CX-collisions to occur. Recycled neutral hydrogen atoms or molecules will travel through this so-called *gas target* [22] and undergo several elastic collisions with hydrogen ions which flow to the target. As the masses of the neutral atom or molecule

and the ion are approximately equal, the momentum transfer is very efficient and the ions will rapidly cool down to the neutral temperature. After the collisions, the neutral will either reach the surface, where it deposits its momentum, or enter the hotter recycling zone, where it will ionize and flow back to the surface, removing no momentum. After the first collision, however, the neutral will travel at approximately the ion sound speed and the following collisions do not efficiently remove momentum. In order to maximize momentum removal, the neutral must reach the surface after each collision. The number of effective collisions is given by the mean free path for ion-neutral collisions, λ_{in}, and the divertor dimension, L_{div}. Most collisions would be efficient if both lengths are of the same order and small compared to the ionization mean free path:

$$\lambda_{in} \approx L_{div} \ll \lambda_{ion} \tag{2.31}$$

The reduction of the particle flux with respect to the flux entering the gas target at the recycling zone, Γ_r, is then approximately:

$$\frac{\Gamma_t}{\Gamma_r} \approx \frac{\lambda_{in}}{L_{gt}} \tag{2.32}$$

with L_{gt} being the length of the gas target. If the temperatures are below 5 eV over a sufficient large area and the neutral density is high, ion-neutral collisions provide an effective sink for momentum and particle flux. A measure of this effect is the increase of the neutral pressure in the divertor which can be determined with ionization gauges (see section 4.4.2).

In this simplified picture, cross field transport was neglected. It will be shown in section 2.3.1 that the particle and heat flux profiles peak close to the separatrix and decay radially. Due to CX-collisions, the particle and heat flux profiles will broaden, which corresponds to a reduction of the peak particle and heat flux. If the condition 2.31 is not fulfilled and CX-collisions do not remove momentum, they will nevertheless reduce the peak power flux to the target.

Another effect, which reduces the peak power flux to the target, should be noted here. The radial separation of the flux surfaces is much larger at the divertor target compared to upstream at the midplane position, see Figure 1.3, where the power enters the SOL. This is called *flux expansion*, which broadens the heat flux profile at the target and reduces the peak heat flux.

Volume recombination

If the temperature in the elastic collision zone falls below $T \approx 1-2$ eV then recombination becomes important. The ions flowing to the target can recombine with the electrons, directly decreasing the particle flux to the target. Borras [23] has given a more refined

formulation of the energy balance equation 2.29:

$$\left(2\gamma k_B T_t + \frac{E_{pot}}{(1 - f_{rec})}\right) \Gamma_t = q_{\parallel} (1 - f_{rad}) (1 - f_{fric}) \tag{2.33}$$

where f_{rad} is the radiated power upstream of the elastic collision. The energy lost by ion-neutral collisions is accounted for with f_{fric} and the ratio of the recombination to the ionization rate is given by f_{rec}. Solving this equation for the target particle flux yields:

$$\Gamma_t = \frac{q_{\parallel} (1 - f_{rad}) (1 - f_{fric})}{E_{pot} (1 - f_{rec})^{-1} + 2\gamma k_B T_t} \tag{2.34}$$

If $T < 1\,\mathrm{eV}$ ionization becomes negligible compared to the recombination (see sec. 3.2) and f_{rec} can reach high values $\approx 90\%$. At constant power entering the elastic collision zone, Γ_t can be reduced by an order of magnitude due only to recombination processes dominating [23]. It should be noted here that recombination is a volumetric process. If the plasma flow velocity towards the target is still high, the probability for recombination to occur would be low even if the temperature is reduced. Therefore, CX-collisions are needed in order to slow down the plasma.

Stability of the detached regime

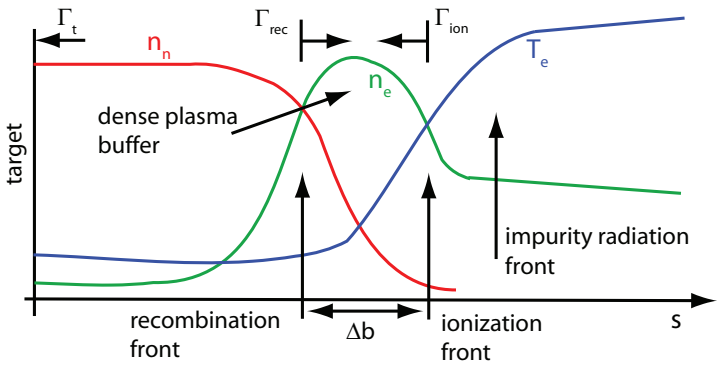

Figure 2.1: Sketch of a straightened out SOL, reproduced from [24]. See text for explanation.

What follows is a short summary of a theoretical work done by Krasheninnikov [24]. Consider a fixed power entering the SOL upstream, E_{sol}. This power first reaches the impurity radiation zone upstream of the recycling zone. With a power E_{imp} removed due to the impurity radiation, the remaining power reaching the hydrogen recycling zone is $E_{hyd} = E_{sol} - E_{imp}$. This sets an upper limit of the number of ionizations as each ionization costs an energy E_{ion}. This gives for the particle flux produced in the recycling zone:

$$\Gamma_{ion} < E_{hyd}/E_{ion} = (E_{sol} - E_{imp})/E_{ion} \tag{2.35}$$

These particles can recombine in the elastic collision zone, where temperatures are low, before reaching the target. The particle flux to the target is thus given by $\Gamma_t^+ = \Gamma_{ion}^+ - \Gamma_{rec}^+$, with Γ_{rec}^+ being the particle sink due to recombination, see Figure 2.1. The neutrals created by the recombination process will, however, reach the recycling zone where they are ionized. This neutral influx Γ_D^0 then equals the ion outflux Γ_D^+, assuming no neutral influx from the surface as an upper boundary. Equation 2.35 is then modified to:

$$E_{hyd} > E_{ion}\Gamma_D^0 \tag{2.36}$$

Here, Γ_D^0 must be reduced with reducing E_{hyd}. However, Γ_D^0 is proportional to the neutral pressure in the elastic collision zone, which increases as detachment proceeds. Therefore, a dense *plasma buffer*, cold enough that no ionization occurs, must exist between the ionization and recombination zone (Fig 2.1). This dense buffer reduces the transport of neutrals to the ionization zone by a factor proportional to $1/n_n$. Thus, Γ_D^0 can be reduced, with $E_{hyd} \to 0$, by increasing the plasma buffer density or width, see Figure 2.1. An increase of the plasma buffer density, however, increases the recombination rate, which sets an upper boundary on the neutral screening efficiency of the plasma buffer. This implies that the neutral flux in the recycling zone cannot be reduced below a critical value which depends on the power reaching the recycling zone, E_{hyd}, and the upstream pressure, p_u. The inequality 2.36 is now written as:

$$E_{hyd}/E_{ion} > \Gamma_D^0 > \Gamma_D^{0,crit}(E_{hyd}, p_u) \tag{2.37}$$

It can be seen that the recycling process sustains the upstream pressure and density, which are also limited to a critical value, depending on E_{hyd} and on the pressure and density in the recombination zone: $p_u \leq p_{rec}(E_{hyd})$, $n_u \leq n_{rec}(E_{hyd})$. These limitations are of practical relevance. If these boundaries are reached (via gas puffing to increase the main plasma density), the energy balance can no longer be sustained by hydrogen radiation if n_u increases further. At this point, n_u saturates and the cold and dense plasma buffer grows in order to accumulate the puffed particles. At some point this situation becomes unstable and the recycling zone is pushed upstream towards the X-point.

2.3 Additional processes in the SOL

Here, additional mechanisms present in the SOL are described which where excluded in the simple description of the divertor regimes above. These are the transport of particles and energy perpendicular to the field lines, called radial transport, and particle flows which can arise in the SOL, caused by $\vec{E} \times \vec{B}$ [25] and diamagnetic [26] drifts.

2.3.1 Radial transport in the SOL

The particle flux perpendicular to the field lines is, in first approximation, a combination of a diffusive process, implying a diffusion coefficient $D_\perp$ [m^2/s], and a convective process with velocity $v_\perp$. It can thus be described as:

$$\Gamma_t = -D_\perp \nabla_r n + v_\perp n \tag{2.38}$$

With the ansatz of a radial exponentially decaying density profile

$$n(r) = n(0) \exp\left[\frac{-r}{\lambda_n}\right] \tag{2.39}$$

equation 2.38 can be solved for the radial decay length λ_n. For purely diffusive transport, one obtains:

$$\lambda_n = \sqrt{\frac{2L_c D_\perp}{c_s}} \tag{2.40}$$

and for the case of convective transport only:

$$\lambda_n = v_\perp \tau_\parallel \tag{2.41}$$

The parallel loss time $\tau_\parallel$ is given by the ratio of particle content in the SOL to the loss rate to the targets:

$$\tau_\parallel = \frac{2L_c n}{2n_t c_s} = \frac{2L_c}{c_s} \tag{2.42}$$

Here, the density relation in the sheath limited regime, equation 2.19, was used as transport was assumed to be purely convective. It can be seen that both limit cases, either diffusive-only or convective-only radial transport, result in the same radial decay length. It is therefore convenient to introduce an effective diffusion coefficient $D_\perp^{eff}$ [27] including both, diffusive and convective effects:

$$\Gamma_t = -D_\perp^{eff} \nabla_r n \tag{2.43}$$

If the measured upstream density profile decays exponentially, $D_\perp^{eff}$ can be obtained by a fit of equation 2.39 and 2.40 to the measured data, assuming negligible sources and sinks. In the low recycling regime, reasonable agreement between modelling and experiment has been obtained for various machines [28, 29, 30] with this technique. However, this implies a spatially constant diffusion coefficient, an assumption which is not valid in high recycling or detached regimes. It has been found experimentally that $D_\perp^{eff}$ increases with radius as well as with increasing density [27]. The density effect was connected with an increase of the density and poloidal electric field fluctuation levels, $\tilde{n}/n$ and $\tilde{E_\Theta}/E_\Theta$,

caused by micro instabilities [25, 26]. Due to the $\tilde{E_\Theta} \times B_\Phi$ force (see sec. 2.3.2) this results in an outward radial flux:

$$\Gamma_r^{fluc} = \frac{\left\langle \tilde{n}\tilde{E_\Theta} \right\rangle}{B_\Phi} \tag{2.44}$$

In addition, larger scale plasma filaments or blobs [31], which extend along a field line, can be released from the main plasma. The $\vec{B} \times \nabla \vec{B}$ drift (eq. 2.48) can polarize these blobs, resulting in an outward radial motion via the $\vec{E} \times \vec{B}$ drift. Measurements have shown that this turbulent or intermittent convective transport can be of the same order as the diffusive radial transport [32].

The same picture essentially holds also for radial transport of power in the SOL. It can be written as the sum of a convected and diffusive, or conducted, cross-field transport (for $T_e = T_i = T$):

$$\begin{aligned} q_\perp &= q_\perp^{conv} + q_\perp^{cond} + q_\perp^{CX} \\ &= -\frac{5}{2} k_B T D_\perp \frac{\mathrm{d}n}{\mathrm{d}r} - n\chi_\perp \frac{\mathrm{d}}{\mathrm{d}r} k_B T + q_\perp^{CX} \end{aligned} \tag{2.45}$$

where $q_\perp^{CX}$ is the broadening of the heat flux profile due to CX collisions, which was discussed in section 2.2.3. The heat diffusion coefficient $\chi_\perp$ is usually larger than the particle diffusion coefficient $D_\perp$ by a factor of 2 to 5 [9]. Analogous to the radial particle profile (eq. 2.40) one can define a radial energy decay length λ_q. Consider the high recycling regime with only conductive radial transport and no power loss in the SOL. As the main plasma is the only power source, it must hold that:

$$\frac{\mathrm{d}q_\perp}{\mathrm{d}r} = -\frac{\mathrm{d}q_\parallel}{\mathrm{d}r} \tag{2.46}$$

With $q_{\perp,\parallel} = K_{\perp,\parallel} \mathrm{d}T/\mathrm{d}r_{\perp,\parallel}$ one obtains:

$$\begin{aligned} \lambda_q &= \sqrt{K_\perp / K_\parallel}\, L_c \\ &= \sqrt{e n_u \chi_\perp / \kappa_{0e} T^{5/2}}\, L_c \end{aligned} \tag{2.47}$$

In the high recycling or detached regime this simple derivation is invalid. For example, the radial particle flux due to fluctuation driven intermittent transport (eq. 2.44) directly results in a fluctuation driven, radial convected heat flux (eq. 2.45).

2.3.2 Drift flows in the SOL

In section 2.2, where simple relations between upstream and target parameters were derived, it was assumed that the particle flux occurs only between the region where the

neutrals ionize and the target. Due to electric and magnetic fields in the SOL, so-called particle *drifts* arise [33]. Before discussing the most important drifts, the normal, or *forward* direction of the toroidal magnetic field $\vec{B}_\Phi$ should be defined. It is that for which the ion ∇B drift velocity, given by [25]:

$$\vec{v} = \frac{v_\perp^2 m}{2eB^3}\,\vec{B} \times \nabla B \tag{2.48}$$

is directed towards the divertor. Usually the divertor is at the bottom of the machine, as in AUG. As the toroidal magnetic field decays radially proportional to $1/R$, the forward direction of $\vec{B}_\Phi$ is clockwise as viewed from the top. In the following it is assumed that $\vec{B}$ is perpendicular to the poloidal plane, as $B_\Phi \gg B_\Theta$.

The poloidal $\vec{E} \times \vec{B}$ drift

A radial electric field arises naturally due to a potential drop occurring in the sheath. In section 2.1.1 it was shown that the potential at the surface, $V_{surf} \approx -3k_B T_e/e$ depends on T_e. The temperature at the surface varies in the radial direction (section 2.3.1), resulting in a radial variation of V_{surf}. The resulting radial electric field is then given as:

$$E_r = -\frac{\partial V}{\partial r} \approx \frac{3k_B T_e}{e\lambda_{T_e}} \tag{2.49}$$

E_r is pointing radially outward in the SOL and oppositely in the private flux region. E_r and the resulting poloidal drift flux are shown in figure 2.2a for the forward field case. The poloidal drift flux density is approximately:

$$\Gamma_\Theta^{dr} \approx \frac{3k_B T_e n_e}{e\lambda_{T_e} B} \tag{2.50}$$

The radial $\vec{E} \times \vec{B}$ drift

From the Braginskii equations [18] (Ohm's law) the parallel electric field is known to be

$$E_\parallel = -\frac{0.71}{e}\frac{\partial T_e}{\partial s_\parallel} - \frac{1}{en_e}\frac{\partial p_e}{\partial s_\parallel} \tag{2.51}$$

where parallel currents in the SOL have been neglected for simplicity. The poloidal electric field is then $E_\Theta = (B/B_\Theta)E_\parallel$. Both the temperature and the pressure decrease towards the targets. Thus, E_Θ is directed towards the targets. The associated radial drift for forward field is directed from the outer SOL across the main plasma and private flux region towards the inner SOL, as shown in Figure 2.2b. The pressure along a field line drops, in the simplest case, by a factor of 2 (eq. 2.19). In the sheath limited regime $T_u \approx T_t$ (sec. 2.2.1) and the first term on the right hand side of equation 2.51

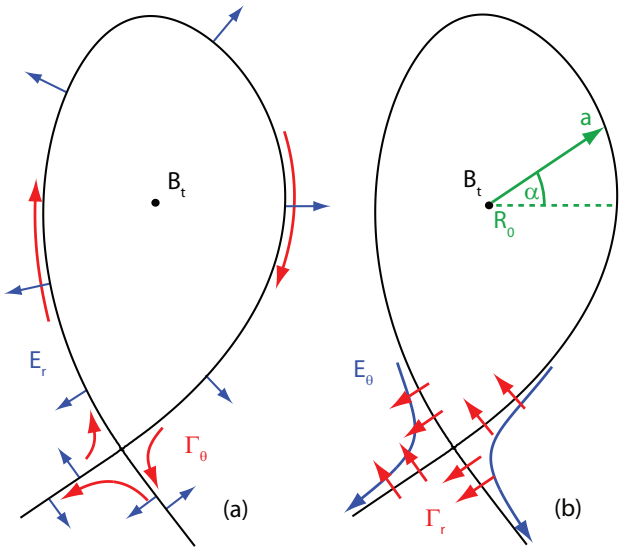

Figure 2.2: Sketch of the $\vec{E} \times \vec{B}$ drifts in the SOL. Blue arrows denote the electric fields and red arrows show the drift direction for forward field (B_t is pointing out of the paper). See text for explanation.

can be neglected, yielding $E_\parallel \approx -(k_B T_e)/(2eL_c)$. In the conduction limited regime the temperature gradient can become large (sec. 2.2.2). Assuming that the temperature gradient expands through the entire length of the SOL, L_c, gives $E_\parallel \approx -(k_B T_e^u)/(eL_c)$. The associated radial drift flux density is larger in the high recycling regime than in the low recycling regime, and is given by:

$$\Gamma_r^{dr} \approx \frac{n_e k_B T_e^u}{B_\Theta e L_c} \tag{2.52}$$

$\vec{E} \times \vec{B}$ drift fluxes vs. basic SOL fluxes

Drift induced fluxes will alter the overall flux distribution in the SOL, but particles will still flow towards the targets due to the basic divertor sink action. It is possible to approximate the strength of the drift fluxes relative to the basic SOL fluxes. The basic parallel SOL flux projected onto the poloidal plane is $\Gamma_\Theta \approx (B/B_\Theta) n_t c_s$. With the ion poloidal gyro frequency $\omega_{i\Theta} = eB_\Theta/m_i$ and $\rho_{s\Theta} = c_s \omega_{i\Theta}$, the relation of the poloidal drift flux (eq. 2.50) to the basic poloidal flux is:

$$\Gamma_\Theta^{dr}/\Gamma_\Theta \approx \rho_{s\Theta}/\lambda_{T_e} \tag{2.53}$$

With the basic cross-field flux (eq. 2.43) one can derive the associated ratio for the radial fluxes:

$$\Gamma_r^{dr}/\Gamma_r \approx \rho_{s\Theta}/\lambda_{n_e} \tag{2.54}$$

Drift fluxes become less important with higher density (and therefore lower temperature) as $\rho_{s\Theta}/\lambda_{T_e,n_e} \propto T^{3/4}\sqrt{D_\perp^{eff}}$. Finally it should be pointed out that although the $\vec{E}\times\vec{B}$ drifts are charge independent they change direction when the toroidal magnetic field is reversed. Changing $\vec{B}_\Phi$ in the experiment therefore allows to untangle to some extent the effects of these drifts.

The diamagnetic drift

Another drift naturally arising in the SOL is the diamagnetic drift caused by the pressure gradient:

$$\vec{v} = \frac{\vec{B}\times\nabla p}{en_eB^2} \tag{2.55}$$

This drift is the fluid analogue to the particle ∇B drift (eq. 2.48) and, in contrast to the $\vec{E}\times\vec{B}$ drifts, is charge dependent. This charge separation results in parallel currents in the SOL, known as *Pfirsch-Schlüter (PS) currents*, and, in parallel (or poloidal) particle flows. The focus is now on the ion flow, because the ions are less mobile and the density in the divertor is mainly determined by their transport. In forward field, this flow is directed towards the divertor. Therefore, the density in both the inner and outer divertor will be higher in forward field compared to reversed field. It is common to define the *PS flows* as a combination of this flow and the poloidal $\vec{E}\times\vec{B}$ flow (section 2.3.2). Assuming a cylindrical plasma geometry, the parallel PS velocity is given as [34]:

$$\vec{v}_{\|i}^{PS} = 2\cos\alpha\,\frac{aB}{R_0B_\Theta}\left(\frac{E_r}{B} - \frac{\nabla_r p}{en_eB}\right) \tag{2.56}$$

where α, a and R_0 are indicated in Figure 2.2b. It can bee seen that $\vec{v}_{\|i}^{PS}$ is zero at the top and bottom of the machine and maximum at the midplane. A detailed investigation of the effect of PS flows on the SOL plasma and comparison of measurements with code calculations can be found in [34] and references therein.

Ionization driven flow reversal

Another effect inducing an additional flow in the SOL is the so-called *ionization driven flow reversal* [35, 36]. The origin of this flow is independent of electric or magnetic fields in the SOL. Consider the divertor as being in the high recycling regime with the ionization zone close to the targets. Both density and temperature profiles decay radially along the target (sec. 2.3.1) being highest close to the separatrix. Neutrals, which are released from the surface, will ionize preferentially in the region of higher temperature and density close to the separatrix. The ionization source in this region can exceed the ion loss to the divertor target and a water-shed is formed at some distance from the

target. Above this water-shed, the ions then flow upstream in a thin region close to the separatrix. Such flow reversal has been measured e.g. in the outer divertor of Alcator C-Mod [37]. Here, it occured only in forward field where the outer divertor was hotter than the inner. This led to the suggestion that flow reversal results in a plasma flow from the hotter to the colder divertor. A recent modelling approach [38] showed that flow reversal can occur at both the inner and outer divertor, being stronger at the hotter outer divertor.

It must be noted that flow reversal and all drifts discussed above will appear, in the worst case, simultaneously. Hence, they will affect each other to some extent. A correct treatment of the drift effects on the SOL plasma is therefore only possible with the use of sophisticated two dimensional computer models.

2.4 Current understanding of detachment

Plasma detachment has been experimentally investigated in all present day tokamaks and the qualitative mechanisms leading to detachment seem to be understood [10, 11]. As detachment is a 2D strongly coupled nonlinear process a quantitative description is only possible with extensive code simulations. In particular to predict the ITER divertor performance a correct simulation of divertor detachment is indispensable. But even with the most sophisticated codes, divertor detachment of present day machines has not yet been successfully reproduced [8]. Several experimental observations are still not fully understood.

For example, the onset of detachment, defined as when the ion flux to the target starts to decrease as the plasma density is further increased (the so-called *roll over*), happens in most tokamaks much earlier at the inner divertor in forward field configuration. Moreover, the inner divertor receives a higher ion flux and a lower power load before the onset of detachment compared to the outer divertor. Several reasons for this so-called *divertor asymmetry* have been discussed [37, 39, 40, 41, 42]. At present it is thought that they are primarily caused by drift flows [43, 44]. The effect of the drift flows on the SOL flow has been tried to model (e.g. [45, 46]). Although the qualitative trend of the drift effects was reproduced by the models, absolute values of the flow velocity in the SOL were underestimated by at least a factor of 2-10.

Furthermore, the radial transport of plasma particles in the SOL is not experimentally well known. In the codes it is usually assumed to be of diffusive nature [47] including a radial dependence, $D_\perp(r)$ (equation 2.43). However, it was shown for medium to high densities that intermittent transport (equation 2.44) can be dominant [48] and increases with increasing density [49]. In recent modelling of experimental observations, a collisionality, and hence density dependent diffusion coefficient, was used [50]. This

yields better agreement with the experimental density necessary to achieve the roll over.

Detachment is typically studied by comparing target and upstream values, as no information on plasma parameters in the divertor volume (aside from the bolometric measured radiation distribution) is available. The DIII-D tokamak is an exception, as it has a divertor Thomson scattering system at the outer divertor. As the mechanisms leading to detachment are volumetric processes, however, knowledge of the distribution of the plasma parameters, such as the electron density, in the divertor volume is necessary to understand the detachment process.

In addition, the evaluation of the target density and temperature from Langmuir probe measurements is difficult in strongly detached conditions (which are earlier achieved in the inner divertor), as the particle fluxes are usually to low for a correct data evaluation. Moreover, the outer target is more critical in terms of the received heat flux due to the divertor asymmetry. Therefore, studies on detachment are normally concentrated on the outer divertor. Thus it is not known if the inner and outer divertor evolve independently of each other or not.

Chapter 3

Atomic processes

In this chapter the basic atomic processes appearing in a plasma will be introduced. Based on this, the emissivity of a certain spectral line with respect to the density and temperature of the surrounding plasma will be derived. Finally, a method is presented which allows the determination of the particle flux of a certain species based on the measurement of the radiance of a spectral line emitted by that species.

3.1 Atomic processes and equilibrium

The basic atomic processes in a plasma due to their interaction are derived. Consider an atom or ion being in the charge state z, named A^z. An excited atom or ion is denoted with A^{z*}. Each of the following equations describe processes which can happen in both directions, thus they have two names:

$$\begin{aligned} \text{impact excitation} &\leftrightarrow \text{impact de-excitation} \\ A^z + e &\leftrightarrow A^{z*} + e' \qquad (3.1) \\ \text{spontaneous emission} &\leftrightarrow \text{photon absorption} \\ A^{z*} &\leftrightarrow A^z + h\nu \qquad (3.2) \\ \text{impact ionization} &\leftrightarrow \text{three body recombination} \\ A^z + e &\leftrightarrow A^{z+1} + e' + e'' \qquad (3.3) \\ \text{radiative recombination} &\leftrightarrow \text{photon ionization} \\ A^{z+1} + e &\leftrightarrow A^z + h\nu \qquad (3.4) \end{aligned}$$

These processes tend to bring the population densities of the various species into equilibrium. If the relaxation time is short compared to the transport time scale in the plasma, then these processes are in a local equilibrium which depends on the local plasma density and temperature. For very high densities, like in the centre of stars, the mean free

path of a photon is short compared to the gradient length. The usual situation in fusion plasmas is that the photonic reactions (equations 3.2 and 3.4) are not in equilibrium and the plasma is optically thin. For high densities, the collisional processes are in equilibrium and it holds the Boltzmann relation and the Saha equation, which is called the local thermodynamical equilibrium. In the opposite case, at low densities almost all ions are in the ground state. The only excitation process is the impact excitation which is completely balanced by spontaneous emission. This is called the corona model. The typical densities in divertors, however, are above the area of validity of the corona model ($n_e < 1 \cdot 10^{18}\,\mathrm{m}^{-3}$). In this density range, models have to be used which also take into account collisions and radiative processes, i.e. collisional radiative models.

3.2 The Collisional Radiative Model

Extensions to the Corona model have been made by Bates [51], which became known as the *Collisional Radiative Model*, and was further improved by McWhirter and Summers [52]. In this approach, a detailed review of which can be found in [53], all atomic processes (eq. 3.1-3.4) are taken into account. The excitation levels of a specific charge state are divided into metastable states indexed by a Greek character, A^z_ρ, and excited states index by a Roman character, A^z_i. The main mechanisms leading to the population of A^z_i are excitation from the metastable level A^z_ρ and recombination from the ground level of the next higher charge state, denoted by A^{z+1}_1. The ratio of their population densities, n_ρ and n^+_1 respectively, which are called the dominant populations, are assumed to be known. The populations of the excited levels, n_i can be assumed to be in a quasi static equilibrium with respect to the dominant populations since the equilibration time scale is of the order of the radiative decay time of the excited levels which is typically of the order of $10^{-9}\,\mathrm{s}$. The collisional radiative model evaluates the dependence of the excited populations on the the dominant populations. The solution for the population density of a certain excited state is given by:

$$\begin{aligned} n_j &= -\sum_{i=1}^{O} C^{-1}_{ji} \sum_{\sigma=1}^{M} C_{i\sigma} n_\sigma + \sum_{i=1}^{O} C^{-1}_{ji} r_i n_e n^+_1 + \sum_{i=1}^{O} C^{-1}_{ji} q^{CX}_i n_H n^+_1 \\ &= \sum_{\sigma=1}^{M} F^{exc}_{j\sigma} n_e n_\sigma + F^{rec}_{j1} n_e n^+_1 + F^{CX}_{j1} n_H n^+_1 \end{aligned} \tag{3.5}$$

with O and M the number of excited and metastable levels, respectively, r_i is the free electron recombination coefficient directly to the level i and q^{CX}_i is the charge exchange recombination coefficient from neutral hydrogen with density n_H to the level i. As the usual plasma species is hydrogen or a hydrogen isotope, see section 1.3, this element is taken as charge exchange partner. The C are elements of the collisional radiative matrix:

$$C_{ji} = -A_{i\to j} - n_e q^e_{i\to j} - n_p q^p_{i\to j} \tag{3.6}$$

with the rate coefficients for spontaneous transition, $A_{i\to j}$, electron induced collisional transition, $q^e_{i\to j}$ and ion induced collisional transition, $q^p_{i\to j}$. Usually, the ion induced collisions can be neglected compared to the electron induced collisions. Their rate coefficients depend only on T_e as $v_e \gg v_i$. The Fs in equation 3.5 are the effective contributions to the population of the excited level j by excitation from metastables, free electron recombination and charge exchange recombination from neutral hydrogen, respectively. Multiplying these Fs with the appropriate Einstein coefficients for a transition from the excited level j to k, $A_{j\to k}$, gives the so-called *Photon Emissivity Coefficients*, PEC. The emissivity of a spectral line with charge z can finally be derived by:

$$\epsilon^z_{j\to k} = n_e n^z \mathrm{PEC}^{exc}(n_e T_e) + n_e n^{z+1} \mathrm{PEC}^{rec}(n_e T_e) + n_H n^{z+1} \mathrm{PEC}^{CX}(n_e T_e T_i T_H) \tag{3.7}$$

These PECs depend on the local density and temperature and have been calculated for various elements and transitions by the ADAS[1] project [54]. From this, total rate coefficients for ionization, recombination and charge exchange can be obtained for a specific element. These rate coefficients for deuterium are shown in Figure 3.1 for two different densities.

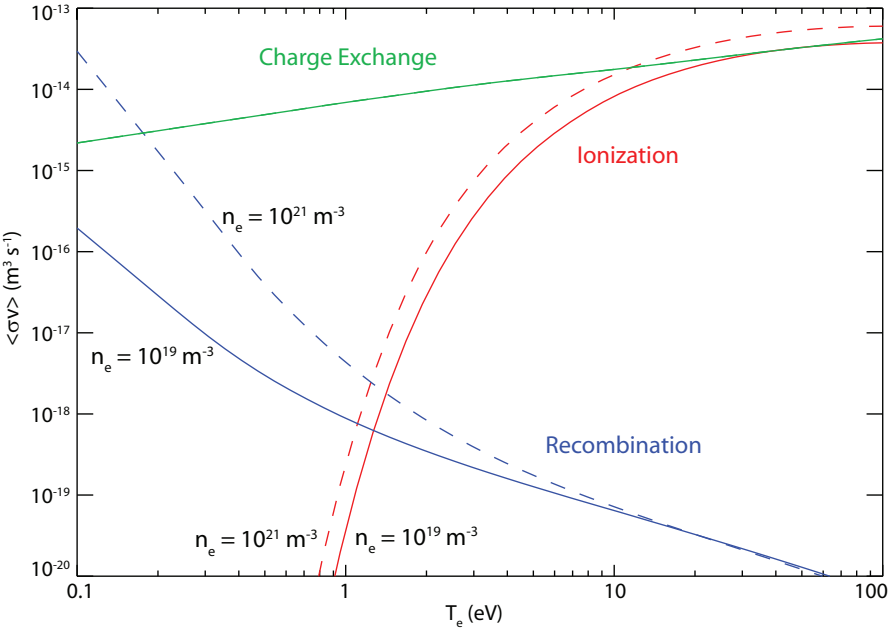

Figure 3.1: Ionization, recombination and charge exchange rate coefficients for two different densities and $T_e = T_i = T_H$.

[1] Atomic Data and Analysis Structure

It can be seen that the charge exchange process dominates with respect to the ionization process when $T_e < 5\,\mathrm{eV}$. Furthermore, recombination becomes stronger than ionization when $T_e < 1.5\,\mathrm{eV}$. This was discussed in section 2.2.3, where a strong temperature reduction in the divertor is needed in order to remove momentum via CX and recombination processes.

In this work, the radiating element of interest is the hydrogen isotope deuterium. As the CX partner is also hydrogen, these are elastic collisions which do not cause photon emissions. For this specific case, the charge exchange contribution has not to be taken into account in equation 3.7 for the line emissivity. For the Balmer D_δ line, $n = 6 \rightarrow n = 2$, equation 3.7 is then written as:

$$\begin{aligned} \epsilon^{+0}_{6\rightarrow 2} &= n_e n_H^{+0} \mathrm{PEC}^{exc}(n_e T_e) + n_e n_H^{+1} \mathrm{PEC}^{rec}(n_e T_e) \\ &= n_e n_H \underbrace{\left(f^{+0} \mathrm{PEC}^{exc}(n_e T_e) + f^{+1} \mathrm{PEC}^{rec}(n_e T_e) \right)}_{\mathrm{TEC}} \end{aligned} \tag{3.8}$$

with n_H^{+0} and n_H^{+1} the neutral hydrogen and ionized hydrogen density, respectively. The fractional abundance, f, is the ratio of the neutral or ionized hydrogen density to the total hydrogen density n_H: $f^{+0,+1} = n^{+0,+1}/n_{tot}$. The expression in the brackets is in this work called the total line emission coefficient, TEC.

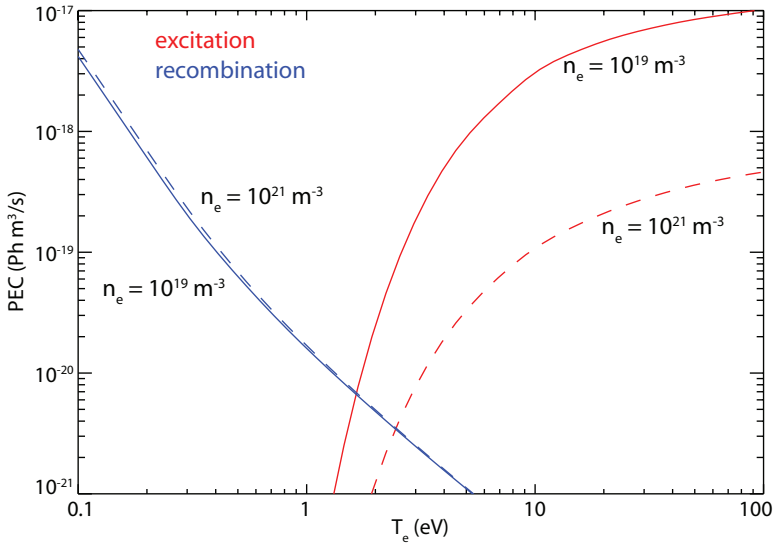

Figure 3.2: Balmer D_δ photon emission coefficients (PEC) for excitation (red) and recombination (blue) derived from ADAS for two different densities.

Figure 3.2 shows the photon emission coefficients for excitation and recombination for the Balmer D_δ line. It can be seen that at $T_e \approx 1.5-2\,\mathrm{eV}$ there is a sharp transition from recombination dominated radiation to excitation dominated radiation. Furthermore, the PEC^{rec} is relatively insensitive to the electron density, in contrast to the PEC^{exc}.

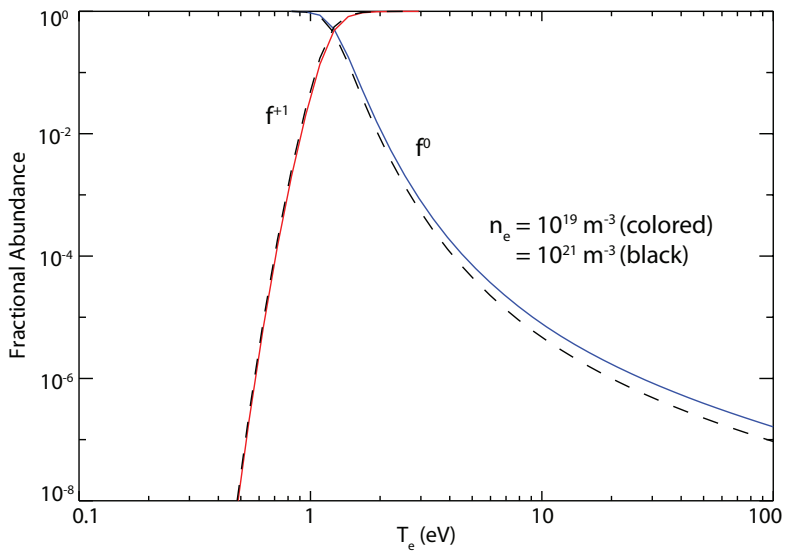

Figure 3.3: Fractional abundance for neutral (red) and ionized (blue) deuterium derived from ADAS for two different densities.

In Figure 3.3 the fractional abundance for neutral and ionized deuterium, which is almost insensitive to the electron density, is shown. For this plot, the transport effects are neglected and only the balance of ionization and recombination rates is taken into account. Below $T_e \approx 1.5\,\mathrm{eV}$ almost all deuterium atoms are in the neutral state as the rate coefficient for ionization is low in this temperature range (Fig. 3.1). Above $T_e \approx 1.5\,\mathrm{eV}$ almost all deuterium atoms are in the ionized state as then ionization dominates with respect to recombination, see Figure 3.1. The neglected transport effects will lead to a modification of the curves, but the transition from neutral to ionized hydrogen is always around $\approx 1.5\,\mathrm{eV}$.

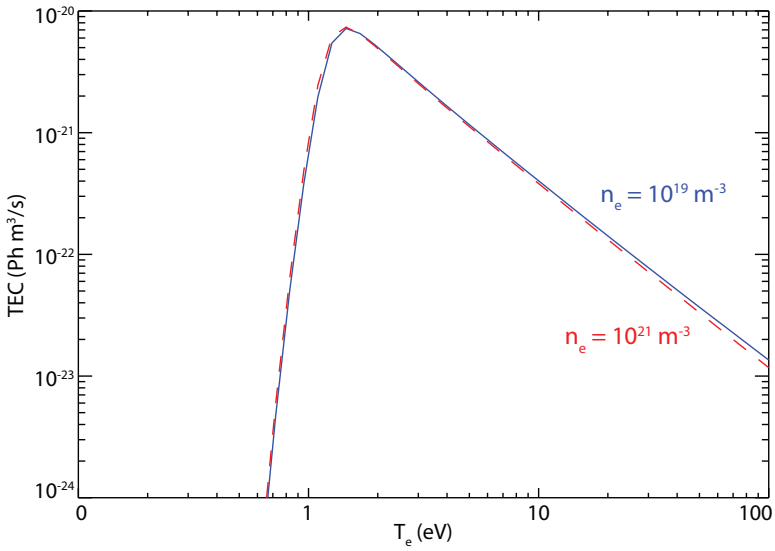

Figure 3.4: Balmer D_δ total emission coefficient for two different densities.

With the PECs for excitation and recombination, Figure 3.2, and the fractional abundance, Figure 3.3, one can calculate the total emission coefficient for the Balmer D_δ line, equation 3.8, which is shown in Figure 3.4. The TEC peaks at $T_e \approx 1.5\,\mathrm{eV}$ and drops rapidly when the temperature decreases. This is due to the strong decrease of the ionized deuterium density when the temperature decreases, which is stronger than the increase of the PEC^{rec}. Moreover, the TEC does almost not depend on the electron density.

3.3 Electron temperature determination from line ratios

By measuring the line emission ratio of two different transitions of the same atom it is in principle possible to determine the electron temperature. Therefore it is necessary that the line emission of both transitions, the TEC, does weakly depend on the electron density. For example, this is routinely done at TEXTOR by measuring helium line ratios [55]. The determination of the electron temperature is also possible by measuring deuterium line ratios. With the spectrometers used for this work, it was possible to measure the Balmer D_δ and D_ϵ lines simultaneously, see section 4.3.1. The line emission ratio is the ratio of the corresponding TECs and given by equation 3.8:

$$\frac{\epsilon_{6\to2}}{\epsilon_{7\to2}} = \frac{\mathrm{TEC}_{D_\delta}}{\mathrm{TEC}_{D_\epsilon}} \tag{3.9}$$

where the electron and total hydrogen densities cancel out. The line ratio of D_δ/D_ϵ is calculated for two different densities and shown in Figure 3.5.

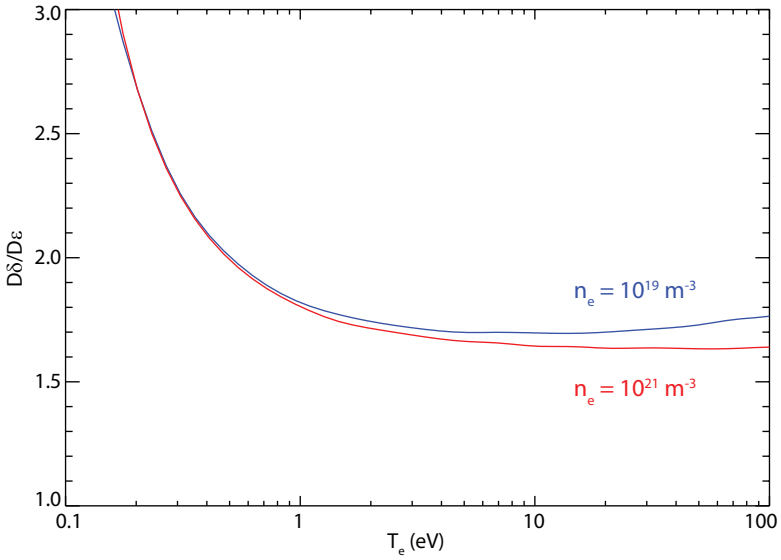

Figure 3.5: Line emission ratio of D_δ and D_ϵ for two different densities.

It can bee seen that the line ratio depends weakly on the electron density and increases strongly at $T_e < 1\,\mathrm{eV}$ when recombination becomes dominant. At temperatures above $\approx 1\,\mathrm{eV}$ the line ratio is also insensitive to the temperature. The temperature can therefore only be deduced from this line ratio if $T_e < 1\,\mathrm{eV}$. The spectroscopic measurements are line integrated measurements. Quantitative local line emission ratios can thus not be obtained. However, due to the strong increase of the line ratio below 1 eV and the flat profile above this temperature it can be determined whether recombination is dominant and thus whether T_e is smaller than 1 eV.

3.4 Spectroscopic determination of hydrogen flux densities

It is possible to determine the hydrogen flux density by a spectroscopic measurement of its line radiation. In section 3.2, Figure 3.2 it was shown that the radiation is either ionization dominated or recombination dominated. In the following, the method calculating the hydrogen flux density will be presented for both cases.

3.4.1 Ionizing plasma

In section 2.2 it was discussed that hydrogen ions impinging on the surface can release neutral hydrogen atoms from the surface. These atoms travel through the SOL plasma where the temperature is high enough that they are ionized. In addition, these atoms can emit photons via electron impact excitation. The first important constraint is that the ionization rate is a measure for the influx, i.e. that the recombination can be neglected. It can then be deduced from the collisional radiative model how many photons are emitted on average per ionization. The second constraint is that the ionization and the excitation have to occur in the same volume. It is common to abbreviate the rate coefficients for the basic processes as follows:

$$\text{electron impact ionization} \;:\; S_z =< \sigma_{z\to z+1} v_e > \tag{3.10}$$

$$\text{radiative recombination} \;:\; \alpha_z =< \sigma_{z\to z-1} v_e > \tag{3.11}$$

$$\text{electron impact excitation} \;:\; X_{ik} =< \sigma_{ik} v_e > \tag{3.12}$$

The simple one dimensional transport equation for neutral hydrogen perpendicular to the divertor surface can be written as:

$$\frac{\partial n_H^0}{\partial t} = -\frac{\mathrm{d}}{\mathrm{d}x}\Gamma_H^0 - S n_e n_H^0 + \alpha n_e n_H^+ \tag{3.13}$$

where Γ^0_H is the flux density of neutral hydrogen. Furthermore it is assumed that T_e and n_e only vary perpendicular to the divertor surface. In equilibrium, the derivative with respect to the time is zero. Integration of equation 3.13 yields:

$$\Gamma^0_H(x) - \Gamma^0_H(0) = \int_0^x (-S n_e n^0_H + \alpha n_e n^+_H)\, dx \tag{3.14}$$

The integration is then taken so far into the plasma where all neutral hydrogen is already ionized, i.e $\Gamma^0_H(x) = 0$. As a pure ionizing plasma is assumed here, the recombination term on the right side of equation 3.14 can be neglected, giving the neutral hydrogen flux density at the divertor surface ($x = 0$):

$$\Gamma^0_H(0) = \int_0^x S n_e n^0_H\, dx \tag{3.15}$$

The radiance $\Gamma_{\gamma,i\to k}$ for a transition from i to k along a line of sight perpendicular to the divertor surface is for the case of pure ionization given by:

$$\Gamma_{\gamma,i\to k} = \int_0^x X_{ik} B_{ik} n_e n^0_H\, dx = \int_0^x \mathrm{PEC}^{exc}_{ik} n_e n^0_H\, dx \tag{3.16}$$

where the branching ratio $B_{ik} = A_{ik}/\sum_i A_{ij}$ with $j > i$ was used. The effective XB value from the collisional radiative model corresponds to the PEC^{exc} in equation 3.7. The S and XB values depend on the electron density and temperature, $S = S_0\, f(n_e, T_e)$ and $XB = (XB)_0\, f(n_e, T_e)$, and it is assumed that both values have approximately the same dependence on n_e and T_e. This is a reasonable assumption as can bee seen in Figure 3.1 and 3.2. The neutral hydrogen influx density can finally be determined from the measured radiance via:

$$\begin{aligned} \frac{\Gamma^0_H(0)}{\Gamma_{\gamma,i\to k}} &= \frac{S_0 \int_0^x f(n_e,T_e) n_e n^0_H\, dx}{(XB)_0 \int_0^x f(n_e,T_e) n_e n^0_H\, dx} \\ \Rightarrow \Gamma^0_H(0) &= \frac{S_0}{(XB)_0}\, \Gamma_{\gamma,i\to k} \end{aligned} \tag{3.17}$$

Not only hydrogen is released from the wall due to impinging plasma ions but also impurity species due to *sputtering*. With this method, which became known as the *S/XB method* [56], also the impurity influx can be deduced. The S/XB values have been calculated for various species and transitions and are stored in the ADAS database. In Figure 3.6a the S/XB value for the Balmer D_ϵ line is shown for two different densities.

3.4.2 Recombining plasma

If one assumes, in the opposite case, a low temperature plasma where only recombination processes are dominant (see Figures 3.1 and 3.2), then the transport equation 3.13 for

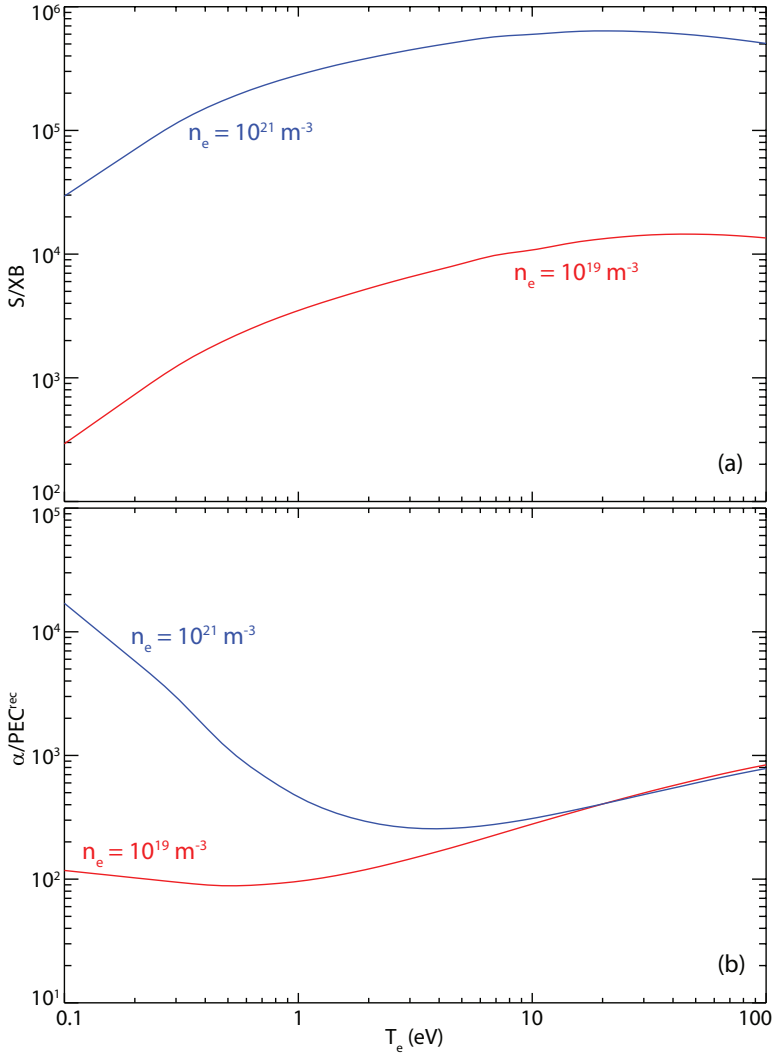

Figure 3.6: S/XB (a) and $\alpha/\mathrm{PEC}^{exc}$ (b) values for an ionizing and recombining plasma, respectively, for the Balmer D_ϵ line and two different densities.

ionized hydrogen can be written as:

$$\frac{\partial n_H^+}{\partial t} = -\frac{\mathrm{d}}{\mathrm{d}x}\Gamma_H^+ + S n_e n_H^0 - \alpha n_e n_H^+ \tag{3.18}$$

Integration of this equation yields:

$$\Gamma_H^+(x) - \Gamma_H^+(0) = \int_0^x -\alpha n_e n_H^+ \, dx \tag{3.19}$$

where the ionization term has already been neglected. Now it is assumed that at the divertor surface all ionized hydrogen is recombined to neutral hydrogen, i.e. $\Gamma_H^+(0) = 0$ in equation 3.19. The radiance, according to equation 3.16, is for a recombination dominated plasma written (see eq. 3.7):

$$\Gamma_{\gamma,i\to k} = \int_0^x \mathrm{PEC}_{ik}^{rec} n_e n_H^+ \, dx = \int_0^x R_{ik} B_{ik} n_e n_H^+ \, dx \tag{3.20}$$

To give an analogy for the XB value in equation 3.16, the PEC_{ik}^{rec} is named here RB. As in section 3.4.1, it is assumed that the α and RB values show approximately the same density and temperature dependence (compare Figure 3.1 with Figure 3.2). Furthermore, the ion flux density in the SOL at the position x can be assumed to be equal to the neutral flux density at the surface ($x = 0$), as the constraint here was that all ions are recombined before reaching the surface. The neutral hydrogen flux density at the surface can then be determined from the measured radiance for the case of a recombination dominated plasma by:

$$\Gamma_H^0(0) = \Gamma_H^+(x) = \frac{\alpha_0}{(RB)_0} \Gamma_{\gamma,i\to k} \tag{3.21}$$

The α/RB value for the Balmer D_ϵ line for two different densities is shown in Figure 3.6b. It has to be noted that, although the S/XB and α/RB values are finite in the entire plotted temperature range, one has to use either the S/XB or α/RB value, depending on the plasma conditions (recombining or ionizing) which set the constraints of this model. Furthermore, one has to keep in mind that at a density of the order of $10^{19}\,\mathrm{m}^{-3}$ the divertor plasma of ASDEX Upgrade is too hot to be recombining and the S/XB method has to be used. On the other hand, at a density of the order of $10^{21}\,\mathrm{m}^{-3}$, the divertor plasma is usually too cold to be ionizing and the α/RB method is valid.

Chapter 4

Diagnostic

In this chapter, the development of a new diagnostic capable of determining the electron density in the divertor volume is presented. It is based on the spectroscopic measurement of the Stark broadening of the Balmer lines. The theory of Stark broadening in a plasma has already been extensively reviewed in [57]. In section 4.1 the two basic approaches to calculate the Stark broadening are summarized. The influence of other broadening mechanisms, such as e.g. the Zeeman splitting, is discussed in section 4.2. Thereafter, in section 4.2, the setup of the Stark broadening diagnostic, SBD [58], is presented. Finally, in section 4.4, the SBD measurements are compared to Langmuir probe and ionization gauge measurements in order to check for consistency.

4.1 Theory of Stark broadening in a plasma

In this section the broadening of spectral lines due to the influence of surrounding particles on the emitting atoms is discussed. This effect is proportional to the density of the surrounding particles and can, therefore, be used as a measure of this parameter if the relationship between particle density and spectral line shape is known. As the surrounding particles in a plasma are charged particles, this broadening is a combination of the pressure broadening due to coulomb collisions, also called the *collision damping* theory, and the *statistical theory*, which is the Stark splitting due to the electric field produced by the surrounding particles. The combination of both mechanisms is called *Stark broadening*. The collision damping theory becomes valid if the duration of the perturbation is short compared to the *time of interest*, τ, which is the inverse of the frequency shift caused by the perturbation. This effect determines the centre of the broadened spectral line. On the other hand, the statistical theory becomes valid when the duration of the perturbation is long compared to τ and it determines the line wings. In section 4.1.1 the question of when to use which theory will be addressed. The effect of an additional Zeeman splitting on the line broadening, which is unknown, can be easily included in the

so-called *unified theory*. This semi quantum mechanical approach calculating the Stark broadening, where the perturbation caused by the electrons and ions is calculated with the collision damping and the statistical theory, respectively, will be introduced in section 4.1.2. The pressure broadening caused by the ions, valid in the line centre, has to be neglected in this theory. With the so-called *model microfield method*, MMM, introduced in section 4.1.4, this restriction can be overcome. Stark broadened spectral line shapes of different Balmer lines calculated with both theories are compared. The influence of the other broadening mechanisms, including the Zeeman splitting, is discussed afterwards in section 4.2.

4.1.1 Validity of the collision damping and statistical theory

In AUG either hydrogen or a hydrogen isotope, typically deuterium, is used as the main gas species. Therefore, it will be focused here on hydrogen as the emitting atom. In a simplified picture, reviewed in [59], the emitting hydrogen atom in the plasma is most of the time not or weakly disturbed due to collisions. The corresponding spectrum is derived via the collision damping theory. From time to time, however, the atom experiences a strong collision, which results in a frequency shift $\Delta\omega_c$ of its emission. One can assume a collision time of $t_c \approx r/v_{rel}$, with the distance r between the emitting atom and the disturbing plasma particle and their relative velocity v_{rel}. This contribution to the emitted spectrum, derived from Fourier analysis, is a narrow broadening of width $\sim 1/t_c$ at $\Delta\omega_c$. As long as $1/t_c \ll \Delta\omega_c$, these contributions will add with respect to their statistical occurrence. The constraint $1/t_c \ll \Delta\omega_c$ is equivalent to the time of interest $\tau = \Delta\omega_c^{-1}$ being very short and the duration of the perturbation is long compared to τ. In this case the statistical theory is used. Assuming that the frequency shifts are caused by a central potential at distance r, then they will take the form:

$$\Delta\omega = \frac{C}{r^2} \tag{4.1}$$

One can approximate a critical wavelength shift $\Delta\lambda_c$ [60] below which the collision damping theory has to be used and above which the statistical theory applies:

$$\Delta\lambda_c = \frac{\bar{v}_{rel}^2 \lambda_0^2}{C 2\pi^3 c} \tag{4.2}$$

with the relative thermal velocity $\bar{v}_{rel}$, the unperturbed wavelength λ_0 and a constant C, which will be derived in section 4.1.3. The critical wavelength shift $\Delta\lambda_c$ is different for electrons and ions due to their different velocities in a thermal plasma ($T_e = T_i \Rightarrow v_i = \sqrt{m_e/m_i}\, v_e$). Therefore a unified description of the electrons and ions is not possible. In Table 4.1 $\Delta\lambda_c$ calculated for different Balmer lines and temperatures is shown.

Table 4.1: Critical wavelength shift $\Delta\lambda_c$ for different Balmer lines and temperatures.

Temperature:		5 eV		10 eV		20 eV	
D_β	Electrons	73.23	nm	146.4	nm	292.9	nm
	Ions	0.040	nm	0.060	nm	0.100	nm
D_γ	Electrons	21.94	nm	43.88	nm	87.75	nm
	Ions	0.012	nm	0.018	nm	0.030	nm
D_δ	Electrons	9.90	nm	19.79	nm	39.58	nm
	Ions	0.005	nm	0.008	nm	0.013	nm
D_ϵ	Electrons	6.88	nm	13.76	nm	27.52	nm
	Ions	0.004	nm	0.006	nm	0.009	nm

In the case of electrons the critical wavelength shift is very large. Hence, the collision damping theory has to be used throughout the entire spectrum. For the ions, however, the statistical theory is valid, with an exception in the very center of the spectral line where the collision damping theory has to be applied. This exception becomes less important for the higher members of the Balmer series.

4.1.2 The unified theory

With the so-called semi quantum mechanical *unified theory* it is possible to combine the pressure broadening by electrons with the Stark splitting caused by the ions. However, it is not possible to include the ion pressure broadening. A detailed description of this method can be found in [61]. Starting with the electron pressure broadening, the radiated power of an emitting system can be written as [62]:

$$P(\omega) = \frac{4\omega^4}{3c^2} \underbrace{\sum_{i,f} \delta(\omega - \omega_{if}) \left| \left\langle i|\hat{D}|f \right\rangle \right|^2 \rho_i}_{I(\omega)} \tag{4.3}$$

It is summed over all initial states $|i\rangle$, multiplied by their occupation probability ρ_i and summed over all final states $|f\rangle$ of the entire system. $\hat{D}$ is the transition dipole moment of the entire system. The sum can be interpreted as the spectral line profile $I(\omega)$ which is the Fourier transform of an auto correlation function $\Phi(t)$:

$$\Phi(t) = \sum_{i,f,j} e^{i\omega_{if}t} \left|\langle i|ex_j|f\rangle\right|^2 \rho_i \tag{4.4}$$

Several assumptions are made to find the auto correlation function of the system. The

perturbing electrons are treated as classical point charges (thus semi quantum mechanical) moving, in the case of a neutral particle as the emitting atom, along straight lines. Moreover, it is assumed that the electrons are unperturbed by the presence of the emitting atom. The reason for this is that the average energy of the interaction between the atom and the electron is small with respect to the kinetic energy of the electrons. This assumption is called the *classical path approximation*. In addition it is assumed that collisions leading to a broadening of the spectral line occur much more often compared to those causing transitions between different energy levels (the so-called *impact approximation*). The Schrödinger equation of this problem can be written as:

$$i\hbar\frac{d\Psi(t)}{dt} = \left[H_0 + H^e_{pert}(t) + H^{ion}_{pert}(E)\right]\Psi(t) \tag{4.5}$$

with H_0 being the Hamiltonian of the unperturbed system, $H^e_{pert}(t)$ is the time dependent interaction Hamiltonian due to electron collisions and $H^{ion}_{pert}(E) = e\vec{r}\vec{E}$ is the interaction Hamiltonian which depends on the electric field $\vec{E}$ produced by the ions. The auto correlation function of this system, with the assumptions described above, is then:

$$\Phi(t) = \vec{d}_{if}\left\langle\left\langle if\left|\exp\left[-\frac{i(H_f(E) - H_i(E))t}{\hbar} + \Omega_{i,f}t\right]\right|i'f'\right\rangle\right\rangle\vec{d}^{\,*}_{i'f'} \tag{4.6}$$

where $H(E) = H_0 + H^{ion}_{pert}(E)$ is the Hamiltonian of the initial and final states i, f. The sub levels i', f' of a certain energy level are generated by the perturbation due to the electron collisions. This perturbation is described with the perturbation operator $\Omega_{i,f}$. As the perturbation is proportional to n^4, with n the principal quantum number of the energy level, the effect of electron collisions on the lower level is neglected: $\Omega_{i,f} \approx \Omega_i$. Nguyen-Hoe, Drawin and Herman [63] calculated the collision operator which was used for this work:

$$\Omega_i = -\left[\frac{4\pi n_e e^4 a_0^2}{3\hbar^2}\left(\frac{2m}{\pi k_B T_e}\right)^{1/2}\right]\left(0.6342 + \ln\frac{1}{\epsilon}\right)\frac{\vec{r}_i\cdot\vec{r}_i}{a_0^2} \tag{4.7}$$

with

$$\epsilon = \frac{4\pi^{1/2}\hbar e}{(3m)^{1/2}\,k_B}\frac{n^2 n_e^{1/2}}{T_e} \tag{4.8}$$

where a_0 is the Bohr radius, n_e is in cm^{-3} and T is in K. The Fourier transform of equation 4.6 leads to the final expression of the spectral line shape:

$$I(\omega) = \frac{1}{\pi}\int_0^\infty dE\, W(E)\ \mathrm{Re}\ \vec{d}_{if} \times \\ \times \left\langle\left\langle if \left| \left[i\omega - \frac{i(H_i(E) - H_f(E))}{\hbar} - \Omega_i \right]^{-1} \right| i'f' \right\rangle\right\rangle \vec{d}^{\,*}_{i'f'} \tag{4.9}$$

First the spectral line broadening due to electron collisions (collision damping theory) is calculated for a given Stark splitting of the energy levels caused by a certain electric field strength produced by the ions multiplied by its probability of occurring $W(E)$, which will be derived in the next section (statistical theory). Then the total profile is obtained by integrating over all possible electric field strengths. As mentioned above, the influence of the ion collision damping, valid in the line center (see chapter 4.1.1), has to be neglected in the unified theory. But here an additional Zeeman splitting due to a magnetic field can easily be included, section 4.2.1.

4.1.3 Statistical theory

The perturbing ions are statistically distributed and produce so-called electric micro fields. In the case of hydrogen emitters, these electric fields lead to the well known Stark splitting. The energy levels split into $2n-1$ sub levels. The frequency splitting of a transition is proportional to the electric field caused by an elementary charge e of distance r, $E = \frac{1}{4\pi\epsilon_0}\frac{e}{r^2}$ (linear Stark effect):

$$\Delta\omega = \frac{3}{2}\frac{\hbar}{m}\frac{\Delta n_k}{r^2} \tag{4.10}$$

with $n_k = n \cdot k$, $k = 0;\ \pm 1;\ \cdots\ \pm(n-1)$. This yields a symmetric splitting of the transition lines between two energy levels which becomes larger with higher upper principal quantum number. An average frequency shift is derived by weighting the shift of the individual components with their line strength [64] $\overline{\Delta n_k} = \sum S\Delta n_k / \sum S_k$. C, introduced in equation (4.1):

$$C = \frac{3}{2}\frac{\hbar}{m}\overline{\Delta n_k} \tag{4.11}$$

For the Balmer lines H_β ($n = 3 \to 2$) up to H_γ ($n = 7 \to 2$) one gets:

$$C = (10.4;\ 20.5;\ 27.3;\ 42.7) \cdot 10^{-4}\frac{\mathrm{m}^2}{\mathrm{s}}$$

The problem is the determination of the electric field produced by the statistically distributed ions. With N disturbing ions of charge e in the volume V the total field strength at the place of the emitting atom, situated at the origin of a Cartesian coordinate system,

is $E = \sum^N E_i$. The probability that the field strength E_k produced by the kth particle is between E_k and $E_k + dE_k$ is equivalent to the probability that the kth particle is in the volume element dr_k. The probability that all N ions produce a field strength in the range of $E + dE$ is thus given by:

$$W(E)dE = \int \dots \int \delta(E - \sum_{i=1}^{N} E_i) \, \frac{g_N}{V^N} \, d\vec{r}_1, d\vec{r}_2, \dots d\vec{r}_N dE \tag{4.12}$$

where g_N is the correlation function of the N-particle system. The approximation of statistically independent particles ($g_N = 1$) producing a Coulomb field results in the Holtsmark distribution function [65]:

$$W(\beta) = \frac{2}{\pi\beta} \int_0^\infty v \, \sin v \, \exp\left[-\left(\frac{v}{\beta}\right)^{3/2} \right] \, dv \tag{4.13}$$

with the relative field strength $\beta = E/E_0$ and the normal field strength E_0, given by:

$$E_0 = \frac{2.61}{4\pi\epsilon_0} e n_e^{2/3} \tag{4.14}$$

Baranger and Mozer [66, 67] introduced two components of the micro field, produced by the electrons and ions, respectively. With this, correlations between the perturbing particles can be considered and g_N becomes:

$$g_2(\vec{r}_1, \vec{r}_2) \approx -\frac{e^2}{4\pi\epsilon_0 k_B T \, |\vec{r}_1 - \vec{r}_2|} \, \exp\left[-\frac{|\vec{r}_1 - \vec{r}_2|}{\lambda_D} \right] \tag{4.15}$$

Furthermore the field produced by the kth particle is shielded by the other particles and instead of a Coulomb field a Debye field is produced:

$$E_k = \frac{e}{4\pi\epsilon_0 r_k^2} \left(1 + \frac{r_k}{\lambda_D} \right) \, \exp\left[-\frac{r_k}{\lambda_D} \right] \tag{4.16}$$

with the Debye shielding length:

$$\lambda_D = \sqrt{\frac{\epsilon_0 k_B T}{e^2 n_e}} \tag{4.17}$$

A measure of this effect is the ratio between the average distance of the particles r_0, with $\frac{4}{3}\pi n_e r_0^3 = 1$, and the Debye length. The limiting case $r_0/\lambda_D \to 0$ is equivalent to the Holtsmark distribution. The distribution function $W(E)$ for several values of r_0/λ_D including the Holtsmark one is shown in Figure 4.1a. $W(\beta)$ shows for large β a decay proportional to $\beta^{-5/2}$. This results in a decay of the Stark broadened line wings that is proportional to $\Delta\lambda^{-5/2}$, which is a well known observation.

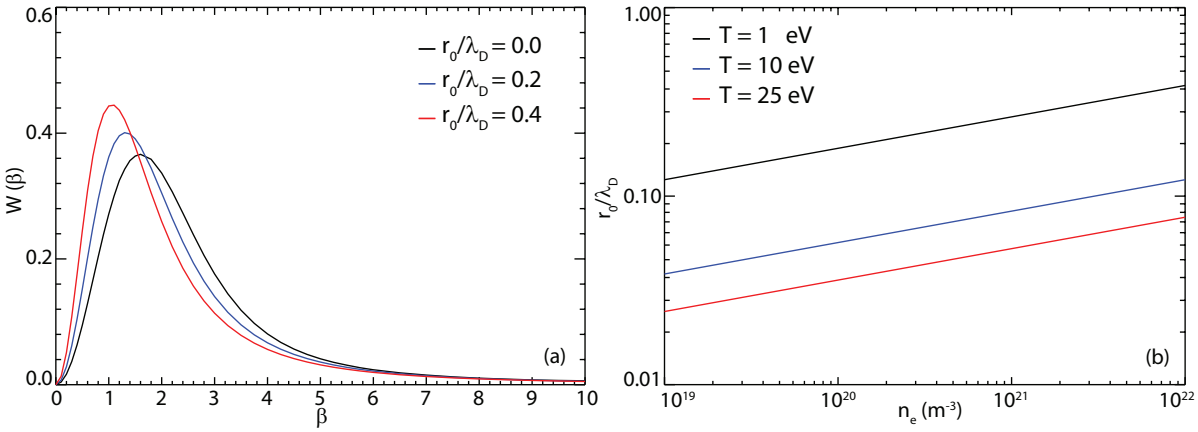

Figure 4.1: Probability distribution function from Mozer and Baranger [67] for different values of r_0/λ_d (a). The limit case $r_0/\lambda_D \to 0$ is equivalent to the Holtsmark distribution. Quotient r_0/λ_D for different temperatures versus the electron density (b).

In Figure 4.1b the fraction r_0/λ_D is shown for different densities and temperatures. For typical parameters at ASDEX Upgrade one can assume $r_0/\lambda_D \approx 0$ and use the Holtsmark distribution function. Only at very low temperatures $T_e \approx 1\,\mathrm{eV}$ and high densities $n_e > 1 \cdot 10^{21}\,\mathrm{m}^{-3}$ are values of $r_0/\lambda_D > 0.2$ reached and deviations from the Holtsmark distribution have to be considered.

4.1.4 Model Microfield Method

A different approach to calculate the Stark broadening in a plasma, named the *model microfield method* (MMM), was derived by Brissaud and Fritsch [68]. Considering only dipole interactions the time dependent electric micro field produced by the plasma electrons and ions is needed. Here, the field strength jumps instantaneously between constant values in a stochastic way [69]:

$$E(t) = \begin{cases} E_0 & \text{for } 0 \le t \le t_0 \\ E_1 & \text{for } t_0 \le t \le t_1 \\ E_2 & \text{for } t_1 \le t \le t_2 \\ \vdots \end{cases} \tag{4.18}$$

The information from the previous condition is not just lost with a new jump but at any time (a so-called *kangaroo process* [68, 70]). Then the probability density for the duration of the occurrence of a given field strength, $\omega\,(t|E)$, is given by:

$$\omega\,(t|E) = \mu\,(E)\,e^{-\mu(E)t} \tag{4.19}$$

with the jump frequency $\mu(E)$. The auto correlation function for the field strength of

this stochastic process is:

$$\Phi(t) = \int_0^\infty dE\ E^2 W(E) \int_t^\infty dt'\ \mu(E) e^{-\mu(E)t'} \tag{4.20}$$

with $W(E)$ being the probability distribution function (section 4.1.3). The jump frequency $\mu(E)$, equation 4.19, is derived by setting the correlation function of the statistical process, equation 4.20, equal to the correct auto correlation function of the problem. The auto correlation function for a field produced by statistical independent perturbers including Debye shielding is given in [71] to be:

$$\Phi(t) = \frac{4\pi n_e e^2}{t}\sqrt{\frac{2m}{\pi k_B T}}\left[1 + \tau^2 - \sqrt{\pi}\tau\left(\tau^2 + \frac{3}{2}\right)e^{\tau^2}\mathrm{erfc}(\tau)\right] \tag{4.21}$$

with $\tau = \omega_{pl} t/\sqrt{2}$ and the error function

$$\mathrm{erfc}(\tau) = \frac{2}{\sqrt{\pi}}\int_\tau^\infty e^{-t^2}\ dt \tag{4.22}$$

With this, the Schrödinger equation (4.5) can be solved exactly. The big advantage of this approach is that both, strong (Stark splitting) and weak (pressure broadening) collisions can be described. Moreover, through the superposition of two stochastic processes, the perturbation of electrons and ions can be calculated uniformly. Hence, the ion pressure broadening has not to be neglected. Based on this theory, Stehlé and Hutcheon have calculated and published Stark broadened spectral lines for several members of the Lyman and Balmer series for a wide density and temperature range [72, 73]. At present these profiles are the most accurate ones with an uncertainty of about 10% and widely accepted.

In Figure 4.2 a comparison of different Stark broadened Balmer line profiles calculated with the unified theory and MMM profiles published by Stehlé and Hutcheon are shown. The unified theory profiles have narrower line centres due to the ion pressure broadening which has to be neglected in this theory. This leads to broader line wings. In agreement with section 4.1.1 this effect becomes less important with higher upper principal quantum number. Considering further that the line centre is smeared out by folding the Stark profile with an additional Doppler profile, see section 4.2.2, the difference between the two theories becomes negligible for the higher members of the Balmer series.

4.2 Influence of other broadening mechanism

In addition to the Stark broadening there are other broadening mechanisms that have to be considered. The magnetic field present in a tokamak causes Zeeman splitting of the

energy levels, and the temperature of the emitting atom leads to Doppler broadening. Finally, the entrance slit of the spectrometer causes a line broadening referred to as the instrument function. In the following these mechanisms will be introduced and their influence with respect to the Stark broadening will be discussed.

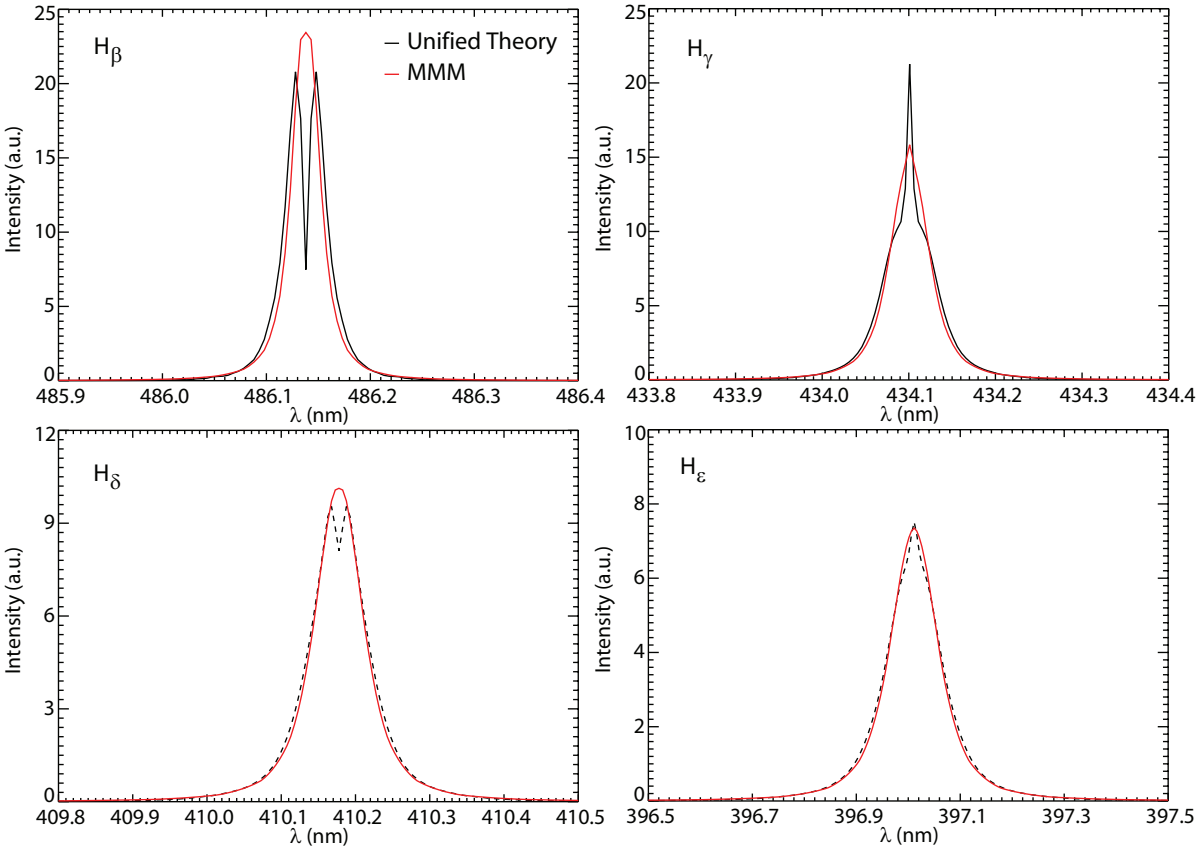

Figure 4.2: Stark profile of $n_e = 1 \cdot 10^{20}\,\mathrm{m}^{-3}$ for different Balmer lines calculated with the unified theory compared to the MMM profiles published by Stehlé [73].

4.2.1 Zeeman splitting

A magnetic field results in a splitting of the atomic energy levels and hence to a broadening of the spectral line. The corresponding Hamilton operator in equation 4.5 now depends also on the magnetic field ($H^{i,f}(E,B)$). The Schrödinger equation is then written as:

$$\left[H_0 + \frac{e}{2mc}\vec{B}(\vec{L}+2\vec{S}) + e\vec{E}\vec{r}\right]|\Psi\rangle = E\,|\Psi\rangle \tag{4.23}$$

$\vec{L}$ is the orbit angular momentum and $\vec{S}$ the spin.

Following the calculations of Nguyen-Hoe et. al. [63] this equation can be solved with first order calculation of perturbations. The result is an Eigenvalue equation for the

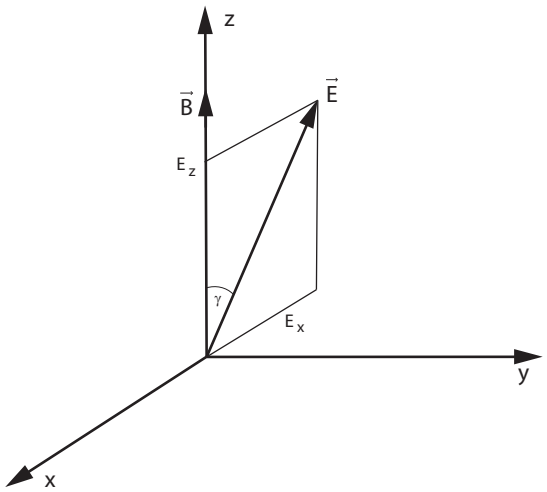

Figure 4.3: Geometry of the perturbation of an emitting atom due to a B-field and an E-field.

unperturbed states, which is for $\vec{B} = B_z$ (see Fig. 4.3) written as:

$$\underbrace{\left[\frac{L_z}{\hbar} + A\left(-\frac{x(1-(\cos\gamma)^2)^{1/2}}{a_0} + \frac{z\,\cos\gamma}{a_0}\right)\right]}_{K}|\Psi\rangle = \zeta\,|\Psi\rangle \tag{4.24}$$

γ is the angle between $\vec{E}$ and $\vec{B}$, see Fig. (4.3). It holds further:

$$A = \frac{ea_0E}{\hbar\omega_L} \qquad \omega_L = \frac{eB}{2mc} \tag{4.25}$$

$$\zeta = \frac{E - E_0^n}{\hbar\omega_0} - 1 \qquad E_0^n = -\frac{e^2}{2a_0}\frac{1}{n^2} \tag{4.26}$$

The state of an energy level $|\Psi\rangle$ can be written as a linear combination of states with different combinations of quantum numbers (with the new quantum number $i = l^2 + l + m + 1$):

$$|\Psi\rangle = \sum_{i=1}^{n^2} a^i\,|n,i\rangle \tag{4.27}$$

Then, equation 4.24 results in:

$$\sum_{i=1}^{n^2}(K-\zeta)\,a^i\,|n,i\rangle = 0 \tag{4.28}$$

Solving this $n^2 \times n^2$ Eigenvalue equation yields n^2 Eigenvalues ζ describing the energy of the perturbed levels. For each Eigenvalue ζ there are n^2 Eigenvectors a^i spanning the state of the perturbed levels (eq. 4.27). With this, equation 4.9 can be solved for the case of an additional uniform magnetic field.

In Figure 4.4 profiles of different Balmer lines calculated for typical parameters of ASDEX Upgrade divertor plasmas with and without additional Zeeman splitting are shown. The influence of the Zeeman splitting on the line broadening can be neglected for the higher members of the Balmer series.

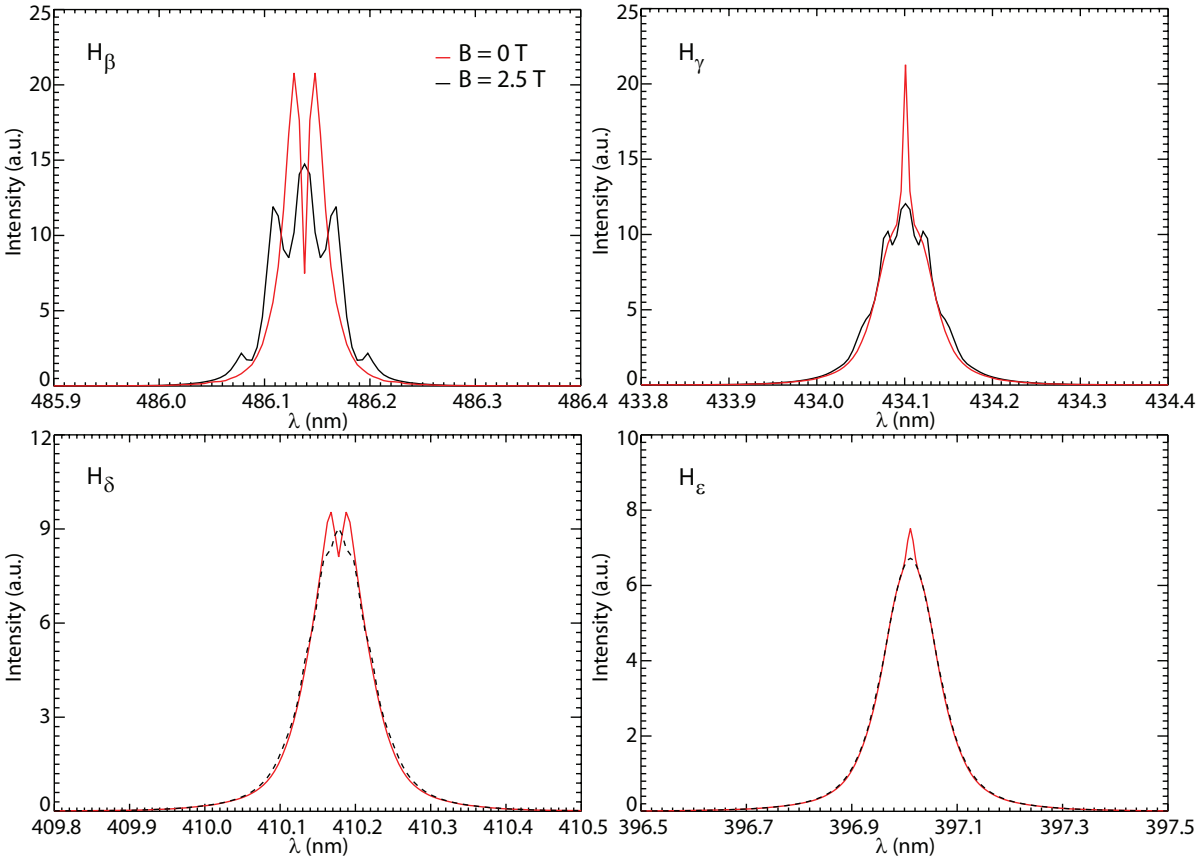

Figure 4.4: Stark profile of $n_e = 1 \cdot 10^{20}\,\mathrm{m}^{-3}$ for different Balmer lines calculated with the unified theory with and without an additional magnetic field of $B = 2.5\,\mathrm{T}$.

4.2.2 Doppler broadening

Besides the Stark broadening and the Zeeman splitting there is also the Doppler broadening influencing the line profile. The Doppler broadening is caused by the thermal motion of the emitting neutral particles with temperature T_n. In a thermal equilibrium the velocity distribution is a Maxwellian and the spectral intensity distribution is given by:

$$I(\lambda) = \frac{1}{\sqrt{\pi}\,\gamma} \exp\left[-\left(\frac{\lambda - \lambda_0}{\gamma}\right)^2\right] \qquad \gamma = \lambda_0 \sqrt{\frac{2k_B T_n}{mc^2}} \tag{4.29}$$

In order to be able to evaluate n_e from the Stark broadening one is constrained to a fixed Doppler broadening. Therefore, $T_n = 5\,\mathrm{eV}$ is assumed, which is the maximum

Franck-Condon dissociation energy of recycled H_2 molecules. The Doppler broadening mainly influences the central part of the line, while the wings show still the pure Stark profile due to the weak $\Delta\lambda^{-5/2}$ decay. Nevertheless, in Figure 4.5 the FWHM of a Stark and Doppler broadened D_ϵ line is shown for various n_e and T_n values as an indication for the influence of the Doppler broadening on the Stark profile. For densities larger than $n_e \approx 4 \cdot 10^{19}\,\mathrm{m}^{-3}$ the FWHM is insensitive to small changes around $T_n = 5\,\mathrm{eV}$.

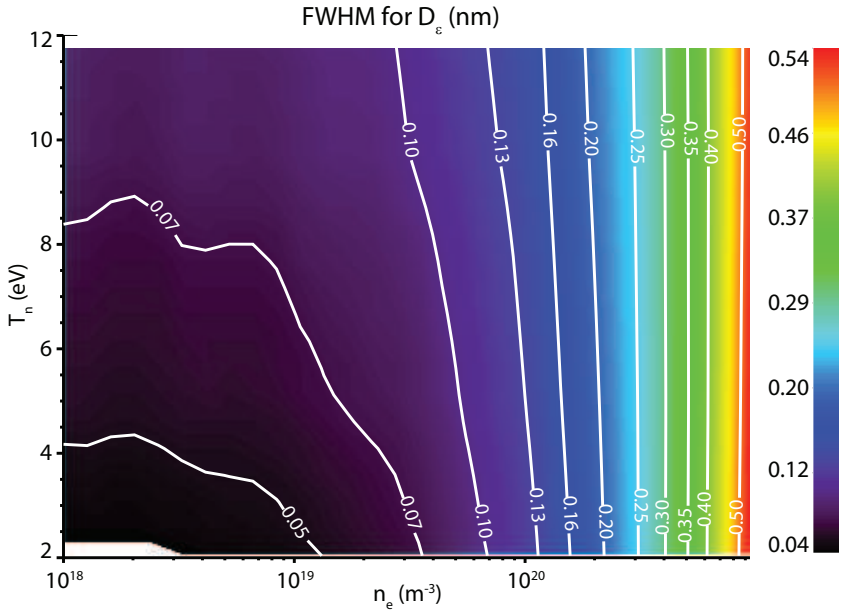

Figure 4.5: FWHM of a Stark and Doppler broadened D_ϵ line.

4.3 Diagnostic Setup and data evaluation

4.3.1 Diagnostic setup

Figure 4.6 shows the geometry of the lines of sight (LOS) in the divertor of ASDEX Upgrade used for the Stark broadening measurement. This setup allows the determination of n_e in the inner and outer divertor strike point region. The collected light is transmitted via optical fibres with a diameter of $d_f = 400\,\mu\mathrm{m}$ to a Czerny Turner like spectrometer. For this work, two identical spectrometers were available. The polished ends of the fibres are mounted directly in front of the entrance slit of the spectrometer. The light is then dispersed with a reflection grating of 2400 lines/mm and focused onto an EM-CCD camera. The spectrometer is equipped with commercial camera lenses. The collimating lense has a focal length f of 280 mm and an F-number of 4 while for the focusing lense these parameters are $f = 180\,\mathrm{mm}$ and $F = 2.8$. The different focal lengths yield a demagnification of 180/280 of the image on the CCD chip. The size of the CCD chip is 656 pixels in the horizontal and 496 pixels in the vertical direction with a pixel size

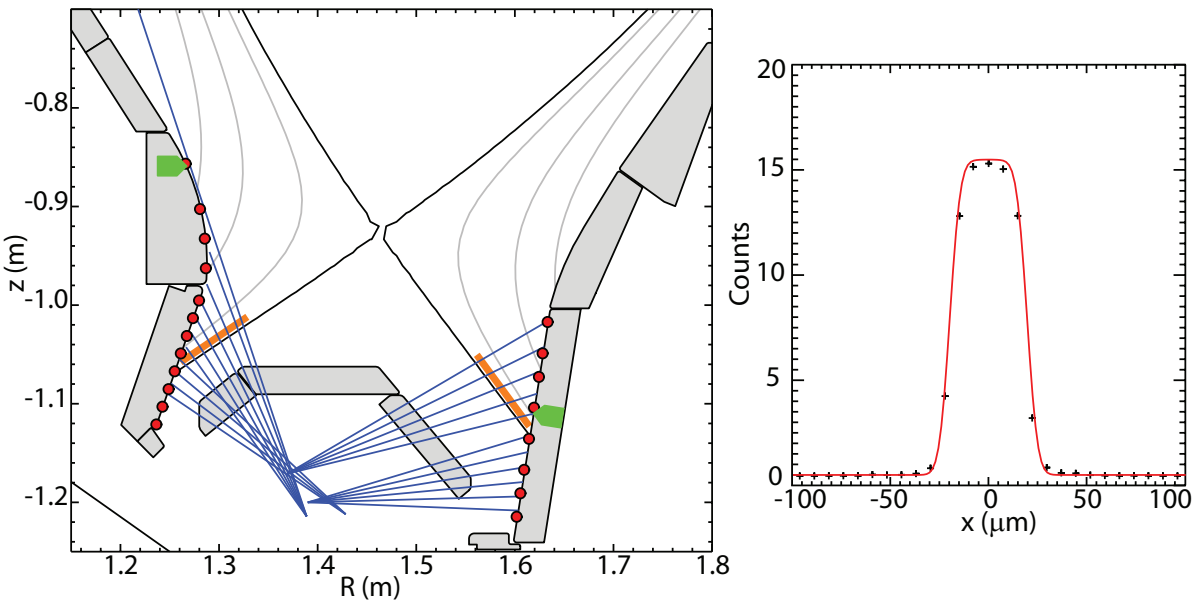

Figure 4.6: Left: Geometry of the LOS of the Stark diagnostic (blue). Also shown are pressure gauges (green) and Langmuir probes (red). Right: Instrument function for an entrance slit width of 50 μm.

of 7.4 μm $\times$ 7.4 μm. The wavelength resolution is $\Delta\lambda = 0.07$ nm/pixel at 400 nm and the imaged wavelength range is about 9 nm. With vertical binning a simultaneous measurement of 11 LOS with a time resolution of $\Delta t = 4$ ms can be achieved. When reading out just one LOS, the integration time can be decreased down to $\Delta t = 0.2$ ms. Furthermore the CCD camera is equipped with a 12 bit analog-to-digital converter. The entrance slit of the spectrometer is set to 50 μm, which gives a good compromise between the resolution and the signal strength. This yields a rectangular-shaped instrument function with a width on the CCD chip of about 0.4 nm, shown in Figure 4.6.

During this work, the CCD camera was replaced by a new one. The measurements shown in this section were made with the old camera characterized above. The measurements presented in chapter 5 were made with the new camera. This CCD chip has a size of 512 $\times$ 512 pixels and a pixel size of 16 μm $\times$ 16 μm. The wavelength resolution at 400 nm is $\Delta\lambda = 0.15$ nm/pixel and the imaged wavelength range is about 19.5 nm. This allows the simultaneous measurement of the D_δ and the D_ϵ line. Moreover, 25 LOS can be measured with a time resolution of 2.65 ms. In addition, also the number of LOS and hence, the covered area in the divertor was increased during this work (see Fig. 5.2).

4.3.2 Data evaluation

As shown in section 4.1.3 the wavelength shift $\Delta\lambda$ due to the Stark splitting becomes larger with higher upper principal quantum number. Measuring the higher members of the Balmer series therefore makes less demands on the spectral resolution of the

spectrometer. As a compromise between high Balmer series member and a good signal to noise ratio, the D_δ or the D_ϵ line is used by default for the density evaluation.

Furthermore, it was shown that the Zeeman effect can be neglected when measuring the higher Balmer lines (section 4.2.1). As the MMM profiles published by Stehlé [73] are widely accepted and, in the case of the higher Balmer lines, similar to the profiles obtained with the unified theory (section 4.1.4), the MMM profiles are used and the Zeeman splitting is neglected.

Theoretic profiles of the Stark broadened Balmer line are calculated for 28 different densities in the wavelength range of interest between $1 \cdot 10^{19}\,\mathrm{m}^{-3} < n_e < 1 \cdot 10^{22}\,\mathrm{m}^{-3}$. These calculated profiles are then convoluted with the Doppler broadened Gaussian profile corresponding to $T_n = 5\,\mathrm{eV}$ (section 4.2.2) and the instrument function. The profile of an arbitrary density value is obtained by a linear interpolation between these calculated profiles. When additional impurity lines appear within the spectrum they are also taken into account. They are modelled as a convolution of the Doppler profile with the instrument function only. All profiles are normalized to intensity $I = 1$. This theoretic spectrum is then fitted to the measured data using a *least squares* method where n_e, as well as the intensities of the lines, the position of the Balmer line and the background radiance are fit parameters. The positions of the impurity lines are fixed with respect to the Balmer line. Figure 4.7 shows an example of such a fit on the D_ϵ line. In addition to the Balmer line ($\lambda_{D_\epsilon} = 396.90\,\mathrm{nm}$) there is a nitrogen line ($\lambda_{NI} = 395.59\,\mathrm{nm}$), a helium line ($\lambda_{HeI} = 396.47\,\mathrm{nm}$), an oxygen line ($\lambda_{OII} = 396.21\,\mathrm{nm}$) and an oxygen multiplet ($\lambda_{OI} = 395.44\,\mathrm{nm}$; $397.33\,\mathrm{nm}$; $398.27\,\mathrm{nm}$) within the regarded wavelength range. The $\Delta\lambda^{-5/2}$ decay of the D_ϵ line, which is characteristic for the Stark broadening (section 4.1.3), can bee clearly seen in Figure 4.7.

Stehlé and Hutcheon claim an uncertainty of about 10% in their profiles. With the additional sources of error, such as the neglect of the Zeeman splitting, an uncertainty of this measurement of about 15% is expected. The lower measurement range is set by two constraints. On the one hand, as shown in section 4.2.2, at densities below $n_e \approx 4 \cdot 10^{19}\,\mathrm{m}^{-3}$ the Doppler profile becomes comparable to the Stark profile. Thus this is the lowest measurable density. On the other hand the divertor must be in the medium to high recycling regime to obtain a reasonable signal to noise ratio of the higher Balmer lines. Finally, it should be noted that, while this is in principle a line integrated measurement, the density measurement is localized to regions where the D_ϵ emissivity is highest. Furthermore, as the measured profile is a convolution of the local Stark broadened profiles, the density which is measured exists somewhere along the line of sight and is not the sum of the local densities.

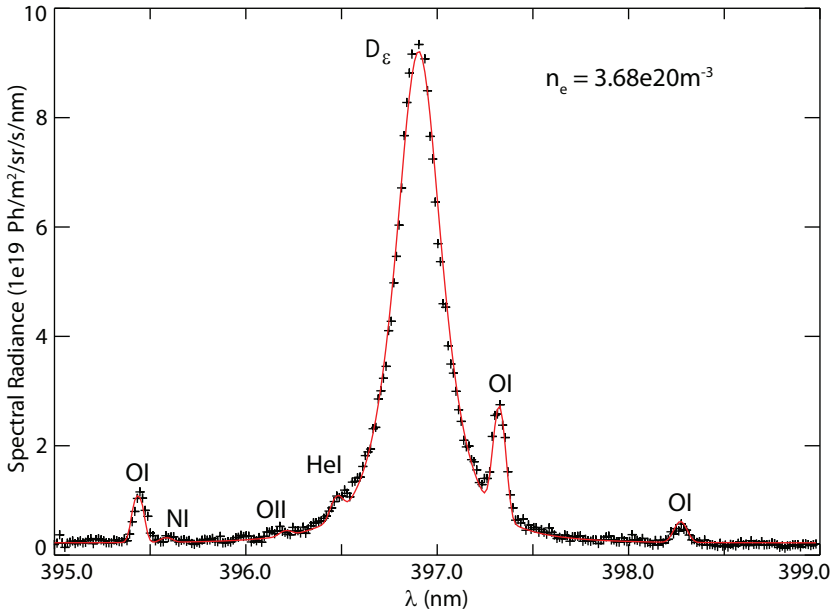

Figure 4.7: Example fit to the D_ϵ line yielding n_e.

4.3.3 Reflection issue

Since 2007 the plasma facing surfaces of ASDEX Upgrade have been completely covered with Tungsten [74], which has a high reflectivity not only for complete but also for diffusive reflection ($R_{tot} \approx 35 - 40\%$, [75]). This seriously disturbed the initial attempts to measure the Balmer lines. Under normal operation the density as well as the radiance of the Balmer line is about one order of magnitude higher in the inner divertor than in the outer divertor (see section 4.4.1). This caused the LOS observing the outer divertor mainly to detect the radiance originating from the inner divertor that was reflected off of the outer target. Therefore a much too high n_e was determined in the outer divertor. To address this problem, the LOS in the outer divertor were rearranged such that they end in a viewing dump between two tiles. This strongly reduces the detection of stray radiation. To document this enhancement a discharge in which n_e was determined with the old LOS setup was repeated with the new LOS setup. Figure 4.8 shows a comparison of an example fit to the D_ϵ line measured with the new and old LOS setups. It can be seen that the radiance of D_ϵ as well as the resulting density is considerably lower with the new LOS setup.

4.4 Consistency check

In this section initial measurements are presented and it is shown that the obtained density values as well as the emissivity of the Balmer line are consistent with other diagnostics.

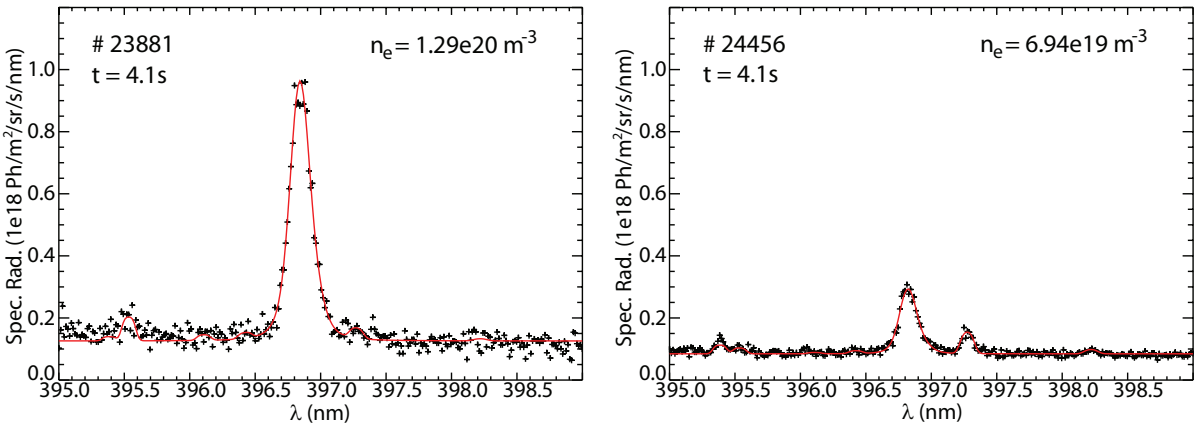

Figure 4.8: Fit to the D_ϵ line measured with the old (left) and new (right) LOS setup for two identical discharges.

4.4.1 Comparison with Langmuir probes

ASDEX Upgrade is equipped with an extensive set of static Langmuir probes, LP, in the inner and outer divertor target (see Fig. 4.6). LPs are used to measure n_e and T_e at the target. Here, n_e obtained from SBD is compared with n_e from LP. Therefore a lower Single Null L-mode discharges with lower triangularity $\delta = 0.36$ was performed. It had a plasma current of $I_p = 0.8\,\mathrm{MA}$, a toroidal magnetic field of $B_t = -2.5\,\mathrm{T}$, a line averaged core plasma density of $\bar{n}_e = 4.5 \cdot 10^{19}\,\mathrm{m}^{-3}$, an additional heating power of 1.4 MW and a safety factor of $q_{95} = 5$. During this discharge strike point sweeps were performed to enhance the spatial resolution of the SBD and LP measurement. The outer divertor was in the medium recycling, conduction limited regime as the target temperature was $T_e \approx 20\,\mathrm{eV}$. The temperature at the inner divertor target was below $T_e < 3\,\mathrm{eV}$ and thus, the inner divertor was in the detached regime. This can also be seen in the total radiation distribution measured by foil bolometers (Fig. 4.9). The radiation front in the inner divertor, which is approximately the recycling front, has moved to the X-point, indicating that the plasma is detached from the inner target (see section 2.2.3).

In Figure 4.9 n_e from SBD and LP as well as the radiance of the D_ϵ line versus the ΔS coordinate is shown. The ΔS coordinate is the poloidal distance from the strike point along the divertor surface. Positive values are in the scrape-off-layer, SOL, negative values are in the private flux, PF, region. It must be noted here that the intersection of the LOS and the target is taken as the LOS position throughout this work. The correct coordinate of the LOS would be the position along the LOS where the D_ϵ radiation is highest, which is unknown, however. As the radiation is emitted somewhere in the SOL between the separatrix and the divertor target, the correct LOS coordinate is between the ΔS coordinate along the divertor surface and the poloidal distance from the strike point along the separatrix (both are indicated by the orange lines in Figure 4.6).

In the outer divertor a good agreement is obtained between n_e at the strike point from SBD and LP. The fact that the shapes of the density profiles do not match is caused by the line integrated SBD measurement discussed above.

The hydrogen ionization rate coefficient for $T_e = 20\,\text{eV}$ and $n_e = 4 \cdot 10^{19}\,\text{m}^{-3}$, see Figure 3.1, is $\langle \sigma v_e \rangle = 2.2{\cdot}10^{-14}\,\text{m}^3/\text{s}$. With a temperature of the neutral deuterium of $T_n = 5\,\text{eV}$, see section 4.2.2, the mean free path of neutrals is approximately $\lambda_{mfp} \approx 3\,\text{cm}$. Thus, the region where the recycled neutrals ionize expands from the divertor target into the SOL along a narrow region close to the separatrix where the temperature is highest (see also the total radiation distribution, Fig. 4.9). The SBD measures therefore the density distribution from the strike point at the target approximately along the separatrix into the divertor volume. In this case, the density in this region is almost constant. This is expected, the fan, formed by the SBD lines of sight, observes a region around the separatrix (orange line in Fig. 4.6), which has an extent on the order of $\lambda_{mfp} \approx 3\,\text{cm}$, leading to a flat n_e profile. The Langmuir probes, in contrast, measure the density at the target and yield therefore a decay of n_e outside the ionization front. The SBD diagnostic can therefore be used to determine the density distribution in the divertor volume.

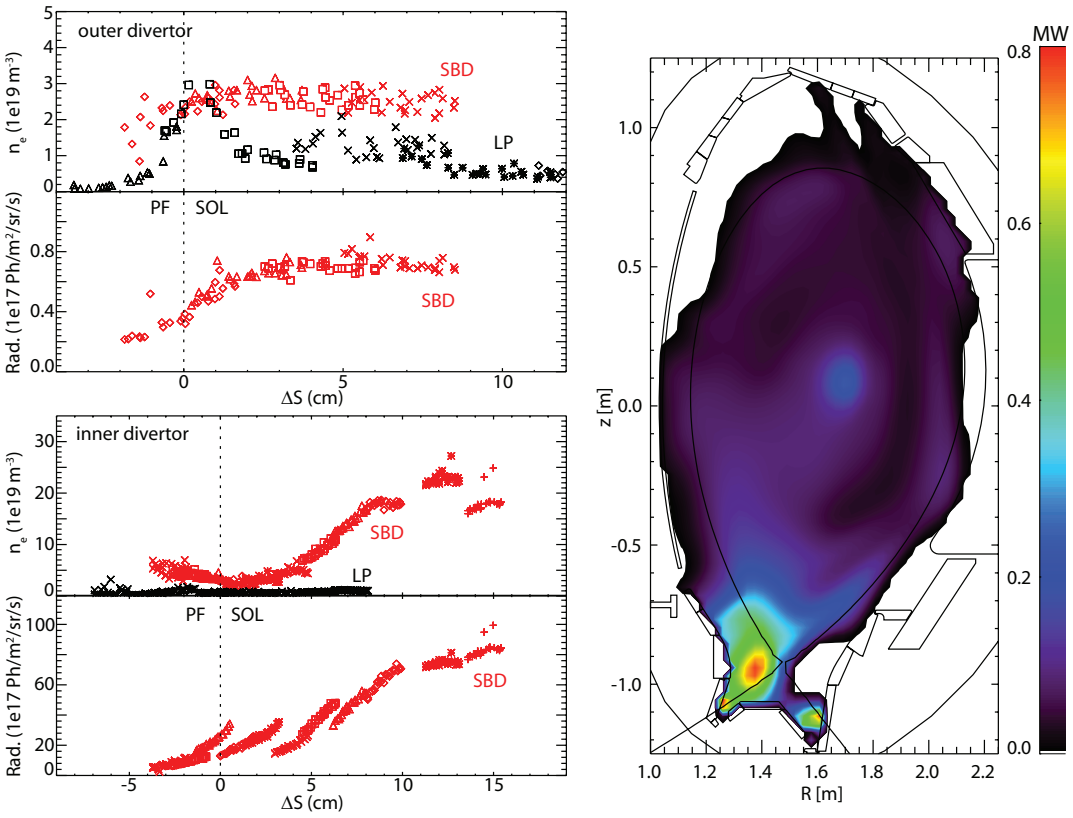

Figure 4.9: Left: n_e measured by SBD (red) and LP (black) and D_ϵ radiance for the outer and inner divertor. The different symbols indicate different LOS and probes, respectively. Right: Total radiation distribution measured by bolometers of discharge #24456.

In the detached inner divertor there is no agreement between n_e from SBD and LP. In

fact, the peak n_e measured by SBD of $\approx 2.3 \cdot 10^{20}\,\mathrm{m}^{-3}$ is about two orders of magnitude higher than n_e from LP at the target and about one order of magnitude higher than the core plasma density. This result is expected as in detached conditions the pressure and hence n_e in front of the target reaches very low values, see section 2.2.3. The region of highest n_e is retracted from the target and in the divertor volume, as discussed in section 2.2.3. This is also confirmed by the distribution of the total radiation (Fig. 4.9). Moreover, high values for n_e in the detached divertor volume which are one order of magnitude higher than the core plasma density has also been previously observed at JET [76].

4.4.2 Comparison with pressure gauges

Finally, SBD measurements are compared to measurements from fast ionization gauges, ION. These gauges measure the neutral flux density Γ_{D^0} [77] at different positions. The gauges of interest are shown in Figure 4.6. In attached conditions, Γ_{D^0} at the divertor target can also be derived from the SBD measurements with the S/XB method, introduced in section 3.6:

$$\Gamma_{D^0} = \frac{S}{XB_{D_\epsilon}}\Gamma_{\gamma,D_\epsilon} \tag{4.30}$$

The radiance $\Gamma_{\gamma,D_\epsilon}$ is derived by projecting the D_ϵ emission along the LOS onto the surface normal. Then it is multiplied by 4π, accounting for homogeneous emission in the full solid angle. In order to obtain the S/XB value, which depends on the electron density and temperature, T_e has been taken from LP and n_e from SBD.

In Figure 4.10a Γ_{D^0} measured by the outer divertor ionization gauge and calculated with the S/XB method for the LOS closest to this gauge are shown. There is a good agreement between both flux densities, which shows that the density and the D_ϵ emission measured by the Stark broadening diagnostic is consistent with the ionization gauge measurement. In the inner divertor, shown in Figure 4.10b, Γ_{D^0} calculated with the S/XB method is about two orders of magnitude larger than Γ_{D^0} measured by the gauge. This result is expected as the inner divertor is in the detached regime. Here, recombination dominates with respect to the ionization (see section 3.2). Therefore, the α/RB value, shown in Figure 3.6b, has to be taken. The calculated Γ_{D^0} from the spectroscopy and the measured one are shown in Figure 4.10c. Although there is an uncertainty of T_e, as it was taken again from the Langmuir probes at the target, a reasonable good agreement of Γ_{D^+} and Γ_D is obtained. This shows that the inner divertor is recombination dominated. Furthermore, the SBD measurements are also consistent with the ionization gauge measurements in detached conditions where a comparison with the Langmuir probe measurements is not possible. The SBD diagnostic can therefore be used to evaluate the electron density in the detached divertor volume. It should be noted here that

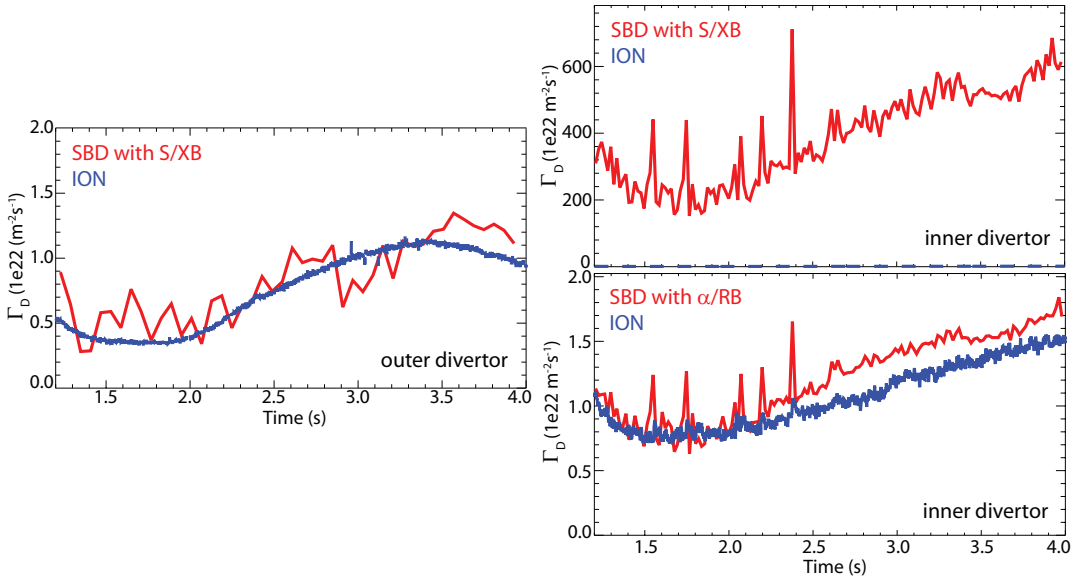

Figure 4.10: Time traces of Γ_{D^0} measured by ionization gauges and calculated from SBD measurements for the inner and outer divertor of discharge #24456.

the evaluation of the neutral flux density with the α/RB method was done for the first time.

Chapter 5

Experimental investigations on divertor detachment

In this chapter the experimental results concerning divertor detachment will be shown. Before presenting the obtained classification of divertor detachment in section 5.2, the setup of the discharges and the diagnostics used will be introduced in section 5.1. Thereafter, in section 5.3, the effect of N_2 seeding and of a magnetic perturbation field on the detachment process as well as the observation of divertor plasma oscillations will be shown.

5.1 Experiment and diagnostic Setup

5.1.1 Discharge setup

A series of ohmic and L-mode density ramp discharges has been performed at ASDEX Upgrade to study the detachment of the divertor. Since 2007, the plasma facing surfaces of ASDEX Upgrade are completely covered with tungsten [74]. All discharges of this series were in lower single null divertor configuration with a lower triangularity of $\delta = 0.36$, a plasma current of $I_p = 1\,\mathrm{MA}$, a toroidal magnetic field of $B_t = 2.5\,\mathrm{T}$ and a safety factor of $q_{95} \approx 4$. The electron cyclotron resonance heating, ECRH, power was varied from discharge to discharge. The fuelling species was changed between deuterium and hydrogen and the field direction was changed between forward field (ion $\mathbf{B} \times \nabla\mathbf{B}$ drift towards the lower divertor, sec. 2.3.2) and reversed field, see Table 5.1. Due to the alignment of the divertor tiles, the magnetic helicity has to remain constant. Thus B_t and I_p have to be changed simultaneously in reversed field operation. Within one shot additional nitrogen was puffed into the divertor, in order to trigger the detachment via removal of power in the SOL by impurity line radiation. Another discharge was performed with an externally applied magnetic perturbation, MP, field (Tb. 5.1).

Table 5.1: Table of plasma parameters that were varied during the series of density ramp discharges.

shot #	P_{ECRH}[kW]	Gas	Field	special
27098	0	D	forward	
27099	400	D	forward	
27100	600	D	forward	
27101	900	D	forward	
27102	900	D	forward	MP field
27326	600	D	forward	N_2 seeding
27283	0	D	reversed	
27284	900	D	reversed	
27286	1300	D	reversed	
27360	0	H	forward	
27361	1000	H	forward	

In Figure 5.1 time traces of various plasma parameters for the discharge #27100 are shown. The current flat top was reached at 1.3 s and a stable magnetic configuration at 1.8 s. The strike point positions where then kept constant within a tolerance of 1 cm, see Figure 5.1b. This magnetic configuration in the divertor is shown in Figure 5.2. Also shown in Figure 5.2 is what will be called later on the inner and outer scrape-off layer, namely the high and low field side divertor SOL, respectively. The strike point positions had to be kept constant to measure the time evolution of the divertor plasma with fixed geometry in order to exclude any geometric effects during the evolution of the detachment. The gas fuelling ramp starts 150 ms after the stable magnetic configuration has been reached. The gas input was thereby increased from $1 \cdot 10^{21}$ up to $1 \cdot 10^{22}$ atoms/s with a rate of $1 \cdot 10^{21}$ atoms/s^2. Then the rate was increased to $3 \cdot 10^{21}$ atoms s^{-2} and the fuelling was ramped up until the density limit occurred. The fuelling ramp leads to a continuous increase of the plasma density and to the development of the detachment in the divertor. This fuelling scheme was not changed within the series of discharges except for the one with additional nitrogen seeding.

5.1.2 Diagnostic setup

Flush mounted Langmuir triple probes measure the ion saturation current density, j_{sat}, and the electron density, $n_{e,t}$ and temperature, $T_{e,t}$ at the divertor targets at the positions shown in Figure 5.2a. The ion flux, Γ_{D^+}, is then calculated dividing j_{sat} by the elementary charge e, assuming pure deuterium plasmas. The spatial probe separation in poloidal

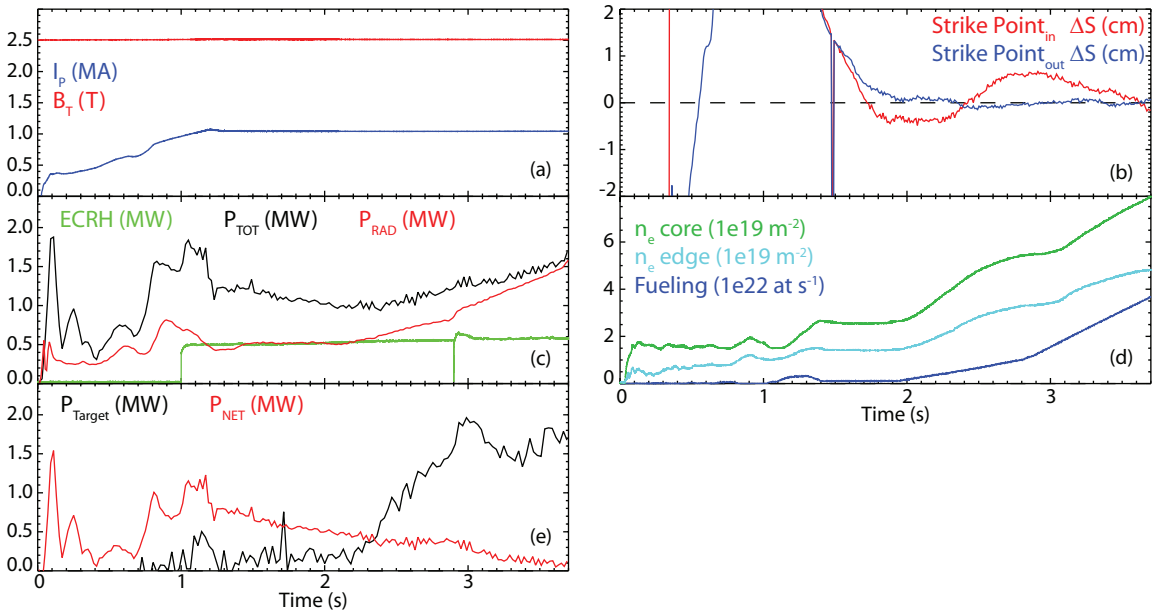

Figure 5.1: Time traces of a representative discharge #27100. Plasma current (blue) and toroidal magnetic field (red) (a), relative positions of the inner (red) and outer (blue) strike point position (b), applied ECRH power (green), total heating power including ohmic heating (black) and total radiated power (c), plasma fuelling (blue), central (green)and peripheral (cyan) line integrated plasma density (d), net power to the divertor targets (red) and total power at the inner and outer target (black) measured by IR.

direction is $\approx 2\,\mathrm{cm}$ in the inner and $\approx 2.5\,\mathrm{cm}$ in the outer divertor. The temporal resolution is $\Delta t = 0.035\,\mathrm{ms}$. The electron density in the divertor volume is determined with the SBD diagnostic [58], see section 4.3.1. The geometry of the extended line of sight setup is also shown in Figure 5.2a.

Fast AXUV diode bolometers measure the radiation between 1 eV and 8 keV [78]. This measurement is not absolutely calibrated and has a time resolution of 200 kHz. The positions of the the bolometer chords as well as the ionization gauges are shown in Figure 5.2b. When these experiments were carried out, the interesting gauges behind the inner and outer divertor (see sec. 4.4, fig. 4.6) were out of order.

In principal, the power flux onto the divertor targets can be calculated from the Langmuir probe measurements according to equation 2.12. However, as mentioned in section 2.1.2, the absolute value of the sheath heat transmission factor γ is not well known and varies for different divertor operating regimes. The target power flux density is in addition routinely measured by an infrared camera (IR). In low recycling divertor conditions this measurement can be used to deduce γ [16]. But, in high recycling or especially in detached conditions the IR measurement does not work anymore. The IR camera measures light at a wavelength of $4.7\,\mu\mathrm{m} \pm 1\,\mu\mathrm{m}$. In this range, there also exists a deuterium line of the Pfund series ($n = 7 \rightarrow n = 5$) at $\lambda = 4.65\,\mu\mathrm{m}$. On top of

this, there are also molecular deuterium bands present in this spectral IR range. With the transition from attached to detached conditions, the neutral density in the divertor increases and therefore, the atomic and molecular deuterium radiation increases. In addition, recombination can become dominant, which preferably populates the higher n-states such as the upper level of this Pfund-line. The target temperature (and therefore the IR emission from the target) decreases, however, and is then strongly disturbed by this stray radiation. In order to verify this, one can make a power balance. In Figure 5.1e the net power to the divertor targets, P_{net}, and the total power P_t on the inner and outer target measured by IR is shown. The net power is given by $P_{net} = P_{tot} - \mathrm{d}W/\mathrm{d}t - P_{rad}$, where P_{tot}, P_{rad} (Fig. 5.1c) are the total heating power including ohmic heating and the total radiated power measured by bolometry, respectively, and $\mathrm{d}W/\mathrm{d}t$ is the change of the stored energy. P_t is derived by integrating the power flux density over the entire target in poloidal and toroidal direction. It can bee seen, that at $t \approx 2.3\,\mathrm{s}$ P_t exceeds P_{net}. This is physically impossible and most likely the effect of the mentioned stray radiation. Therefore, no target heat flux measurements are discussed in the following.

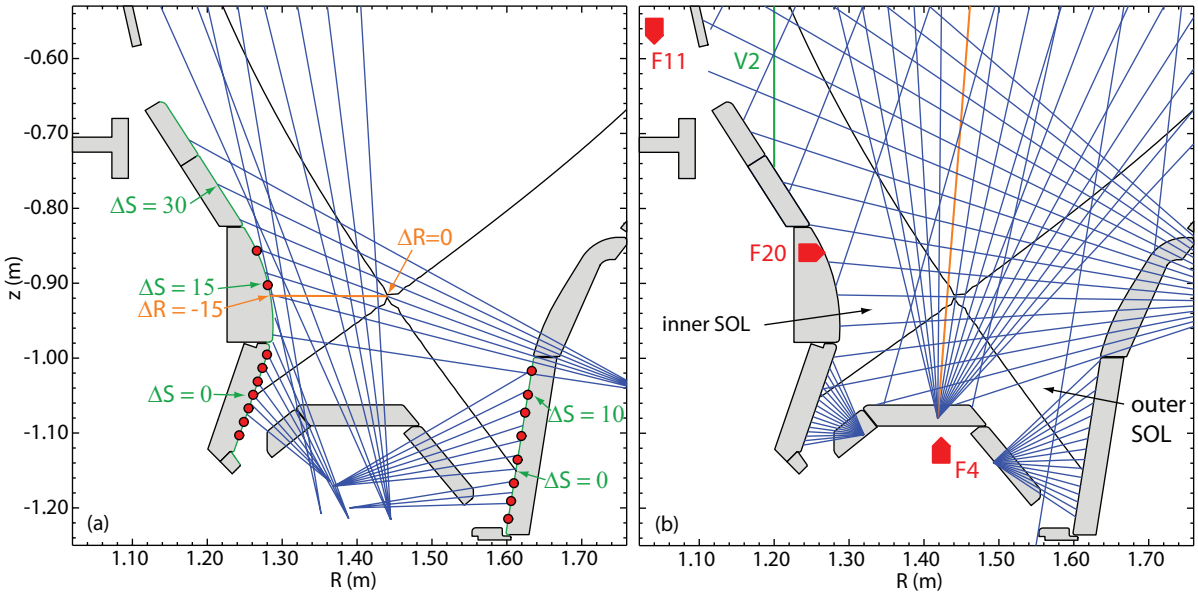

Figure 5.2: (a): LOS for Stark broadening (blue) and fixed Langmuir probes (red). Also shown is the ΔS and ΔR coordinate. (b): AXUV LOS (blue), ionization gauges (red) and vertical interferometer chord (green).

5.1.3 The degree of detachment

Similar to a previous work at JET [79] the notation of degree of detachment, DOD, is used as a marker for the onset and the magnitude of detachment. It is defined as the ratio of the calculated ($\Phi_{D^+}^{\mathrm{calc}}$) and measured ($\Phi_{D^+}^{\mathrm{meas}}$) ion flux to the target. Following the simple Two-Point-Model, the ion flux reaching the divertor target is proportional to the square

of the upstream separatrix density n_u^{sep}, see section 2.2.2 and equation 2.28. Furthermore, for Ohmic and L-Mode discharges it has been shown that n_u^{sep} scales approximately linearly with the line integrated plasma density, $\bar{n}_e$ [80]. Therefore $\Phi_{D^+}^{\mathrm{calc}}$ is deduced from a horizontal edge interferometer measurement and the degree of detachment is then calculated as:

$$\mathrm{DOD} = \frac{\Phi_{D^+}^{\mathrm{calc}}}{\Phi_{D^+}^{\mathrm{meas}}} = \frac{C_1 \cdot \left(n_u^{sep}\right)^2}{\Phi_{D^+}^{\mathrm{meas}}} = \frac{C \cdot \bar{n}_e^2}{\Phi_{D^+}^{\mathrm{meas}}} \tag{5.1}$$

The total ion flux to the entire target is obtained by integrating over all Langmuir probe measurements along the divertor surface:

$$\begin{aligned} \Phi_{D^+}^{\mathrm{meas}} &= 2\pi \int \Gamma_{D^+}(S) R(S)\, dS \\ &\approx 2\pi \sum_{iprobes} \Gamma_{D^+}(i) R(i) \cdot \left(\frac{S\,(i+1) - S\,(i-1)}{2} \right) \end{aligned} \tag{5.2}$$

It should be noted that the large separation between the third and the second uppermost probe in the inner divertor (Fig. 5.2a) results in an additional uncertainty of $\Phi_{D^+}^{\mathrm{meas}}$. To determine the two constants C in Eq. 5.1 for the inner and outer divertor, the mean values of $\Phi_{D^+}^{\mathrm{meas}}(1.8\,\mathrm{s} < t < 1.9\,\mathrm{s})$ before the fuelling ramp are set equal to $\Phi_{D^+}^{\mathrm{calc}}$. At this time the inner divertor is already in a high recycling regime although this is the lowest achievable main plasma density in these density ramp discharges.

When the divertor plasma can be described by the simple Two-Point-Model, then $\Phi_{D^+}^{\mathrm{calc}} = \Phi_{D^+}^{\mathrm{meas}}$ and $\mathrm{DOD} = 1$. The main assumptions of the model are that there is no significant energy and pressure loss along a field line, see section 2.2.2. Simply speaking, when the pressure drops along a field line, hence detachment begins, $\Phi_{D^+}^{\mathrm{meas}}$ becomes less than $\Phi_{D^+}^{\mathrm{calc}}$ and $\mathrm{DOD} > 1$.

There could be other mechanisms leading to a less steep rise of $\Phi_{D^+}^{\mathrm{meas}}$ compared to the TPM scaling such as e.g. a change of the ratio between conducted and convected heat flux, see equations 2.23 and 2.28. Therefore the onset of detachment at JET was defined when the DOD calculated with the peak ion flux becomes larger than 2 while the DOD calculated with the integrated ion flux is below 2. For this work, in contrast, the onset of detachment is defined when $\Phi_{D^+}^{\mathrm{meas}}$ rolls over. The DOD is only used as a guide line, as it will be shown that the roll over of $\Phi_{D^+}^{\mathrm{meas}}$ does not necessarily coincide with the condition of the degree of detachment being lower than one.

5.2 Evolution of divertor detachment - the three detachment states

The main observation of this work is that the detachment process in ohmic and L-mode can be divided into three different states. In the first state, which will be called the *onset state*, the first deviation from the simple Two-Point-Model scaling occurs. In the second one, the *fluctuating state*, radiative fluctuations in the inner SOL close to the X-point occur. When these fluctuations vanish, complete detachment over a large target area sets in, giving this third state the name *complete detachment state*. Furthermore, the characteristics of these states are a combination of both the inner and outer divertor conditions, meaning that the behaviour of both divertors is coupled. These divertor conditions will be described in the following for forward field direction and deuterium fuelling (section 5.2.1), for forward field direction and hydrogen fuelling (section 5.2.2) and for reversed field direction and deuterium fuelling (section 5.2.3).

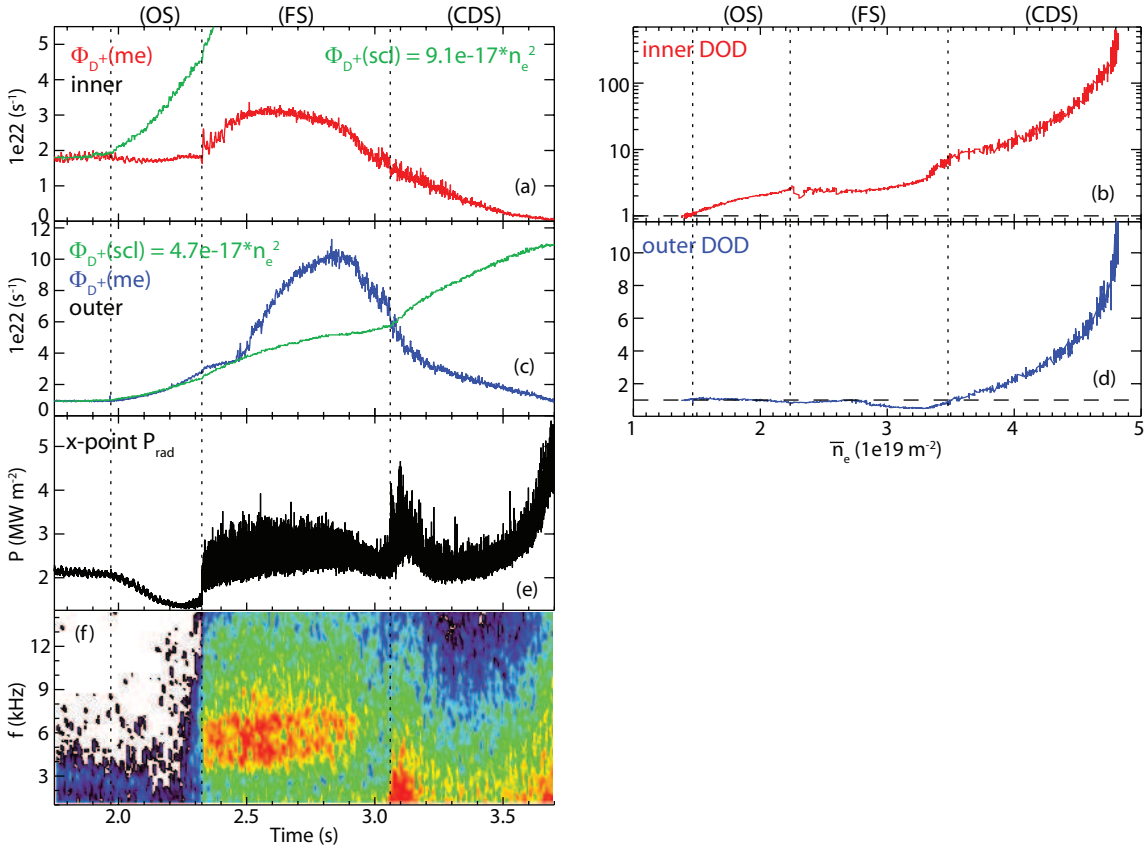

Figure 5.3: Left: Calculated and measured total ion flux to the inner (a) and outer target (c), line integrated radiated power (e) measured by an AXUV diode (orange chord in Figure 5.2b) and its power spectrum (f). Right: DOD as a function of the line integrated peripheral plasma density for the inner (b) and outer (d) divertor of discharge #27100. Note the logarithmic scale of (b). The three detachment states (OS), (FS) and (CDS) are marked.

5.2.1 The three detachment states in forward field

In the following, the evolution of detachment in the inner and outer divertor with forward field direction is described. Representative for all discharges of this series, which are made in forward field, measurements of the discharge #27100 (Fig. 5.1, Tb. 5.1) are shown. The absolute values presented here are only valid for this specific discharge. The qualitative trends of the various parameters during the three detachment states are, however, valid for all discharges made in forward field with deuterium.

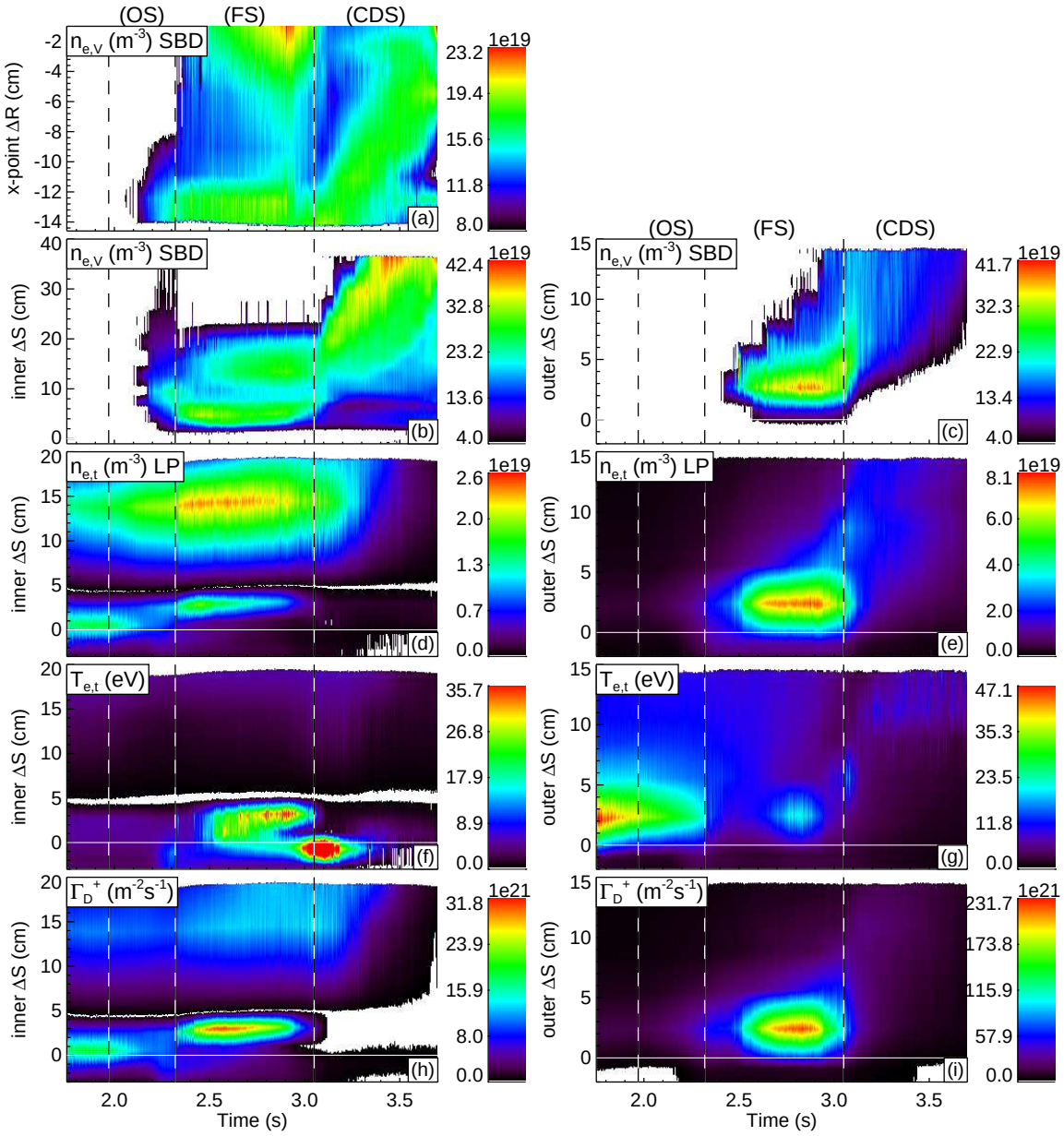

Figure 5.4: Horizontal (a) and vertical (b,c) line integrated $n_{e,V}$ profile in the divertor volume and $n_{e,t}$ (d,e), $T_{e,t}$ (f,g) and Γ_{D^+} (h,i) target profiles in the inner and outer divertor, respectively, of discharge #27100. The three detachment states are marked.

Figure 5.3 shows the measured and scaled temporal evolutions of Φ_{D^+} and the corresponding DOD as a function of the line integrated peripheral plasma density of the inner and outer divertor. From this, the onsets of detachment of the inner and outer divertors are set to $t \approx 2\,\mathrm{s}$ ($\bar{n}_e \approx 1.5 \cdot 10^{19}\,\mathrm{m}^{-2}$) and $t \approx 2.85\,\mathrm{s}$ ($\bar{n}_e \approx 3.3 \cdot 10^{19}\,\mathrm{m}^{-2}$), respectively. Before the onset of the inner divertor detachment at $t < 2\,\mathrm{s}$, Φ_{D^+} to the inner divertor is higher than that to the outer divertor. The ratio of both corresponds to the ratio of the constants C, see Figure 5.3a,b: $\Phi^{in}_{D^+}/\Phi^{out}_{D^+} = 9.1/4.7 = 1.9$

The target profiles of $n_{e,t}$, $T_{e,t}$ and Γ_{D^+} measured by LP and the line integrated density profiles in the divertor volume measured by SBD as a function of time are shown in Figure 5.4. The ΔR coordinate for the inner vertical SBD LOS in Figure 5.4a is the distance from the X-point along a horizontal line, the origin is at the X-point position and negative values are in the inner SOL (see Fig. 5.2a). Before the onset of the inner divertor detachment ($t < 2\,\mathrm{s}$) peak ion fluxes of $\Gamma_{D^+} \approx 2 \cdot 10^{22}\,\mathrm{m}^{-2}\mathrm{s}^{-1}$ close to the inner strike point and $\Gamma_{D^+} \approx 1.5 \cdot 10^{22}\,\mathrm{m}^{-2}\mathrm{s}^{-1}$ close to the outer strike point are measured, respectively. Their ratio of $\Gamma^{in}_{D^+}/\Gamma^{out}_{D^+} = 1.3$ is more symmetric than the total ion flux ratio of $\Phi^{in}_{D^+}/\Phi^{out}_{D^+} = 1.9$. This means that the inner ion flux profile is broader compared to the profile of the outer divertor which indicates that the inner divertor is already in a higher recycling regime, as mentioned above.

The electron density in the divertor volume is below the measurement range of $n_e > 4 \cdot 10^{19}\,\mathrm{m}^{-3}$ of the SBD in both the inner and outer divertor. This is expected as the density at the targets, measured by LP, is below $1.5 \cdot 10^{19}\,\mathrm{m}^{-3}$, which corresponds to a density at the recycling zone of $n_{e,V} \approx 2 \cdot n_{e,t} \approx 3 \cdot 10^{19}\,\mathrm{m}^{-3}$ (section 2.2.1, equation 2.19).

The onset of detachment state

The start of the onset state is defined when the first deviation from the Two-Point-Model scaling occurs. This happens in the inner divertor, see above, where the measured Φ_{D^+} increases less strongly than the TPM scaling.

Inner divertor During this state, the ion flux close to the inner strike point, $\Delta S \approx 1\,\mathrm{cm}$ rolls over and drops to $\Gamma_{D^+} \approx 1 \cdot 10^{22}\,\mathrm{m}^{-2}\mathrm{s}^{-1}$ with increasing upstream density (Fig. 5.4h). This is also visible in the total ion flux to the inner divertor which further deviates from the TPM scaling (Fig. 5.3a) and the DOD increases (Fig. 5.3b). Also $n_{e,t}$ close to the strike point decreases with increasing upstream density, but, in contrast, increases in the far SOL at $\Delta S \approx 14\,\mathrm{cm}$ up to $n_{e,t} \approx 2.3 \cdot 10^{19}\,\mathrm{m}^{-3}$ at the end of the onset state (Fig. 5.4d). This is consistent with the radiation distribution measured by foil bolometry, shown in Figure 5.5. The radiation is higher in the inner far SOL than close to the strike point. In addition, the electron density in the volume increases up

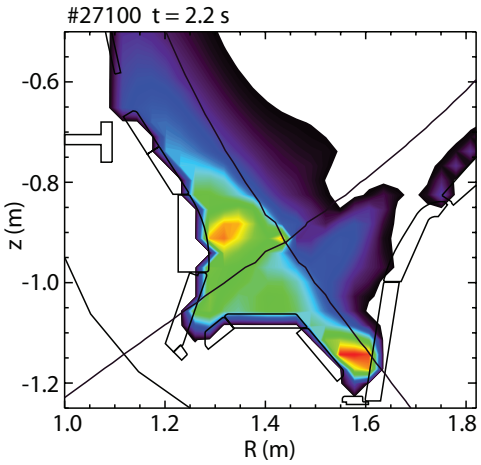

Figure 5.5: Total radiation distribution from foil bolometry in the divertor at one time point during the onset state for #27100.

to $n_{e,v} \approx 1.3 - 2.3 \cdot 10^{20}\,\mathrm{m}^{-3}$ (Fig. 5.4a,b). All in all, this indicates that the plasma is partially detached from the inner strike point region at the end of this state.

Outer divertor The outer divertor is still attached, in the conduction limited regime and follows the simple TPM (DOD= 1) throughout this state (Fig. 5.3b,d). With increasing upstream density, the maximum of Γ_{D^+} and $n_{e,t}$ increases during this state up to $4 \cdot 10^{22}\,\mathrm{m}^{-2}\mathrm{s}^{-1}$ and $1.4 \cdot 10^{19}\,\mathrm{m}^{-3}$, respectively, while $T_{e,t}$ drops to 25 eV (Fig. 5.4i,e,g). The electron density in the volume stays below $4 \cdot 10^{19}\,\mathrm{m}^{-3}$ (Fig. 5.4c).

The fluctuating detachment state

This state is defined by the appearance of radiative fluctuations which are situated close to the X-point in the inner SOL. During this state, the core plasma fuelling becomes less efficient. Although the amount of the fuelling gas is steadily increased, the core plasma density seems to saturate (Fig. 5.1d, $t \approx 2.9\,\mathrm{s}$). The characteristics of these fluctuations and the evolution of the divertor plasma parameters during this state are described in the following.

The X-point fluctuations The transition to this state is determined with a sudden onset of a fluctuation band of $f \approx 5.5\,\mathrm{kHz}$ (Fig. 5.3e,f), measured with the AXUV diodes, which is observed for the first time. The width of this fluctuation band is $\Delta f \approx 3\,\mathrm{kHz}$ and the amplitude is about 1.5 times the original radiation level, which can be seen in the time trace of an AXUV diode (Fig. 5.6). There is currently no other diagnostic available measuring with such a high sampling rate in the according region in order to trace these fluctuations back to the electron temperature or to the density or to a combination of both.

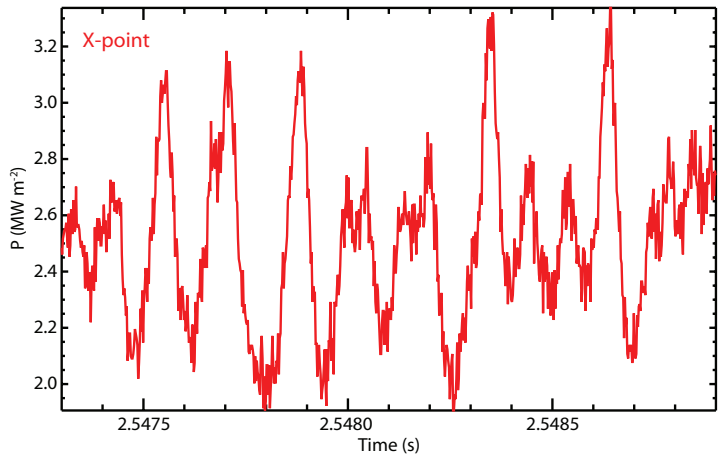

Figure 5.6: Temporal evolution of the radiative X-point fluctuations measured by an AXUV diode (orange chord in Figure 5.2b).

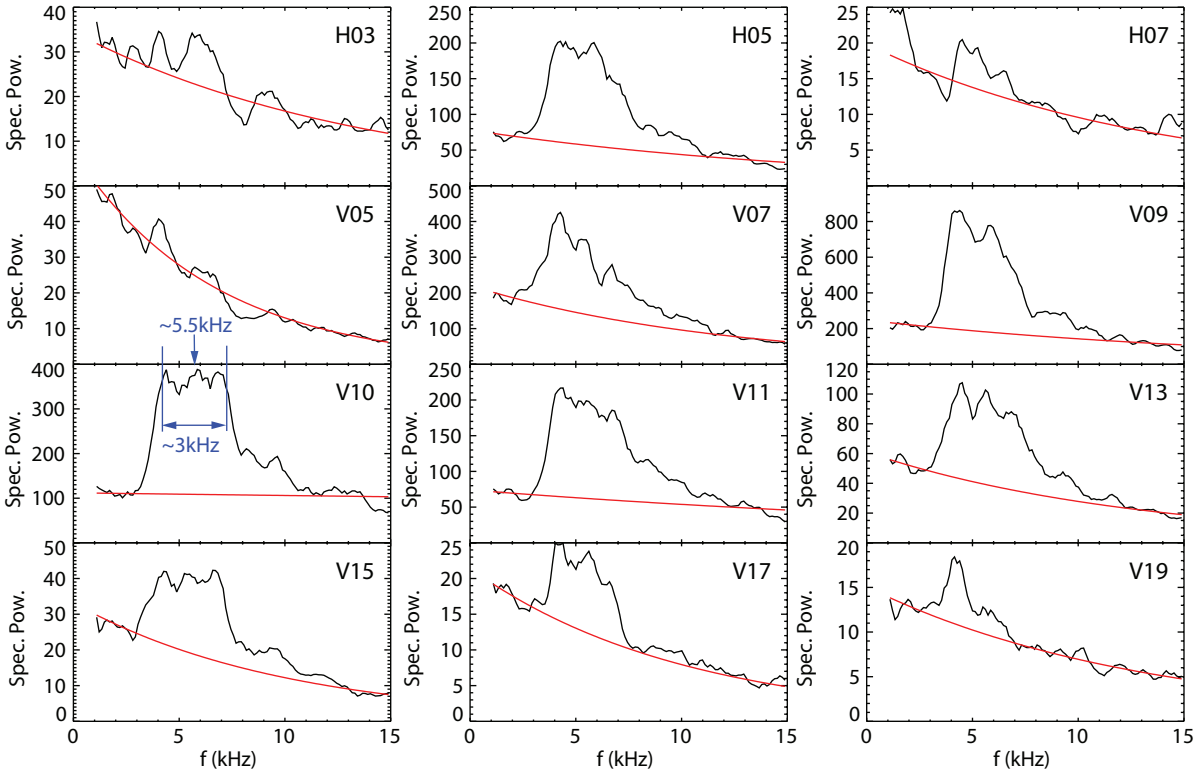

Figure 5.7: Spectral power versus frequency for various AXUV diodes (black) and fit of an exponential function on the background (red) of discharge #27100. The positions of the diodes are shown in Figure 5.8.

Figure 5.7 shows the power versus the frequency, averaged over the time interval from 2.4 s to 2.6 s, for various diodes. The width and the mean frequency are indicated for a specific diode. With all AXUV channels the position of these fluctuations can be located. The strength of the fluctuations is derived by integrating over the spectrum after subtracting the background level, which can be approximated with an exponential function. The fit of an exponential function on the spectrum is also shown in Figure 5.7. The resulting fluctuation strength for all diodes is shown in Figure 5.8, where the colour-code represents the strength. It can be seen that the radiative fluctuations are located close to the X-point in the inner SOL.

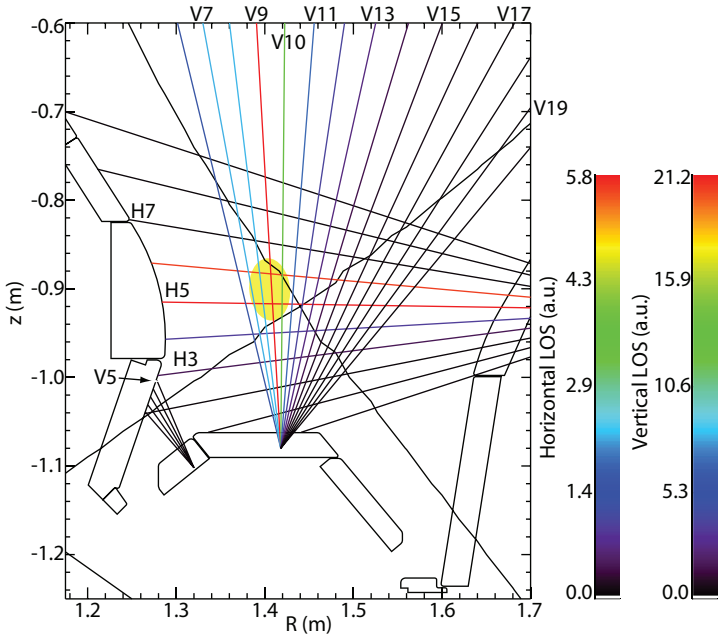

Figure 5.8: Intensity of the fluctuations for all AXUV channels of discharge #27100. The colour-code represents the strength.

Inner divertor At the start of the fluctuating state, there is a sudden increase of Φ_{D^+} (Fig. 5.3a) and Γ_{D^+} as well as an abrupt shift of the peak Γ_{D^+} position away from the strike point from $\Delta S \approx 1\,\text{cm}$ to $\Delta S \approx 5\,\text{cm}$ (Fig. 5.4h). During this state, the ion flux at this position first increases up to $\Gamma_{D^+} \approx 3.2 \cdot 10^{22}\,\text{m}^{-2}\text{s}^{-1}$ and then rolls over at $t \approx 2.6\,\text{s}$. The target electron density at the strike point region shows the same shift and also rolls over, see Figure 5.4d. In contrast, the electron temperature at the target steadily increases up to $T_{e,t} \approx 36\,\text{eV}$ (Fig. 5.4f). The ion flux in the far SOL at $\Delta S > 14\,\text{cm}$ increases throughout this state, whereas $n_{e,t}$ in this region, which is higher than at the strike point, rolls over during this state. The temperature in this region remains low, $T_{e,t} \approx 4\,\text{eV}$.

At the transition to the fluctuating state the peak density in the volume, $n_{e,V}$, shifts from $\Delta S \approx 10\,\text{cm}$ to $\Delta S \approx 6\,\text{cm}$ (Fig.5.4b). Associated with the second roll over of Γ_{D^+}

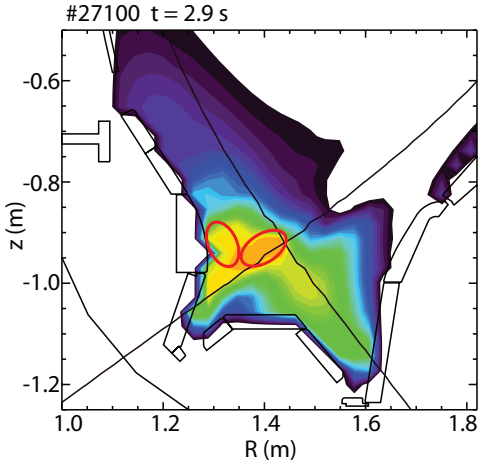

Figure 5.9: Total radiation distribution from foil bolometry in the divertor at one time point during the fluctuating detachment state for #27100. The estimated positions of the high density fronts in the inner divertor are marked with the red circles.

and $n_{e,t}$ at the strike point region (Fig. 5.4h,d) a region of high density with a value of $\approx 2.5 \cdot 10^{20}\,\mathrm{m}^{-3}$ develops in the inner far SOL ($\Delta S \approx 15\,\mathrm{cm}$, Fig. 5.4b). This density is an order of magnitude higher than $n_{e,t}$ and $\bar{n}_e$. In the following these regions are called *high density fronts*. The position can be verified with the vertical $n_{e,V}$ measurements (Fig. 5.4a, $\Delta R = -14\,\mathrm{cm}$) which are from the leftmost LOS (Fig. 5.2a) close to the target. In addition, a second high density front starts to develop in the inner SOL close to the X-point (Fig. 5.4a, $\Delta R = -2\,\mathrm{cm}$). As the region where the SBD diagnostic measures the density corresponds to regions where the radiation is highest, the total radiation distribution can be used as an approximation of the density distribution. The radiation distribution for $t = 2.9\,\mathrm{s}$ is shown in Figure 5.9 and the approximated positions of the high density fronts are indicated. It is also possible, according to the radiation measurement, that this is just one density front rather than two. In any case, however, the density front in the inner divertor expands into the inner far SOL at $\Delta S \approx 15\,\mathrm{cm}$, consistent with the increase of the ion flux and target electron density in this region. With increasing upstream density, first the spatial extent of this front grows into the inner SOL and $n_{e,V}$ rises up to $\approx 2.5 \cdot 10^{20}\,\mathrm{m}^{-3}$ and then rolls over.

Outer divertor During the fluctuating state the ion flux and the electron density at the outer target first increase and then roll over as in the inner one (Fig. 5.4e,i). The peak positions of Γ_{D^+} and $n_{e,t}$ remain constant during the discharge. Moreover, $\Phi_{D^+}^{meas}$ starts to surpass the TPM scaling, $\Phi_{D^+}^{meas} > \Phi_{D^+}^{calc}$, which in the following will be called *flux enhancement*. Consequently the DOD drops below 1, see Figure 5.3d. Contrary to the inner target, $T_{e,t}$ also increases while Γ_{D^+} and $n_{e,t}$ increase and then rolls over (Fig. 5.4g).

In line with this, the density in the outer divertor volume close to the strike point rises by more than an order of magnitude up to $n_{e,V} \approx 4 \cdot 10^{20}\,\mathrm{m}^{-3}$ (Fig. 5.4c), reaching its maximum after Γ_{D^+} and $n_{e,t}$ rolled over. As the spatial extent of the Stark diagnostic in the outer divertor is limited to $\Delta S < 15\,\mathrm{cm}$ it can not be verified if there exists a high density front in the far outer SOL or X-point region similar to the one in the inner divertor.

The complete detachment state

The beginning of this state is defined when the X-point fluctuations disappear (Fig. 5.3f). With the transition from the fluctuating state to the complete detachment state, the core plasma fuelling becomes more efficient. This can be seen in the time traces of the line integrated plasma density and the applied fuelling gas puff (Fig. 5.1, $t \approx 3\,\mathrm{s}$). The plasma density increases faster at this point while the fuelling rate remains constant. In the following, the evolution of the divertor plasma parameters are described in detail and the occurrence of volume recombination will be discussed.

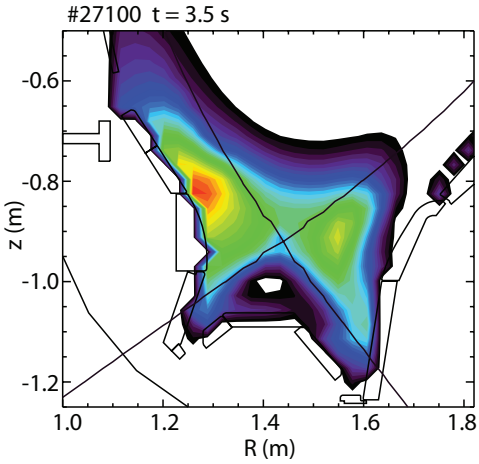

Figure 5.10: Total radiation distribution from foil bolometry in the divertor at one time point during the complete detachment state for #27100.

Inner divertor With the start of the this state $n_{e,t}$, $T_{e,t}$ and Γ_{D^+} at the strike point region almost vanish (Fig. 5.4d,f,h). Thus the plasma is completely detached from the target in this region. In contrast, there is a short increase of $T_{e,t}$ in the private flux region just after the beginning of this state ($t \approx 3\,\mathrm{s}$, Fig. 5.4f). However, the uncertainty in the determination of the strike point position is $\approx 1\,\mathrm{cm}$ and it is therefore possible that this short increase of $T_{e,t}$ occurs in the SOL. In any case, it occurs close to the strike point. Also the high density front at the strike point region disappears and moves along the field lines towards and even above the X-point. With the horizontal and vertical $n_{e,V}$

measurements, the motion of the high density front can be monitored. At the beginning the density front is located at $\Delta S = 15\,\mathrm{cm}$ (Fig. 5.4b) and close to the target at $\Delta R = -14\,\mathrm{cm}$ (Fig. 5.4a). Then the front moves in horizontal as well as in vertical direction until it is close to the X-point at $\Delta R = -2\,\mathrm{cm}$ and $\Delta S = 38\,\mathrm{cm}$ (which are the uppermost horizontal LOS, Fig. 5.2a, being above the X-point). The final position of the density front, at $t = 3.5\,\mathrm{s}$, is consistent with the radiation distribution (Fig. 5.10), which peaks well above the X-point.

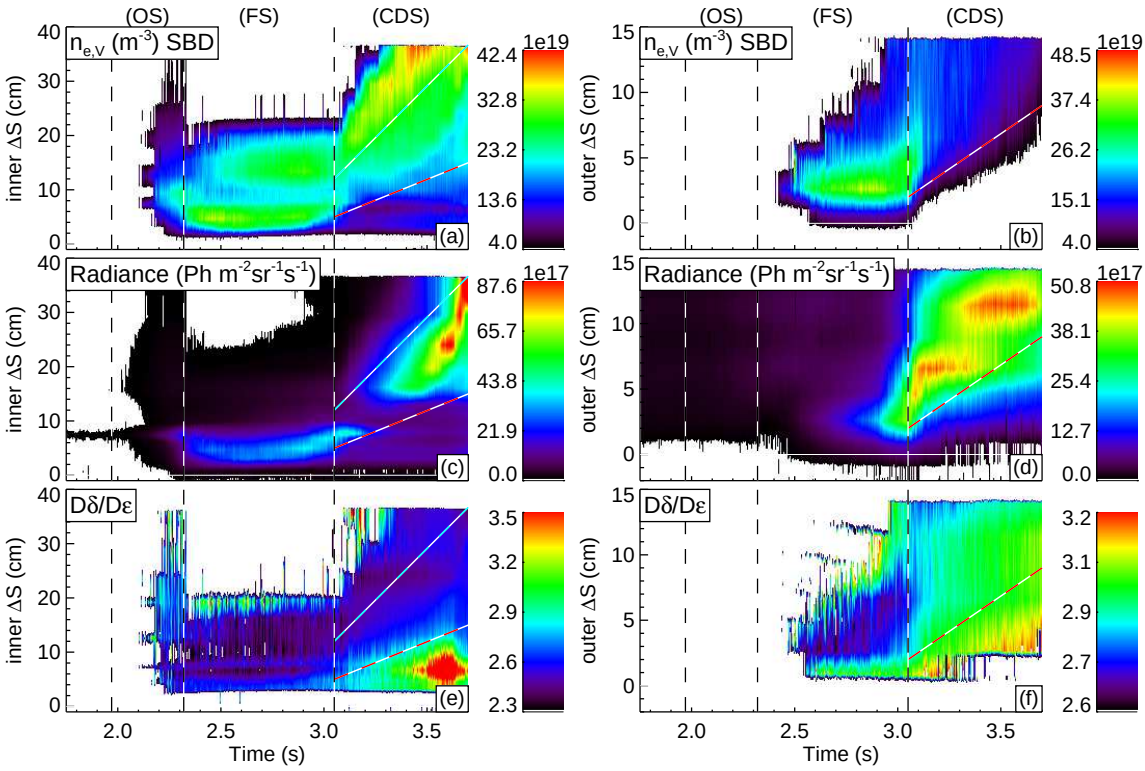

Figure 5.11: Time traces of the line integrated density (a,b), the emissivity of D_δ (c,d) and the line ratio D_δ/D_ϵ (e,f) in the inner and outer divertor volume, respectively of discharge #27100. See text for explanation.

Outer divertor At the transition from the fluctuating state to the complete detachment state, Φ_{D^+} in the outer divertor becomes smaller than the TPM scaling and the DOD exceeds unity (Fig. 5.3b,d). At this point, Γ_{D^+} at the outer target is already strongly reduced by two orders of magnitude with respect to its maximum value (Fig. 5.4i). Also the density and the temperature at the target close to the strike point region ($\Delta S < 5\,\mathrm{cm}$) have reached low values of $n_{e,t} \leq 2 \cdot 10^{19}\,\mathrm{m}^{-3}$ and $T_{e,t} \leq 5\,\mathrm{eV}$. Moreover, the high density front in the outer strike point region rapidly moves out of the spectroscopic observation area ($\Delta S < 15\,\mathrm{cm}$) at the beginning of this state (Fig. 5.4c). In the observed region the plasma is completely detached from the outer target, confirmed by the measurement of the total radiation (Fig. 5.10), which peaks close to the X-point.

It is remarkable that the complete detachment happens simultaneously at the inner and outer strike point region. This has not yet been observed elsewhere.

Evidence for volume recombination and low divertor temperatures The density in the divertor volume, the emissivity of D_δ and the line ratio D_δ/D_ϵ is shown in Figure 5.11. First it can be seen that the D_δ emission increases when the density has decreased, in the inner as well as in the outer divertor. In other words, when the density front has moved towards the X-point (above the blue dotted line in Fig. 5.11a,c), the line emission increases between the density front and the target (below the blue dotted line). The total line emission coefficient, shown in Figure 3.4, increases with decreasing temperature and reaches its maximum at $T_e \approx 1.5\,\mathrm{eV}$. This peak corresponds to the transition from an ionization to a recombination dominated plasma (sec. 3.2) and the temperature is approximately $\approx 1.5\,\mathrm{eV}$ when the D_δ emission peaks. Thereafter, when the emission decreases, the line ratio of D_δ/D_ϵ starts to increase (below the red dotted line in Fig. 5.11c,d,e,f). From Figure 3.5 it can be seen that the line ratio increases when recombination becomes dominant and the temperature is below 1 eV. This is consistent with the drop of the total line emission coefficient below $T_e = 1\,\mathrm{eV}$ (Fig. 3.4). As these are line integrated measurements, absolute values of D_δ/D_ϵ can not be used. However, it can be assumed that the radiation of D_δ and D_ϵ is emitted from the same region and a correct qualitative trend of D_δ/D_ϵ can be expected. It can be concluded from this that, in the inner and outer divertor volume, recombination dominates and the electron temperature is $T_e < 1\,\mathrm{eV}$ in the regions below the red dotted lines in Figure 5.11.

5.2.2 Detachment in hydrogen

To disentangle isotope effects, several discharges of the density ramp series were performed with hydrogen as main ion species (see Table 5.1). The divertor plasma undergoes the same three detachment states in hydrogen as in deuterium. The characteristics of the different detachment states described above qualitatively hold also for a hydrogen plasma with the following main quantitative differences. The ratio of the total ion flux to the inner and outer divertor before the beginning of the fuelling ramp ($t < 1.9\,\mathrm{s}$) is $\Phi^{in}_{D^+}/\Phi^{out}_{D^+} = 1.6$ (Fig. 5.12a,c), which is more symmetric compared to the deuterium fuelled case ($\Phi^{in}_{D^+}/\Phi^{out}_{D^+} = 1.9$). The finally achieved DOD is ≈ 40 and ≈ 5 for the inner and outer divertor, respectively (Fig. 5.12b,d). This is much lower compared to the deuterium fuelled case (inner DOD ≈ 600, outer DOD ≈ 12).

In addition, the radiative X-point fluctuations during the fluctuating detachment state have a frequency of $f \approx 8\,\mathrm{kHz}$ in the hydrogen discharges. This frequency is roughly the frequency in deuterium times the square root of the mass ratio of both species, see Figure 5.12d:

$$8\,\mathrm{kHz} \approx \sqrt{\frac{m_D}{m_H}} \cdot 5.5\,\mathrm{kHz} = 1.4 \cdot 5.5\,\mathrm{kHz} = 7.7\,\mathrm{kHz} \tag{5.3}$$

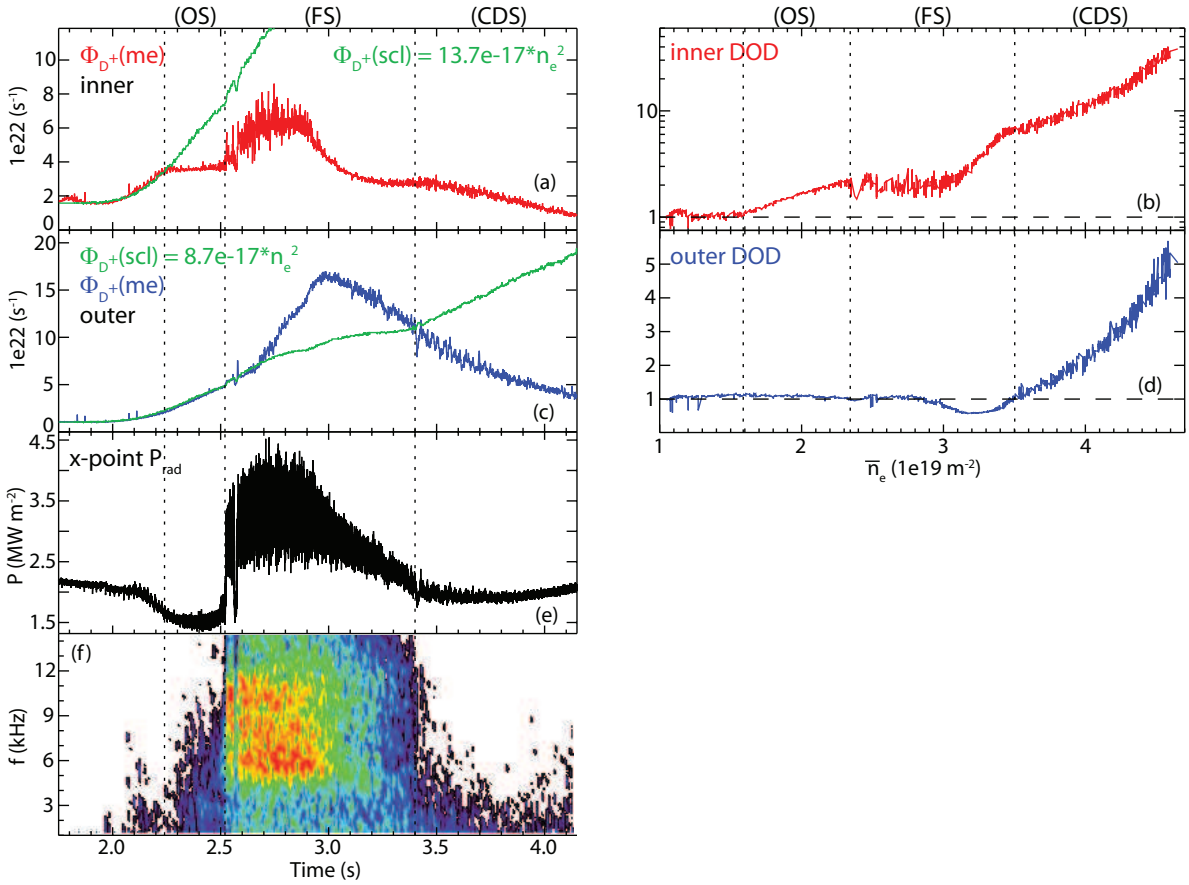

Figure 5.12: Left: Calculated and measured total ion flux to the inner (a) and outer target (c), line integrated radiated power (e) measured by an AXUV diode (orange chord in Figure 5.2b) and its power spectrum (f). Right: DOD as a function of the line integrated peripheral plasma density for the inner (b) and outer (d) divertor of discharge #27362. Note the logarithmic scale of (b). The three detachment states are marked.

5.2.3 The three detachment states in reversed field

In this section the evolution of the divertor plasma is described when B_t and I_p are reversed and compared to the forward field case. Representative for all discharges of the series which are made in reversed field measurements of the discharge #27284 (Tb. 5.1) are shown. When these discharges were carried out, the foil bolometry was not available. Therefore, no measurements of the radiation distribution in the divertor can be shown here. As in forward field, there are three different states during the evolution of detachment. The qualitative development of the target parameters $n_{e,t}$, $T_{e,t}$ and Γ_{D^+} in the inner, respectively outer target in reversed field is rather comparable to the outer,

respectively the inner target in forward field. Whereas the density in the divertor volume evolves quite similar in both field directions.

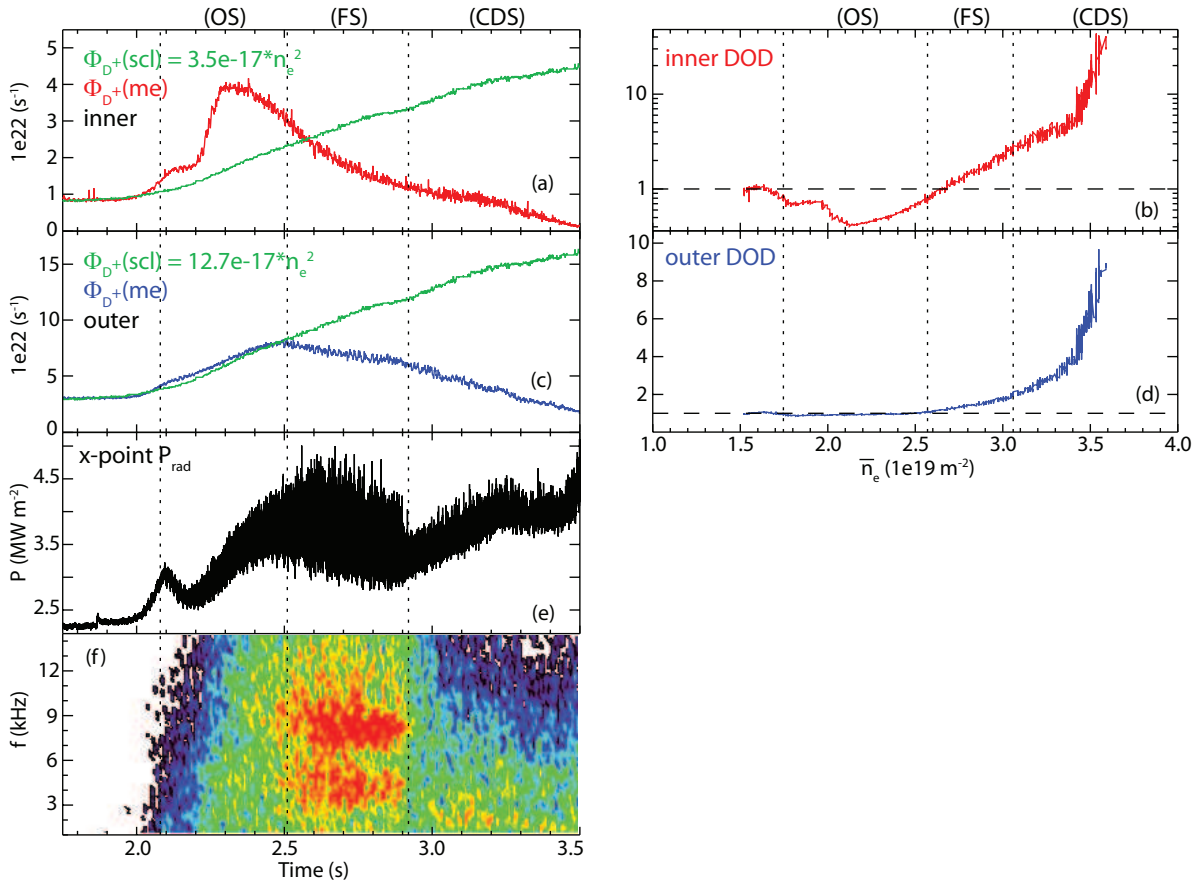

Figure 5.13: Left: Calculated and measured total ion flux to the inner (a) and outer target (c), line integrated radiated power (e) measured by an AXUV diode (orange chord in Figure 5.2b) and its power spectrum (f). Right: DOD as a function of the line integrated peripheral plasma density for the inner (b) and outer (d) divertor of discharge #27284. Note the logarithmic scale of (b). The three detachment states are marked.

The measured and calculated temporal evolutions of Φ_{D^+} and the corresponding DOD as a function of the line integrated peripheral plasma density of the inner and outer divertor are shown in Figure 5.13. The onsets of detachment (roll over of Φ_{D^+}) of the inner and outer divertors are therefore at $t \approx 2.4\,\mathrm{s}$ ($\bar{n}_e \approx 2.1 \cdot 10^{19}\,\mathrm{m}^{-2}$) and $t \approx 2.5\,\mathrm{s}$ ($\bar{n}_e \approx 2.5 \cdot 10^{19}\,\mathrm{m}^{-2}$), respectively. Before the start of the fuelling ramp, $t < 1.9\,\mathrm{s}$, the total ion flux to the outer target is larger than to the inner target, $\Phi^{out}_{D^+}/\Phi^{in}_{D^+} = 3.6$ (Fig. 5.13a,c). This ratio is less symmetric compared to the forward field case and, contrary to forward field, in favour of the outer divertor.

Figure 5.14 shows the inner and outer target profiles of $n_{e,t}$, $T_{e,t}$ and Γ_{D^+} as well as the density measurements in the inner and outer divertor volume. Before the start of the fuelling ramp, peak ion fluxes of $\Gamma_{D^+} \approx 8 \cdot 10^{21}\,\mathrm{m}^{-2}\mathrm{s}^{-1}$ and $\Gamma_{D^+} \approx 5.2 \cdot 10^{22}\,\mathrm{m}^{-2}\mathrm{s}^{-1}$ close

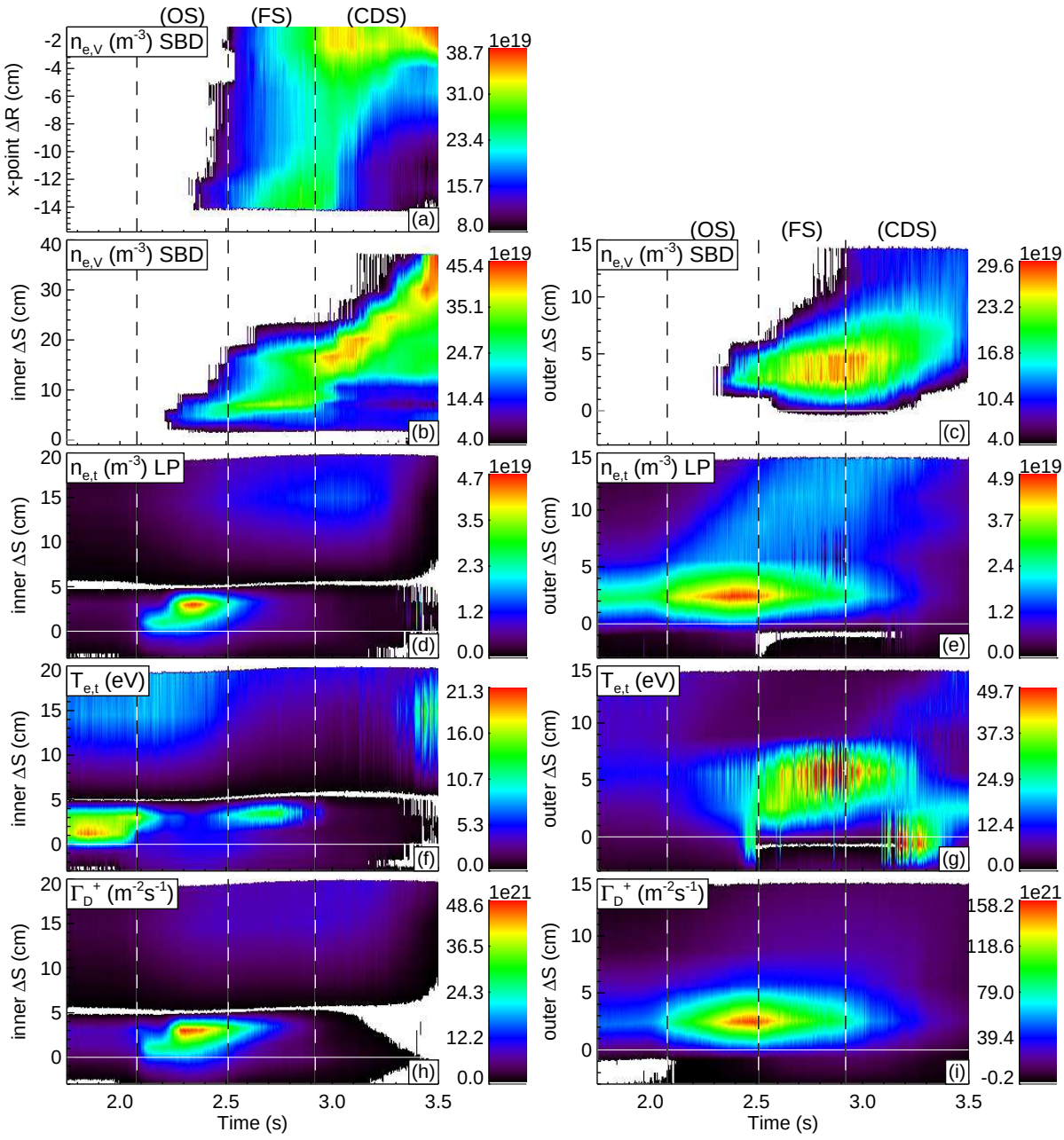

Figure 5.14: Horizontal (a) and vertical (b,c) line integrated $n_{e,V}$ profile in the divertor volume and $n_{e,t}$ (d,e), $T_{e,t}$ (f,g) and Γ_{D^+} (h,i) target profiles in the inner and outer divertor, respectively, of discharge #27284. The three detachment states are marked.

to the inner and outer strike point are measured, respectively.

The onset of detachment state

As in forward field, the start of the onset state is defined by the first deviation from the TPM scaling. This happens, similar to forward field, in the inner divertor. Contrary to forward field, the X-point fluctuations appear already in this state. Their amplitude grows during this state until, at the end of this state, its maximum is reached.

Inner divertor Contrary to forward field, the measured total ion flux increases more strongly compared to the TPM scaling (Fig. 5.13a). Thus, the flux enhancement occurs now in the inner divertor and the DOD falls below unity (Fig. 5.13b). During this state Γ_{D^+} and $n_{e,t}$ increase up to $\Gamma_{D^+} \approx 5 \cdot 10^{22}\,\mathrm{m^{-2}s^{-1}}$ and $n_{e,t} \approx 6 \cdot 10^{19}\,\mathrm{m^{-3}}$, respectively, and then roll over. The target temperature first decreases with increasing $n_{e,t}$ and Γ_{D^+} and increases when $n_{e,t}$ and Γ_{D^+} roll over (Fig. 5.14d,f,h). Associated with the roll over, a high density front of $n_{e,V} \approx 2 \cdot 10^{20}\,\mathrm{m^{-3}}$ develops in the SOL at $\Delta S \approx 7\,\mathrm{cm}$, see Figure 5.14b. It should be noted that, while Γ_{D^+} increases between $t = 2.1\,\mathrm{s}$ and $t = 2.3\,\mathrm{s}$, there seems to be a shift of Γ_{D^+} back to $\Delta S \approx 4\,\mathrm{cm}$ at $t = 2.2\,\mathrm{s}$ (Fig. 5.14h). But it is more likely that the peak of the ion flux profile moves between to probe positions in this case.

Outer divertor The measured Φ_{D^+} follows the TPM scaling throughout this state and the DOD is 1, see Figure 5.13b,d. The peak position of Γ_{D^+} and $n_{e,t}$ remains constant during the discharge (Fig. 5.14e,i). Γ_{D^+} rises up to $\approx 1.6 \cdot 10^{23}\,\mathrm{m^{-2}s^{-1}}$ and $n_{e,t}$ up to $\approx 5 \cdot 10^{19}\,\mathrm{m^{-3}}$. Similar to the inner divertor in forward field, the electron temperature at the target increases with increasing Γ_{D^+} and $n_{e,t}$ throughout this state (Fig. 5.14g). The density in the volume close to the strike point increases up to $\approx 1.5 \cdot 10^{20}\,\mathrm{m^{-3}}$, see Figure 5.14c.

The fluctuating detachment state

In reversed field, the start of this state is defined when the strength of the X-point fluctuations reaches its maximum, see Figure 5.13f.

The X-point fluctuations Contrary to forward field, two frequency bands, one at $f \approx 4.5\,\mathrm{kHz}$ and one at $f \approx 9\,\mathrm{kHz}$ are observed (Fig. 5.13f). The width of each of these frequency bands is $\Delta f \approx 3\,\mathrm{kHz}$, which is similar to forward field.

The maximum of the fluctuations is still located in the inner SOL close to the X-point, see figure 5.15. Their spatial extent, however, is larger than in forward field and seems to expand into the outer divertor SOL.

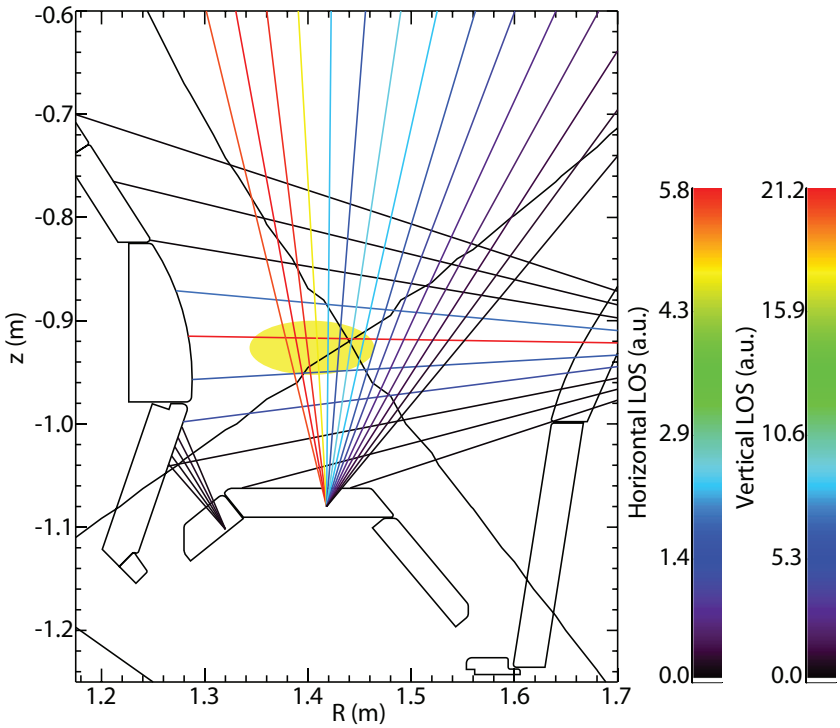

Figure 5.15: Intensity of the fluctuations for all AXUV channels of discharge #27284. The colour-code represents the strength.

Inner divertor During this state, the ion flux and the target density steadily drop further to $\Gamma_{D^+} \approx 5 \cdot 10^{21}\,\mathrm{m^{-2}s^{-1}}$ and $n_{e,t} \approx 7 \cdot 10^{18}\,\mathrm{m^{-3}}$, respectively (Fig. 5.14d,h). Furthermore, the profile of $n_{e,t}$ is getting broader. The target temperature first increases further up to $T_{e,t} \approx 13\,\mathrm{eV}$ and then rolls over within this state (Fig. 5.14f). Associated with the further decrease of Γ_{D^+} and $n_{e,t}$, the high density front at the strike point region ($\Delta S < 10\,\mathrm{cm}$) rises up to $n_{e,V} \approx 3.7 \cdot 10^{20}\,\mathrm{m^{-3}}$ and then rolls over when $T_{e,t}$ rolls over (Fig. 5.14b). Linked to the fluctuations high density fronts of $n_e \approx 3 \cdot 10^{20}\,\mathrm{m^{-3}}$ (Fig 5.14a,b) develop in the inner far SOL ($\Delta S \approx 15\,\mathrm{cm}$) and X-point region ($\Delta R \approx -2\,\mathrm{cm}$). This is similar to forward field. Contrary to forward field, the X-point high density front reaches its maximum at the end of the fluctuating state.

Outer divertor Φ_{D^+}, Γ_{D^+} and $n_{e,t}$ roll over at the start of this state (Figs. 5.13b, 5.14e,i) and the DOD exceeds unity (Fig. 5.13d). The target temperature steadily increases throughout this state up to $T_{e,t} \approx 50\,\mathrm{eV}$ (Fig. 5.14g). Furthermore $T_{e,t}$ strongly fluctuates, which is most likely linked to the radiative X-point fluctuations. As the time resolution of the Langmuir probes is too slow, a correlation analysis with the AXUV diodes can not, however, be made. Associated with the further decrease of Γ_{D^+} and $n_{e,t}$, the high density front at the strike point region increases up to $n_e \approx 3 \cdot 10^{20}\,\mathrm{m^{-3}}$ during this state (Fig. 5.14c).

The complete detachment state

The beginning of the complete detachment state is defined, similar to forward field, when the radiative X-point fluctuations vanish.

Inner divertor At the start of this state, the target parameters at the strike point region ($\Delta S < 10\,\mathrm{cm}$) have already reached very low values of $\Gamma_{D^+} < 2 \cdot 10^{21}\,\mathrm{m^{-2}s^{-1}}$, $n_{e,t} < 3 \cdot 10^{18}\,\mathrm{m^{-3}}$ and $T_{e,t} < 2\,\mathrm{eV}$ (Fig. 5.14d,f,h). Also the high density front in this region has vanished (Fig. 5.14b), indicating that the plasma is completely detached from the inner strike point region. Moreover, similar to forward field, the high density front from the inner strike point region moves upwards along the field lines well above the X-point (Fig. 5.14a,b).

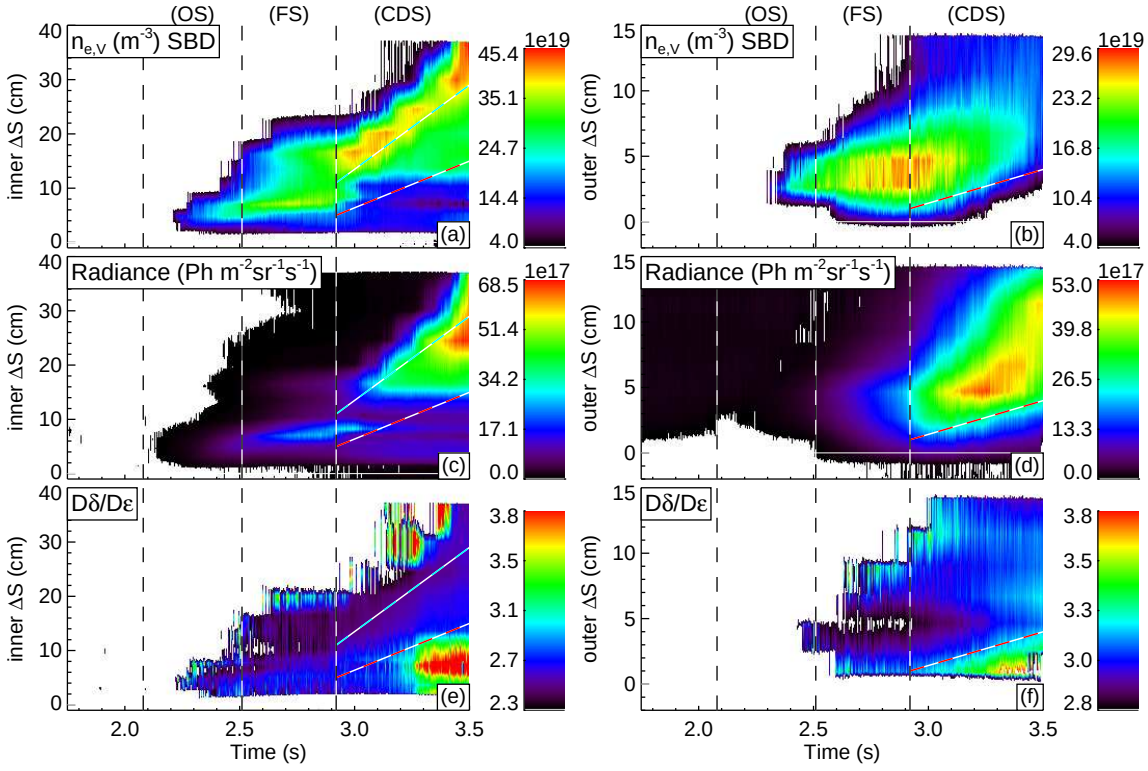

Figure 5.16: Time traces of the line integrated density (a,b), the emissivity of D_δ (c,d) and the line ratio D_δ/D_ϵ (e,f) in the inner and outer divertor volume, respectively of discharge #27284.

Outer divertor The ion flux and the density at the target drop further during this state (Fig. 5.14e,i). Similar to the inner divertor in forward field, the electron temperature at the strike point region ($\Delta S \approx 5\,\mathrm{cm}$) starts to decrease (here to $T_{e,t} \approx 6\,\mathrm{eV}$ at the end of the discharge) while there is a short strong increase of $T_{e,t}$ in the private flux region (Fig. 5.14g). The high density front in the strike point region ($\Delta S < 10\,\mathrm{cm}$, Fig.

5.14c) is reduced by $\approx 50\%$ to $n_e \approx 1.5 \cdot 10^{20}\,\mathrm{m}^{-3}$ during this state. The position of the peak $n_{e,V}$ moves slightly upstream, but, contrary to forward field, stays in the strike point region until the end of the discharge.

Evidence for volume recombination and low divertor temperatures Similar to forward field, there is evidence for volume recombination and therefore electron temperatures below $\approx 1\,\mathrm{eV}$ in the inner and outer divertor. Figure 5.16 shows the density in the divertor volume, the emissivity of D_δ and the line ratio D_δ/D_ϵ. It can be seen again that the line emission increases when the high density front has moved away from the target (below the blue dotted line in Fig. 5.16a,c), indicating temperatures of $\approx 1.5\,\mathrm{eV}$ when the emission reaches its maximum. When the line emission decreases, the D_δ/D_ϵ line ratio increases, and electron temperatures below $\approx 1\,\mathrm{eV}$ can be expected in the regions below the red dotted lines in Figure 5.16.

5.3 Additional effects

In this section, the effect of additional N_2 seeding and an additional magnetic perturbation field on the detachment process will be presented. Furthermore it will be shown that, under certain conditions, the divertor plasma oscillates between the onset and fluctuating detachment state back and forth.

5.3.1 Effect of impurity seeding during the fluctuating state

It was mentioned in section 2.2.3 that, besides increasing the main plasma density, the temperature can be reduced by injecting additional impurities. In this section it will be shown how N_2 seeding alters the detached divertor plasma conditions. In ASDEX Upgrade, it is possible to puff impurities below the divertor dome into the plasma in a feedback controlled way [81], which then cool the divertor plasma via line radiation. The amount of injected nitrogen is controlled with a shunt measurement of the thermoelectric current into the outer divertor target, yielding an approximation for the divertor temperature, $T_{t,sh}$ [81].

Effect of N_2 seeding during the fluctuating state

Such a feedback controlled N_2 puffing was applied during the fluctuating detachment state in forward field. This discharge #27326 is an identical repeat of the reference discharge #27100 (Table 5.1) with the following exception. When the fluctuating detachment state was established, the fuelling gas puff and hence the plasma density were kept constant. Then the N_2 seeding was applied. In Figure 5.17a time traces of the

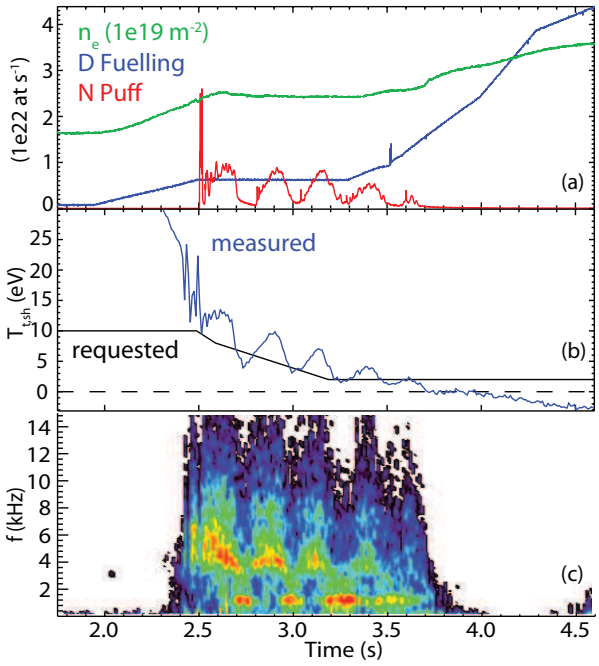

Figure 5.17: Time traces of (a) D fuelling (blue), N_2 puff (red), line integrated core plasma density (green); (b) requested (black) and measured (blue) $T_{t,sh}$; (c) spectrogram of an AXUV diode of discharge #27326.

applied D and N_2 puff as well as the line integrated plasma density are shown. The feedback impurity gas puff starts at 2.5 s and is controlled such that $T_{t,sh}$ is decreased from $\approx$ 12 to $\approx$ 2 eV. As mentioned before, this is just an approximation of the divertor temperature. The requested $T_{t,sh}$ as well as the measured one is shown in Figure 5.17b. Due to the delay of the temperature response on the injected N_2 and the feedback controller itself, N_2 was puffed intermittently. This is why there are oscillations of $T_{t,sh}$ around the requested value.

Figure 5.18 depicts Γ_{D^+} at the target and $n_{e,V}$ in the divertor. With the decrease of the temperature due to the N_2 seeding, Γ_{D^+} on the inner and outer target is reduced by $\approx$ 50% (Fig. 5.18d,e). The frequency of the X-point fluctuations is lowered to $\approx$ 1 kHz (Fig. 5.17c) during phases where the $T_{t,sh}$ oscillations are around the minimal temperature values. The frequency at the maxima starts at $f \approx 5.5$ kHz for $T_{t,sh} = 12$ eV and decreases to $f \approx 3$ kHz for $T_{t,sh} = 4$ eV. Moreover, the densities of the high $n_{e,V}$ fronts in the inner far SOL, inner X-point region and outer strike point region, characteristic for the fluctuating detachment state, are also reduced by $\approx$ 50% (Fig. 5.18a,b,c) during the phases where $T_{t,sh}$ is close to a local minimum.

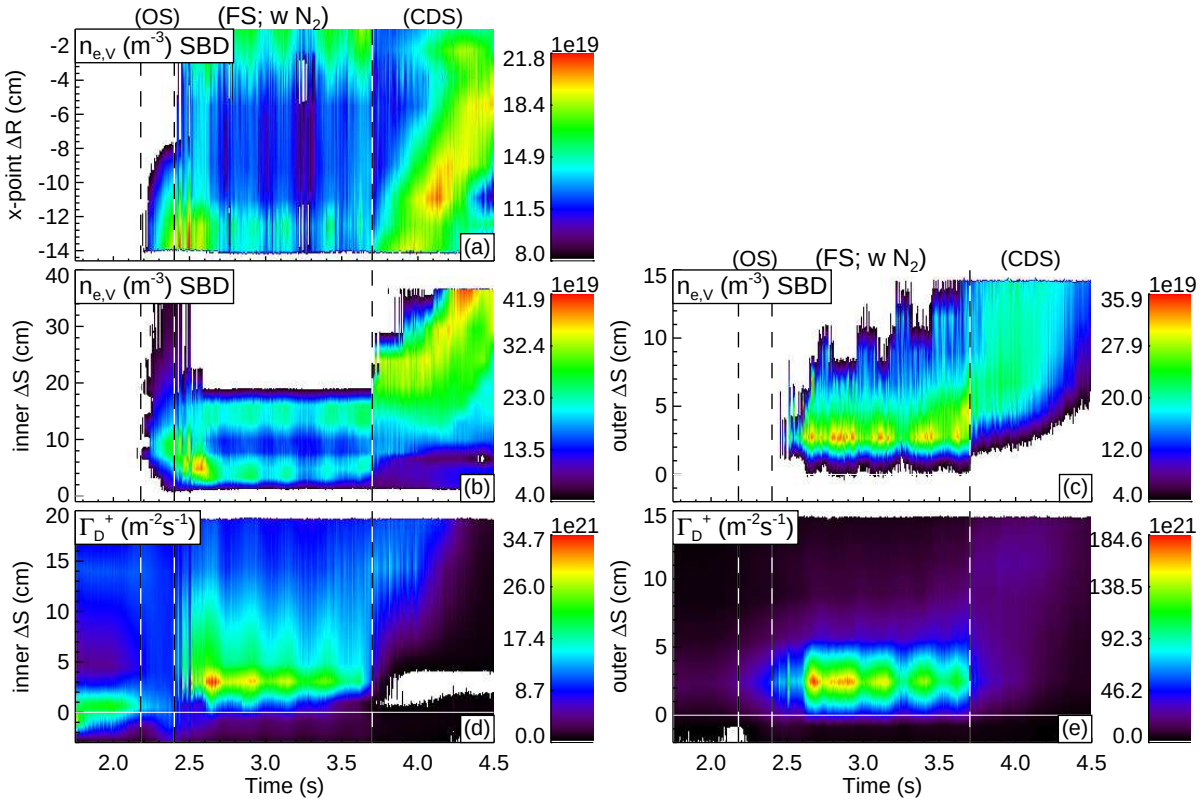

Figure 5.18: Horizontal (a) and vertical (b) line integrated $n_{e,V}$ profile and Γ_{D^+} (d) in the inner divertor. Vertical (c) line integrated $n_{e,V}$ profile and Γ_{D^+} (e) in the outer divertor of #27326. The three detachment states are marked.

High power H-mode discharges with N_2 seeding

A similar effect is observed in high power, high density H-mode discharges. N_2 seeding is routinely used in these high power discharges to reduce the power load to the outer divertor target. Besides this cooling effect, N_2 seeding leads to an improved confinement [82]. The underlying physics of this confinement improvement is not yet completely understood [83].

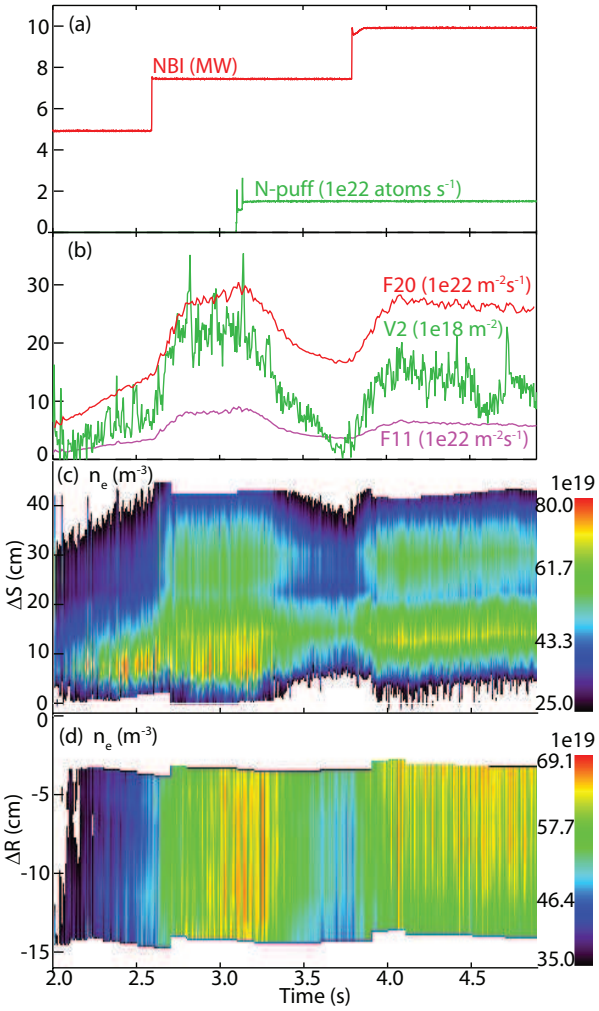

Figure 5.19: Time traces of (a) NBI heating (red), N_2 puff (green); (b) Γ_D (red & magenta), $n_{e,V}$ from V2; horizontal (c) and vertical (d) line integrated $n_{e,V}$ profile in the inner divertor of discharge #26302.

In Figure 5.19 time traces of such a discharge with $I_p = 1\,\mathrm{MA}$, $B_t = -2.5\,\mathrm{T}$ and $\bar{n}_e \approx 8.2 \cdot 10^{19}\,\mathrm{m}^{-2}$ are shown. The NBI heating power was increased stepwise from 5 MW to 10 MW and a constant N_2 puff was applied at $t = 3.5\,\mathrm{s}$. In the phase without N_2 puff a high density front around $5 \cdot 10^{20}\,\mathrm{m}^{-3}$ is measured in the upper part of the inner divertor via the Stark broadening diagnostic (Fig. 5.19c,d). This is supported by a vertical interferometer measurement. The position of the interferometer chord (V2) is shown in

Figure 5.2b. Knowing the density profile of the confined plasma, one can subtract this part from the interferometer measurement, giving the line integrated density in the far SOL [84]. With an intersection length of $\approx 10\,\mathrm{cm}$ of the cord in the SOL, $n_{e,V}$ of the order of $1 \cdot 10^{20}\,\mathrm{m}^{-3}$ are measured (Fig. 5.19b), in line with the Stark measurements. Moreover, high neutral fluxes, Γ_D, are measured with fast ionization gauges at the X-point hight (F20) and above (F11), see Figure 5.19b and Figure 5.2b.

The applied N_2 puff leads to a strong reduction of both $n_{e,V}$ and Γ_D of $\approx 50\%$ in the inner divertor. Also they do not extend far upwards anymore. As the AXUV diodes where not yet available when this discharge was carried out, it is not known whether the radiative X-point fluctuations are also present in this discharge and being suppressed with N_2 seeding. But the characteristics of the high density fronts in the inner SOL are similar to those of the L-mode discharge #27326 discussed in the previous section. Namely the high density fronts in the inner far SOL and X-point region are suppressed with N_2 seeding. When the heating power is further increased by 2.5 MW (Fig. 5.19 at $t = 3.8\,\mathrm{s}$) while the amount of injected N_2 stays constant, the high density and Γ_D fronts in the far SOL are re-established.

5.3.2 Effect of magnetic perturbation coils

When theses experiments were carried out, ASDEX Upgrade was equipped with eight in-vessel saddle coils [85] in order to externally produce magnetic perturbation fields (MP). They are located at the low field side, four coils are mounted above and four coils are mounted below the midplane. The discharge #27101 was repeated with the coils switched on (Table 5.1). The magnetic perturbation field produced by the coils has a toroidal mode number of $n = 2$ and the currents of the upper and lower coils, $I_{coil} = 1\,\mathrm{kA}$, are applied with odd parity.

Figure 5.20 shows Φ_{D^+} and the power spectrum of an AXUV diode of discharge #27101 (without MP) in comparison with discharge #27102 (with MP). Before the onset of detachment, the total ion flux to the inner target is $3.4 \cdot 10^{22}\,\mathrm{s}^{-1}$ with and without MP. With MP Φ_{D^+} in the outer divertor is slightly higher ($\Phi_{D^+} = 1.8 \cdot 10^{22}\,\mathrm{s}^{-1}$) compared to the case without MP ($\Phi_{D^+} = 1.6 \cdot 10^{22}\,\mathrm{s}^{-1}$). The onset of detachment and the transition into the fluctuating state occur with and without MP at the same time. Also the temporal evolution of Φ_{D^+} (Fig. 5.20), Φ_{D^+} and $n_{e,V}$ (Fig. 5.21) in the inner and outer divertor evolve with and without MP similar up to the fluctuating state. The peaks of Φ_{D^+} at the beginning of the fluctuating state without MP (Fig. 5.20a,c) are the divertor plasma oscillations discussed in the next section, which are suppressed by the magnetic perturbation.

The first effect of the applied MP happens when the outer Γ_{D^+} rolls over. With MP the outer Γ_{D^+} then drops abruptly (Fig. 5.20d). This determines the end of the fluctuating

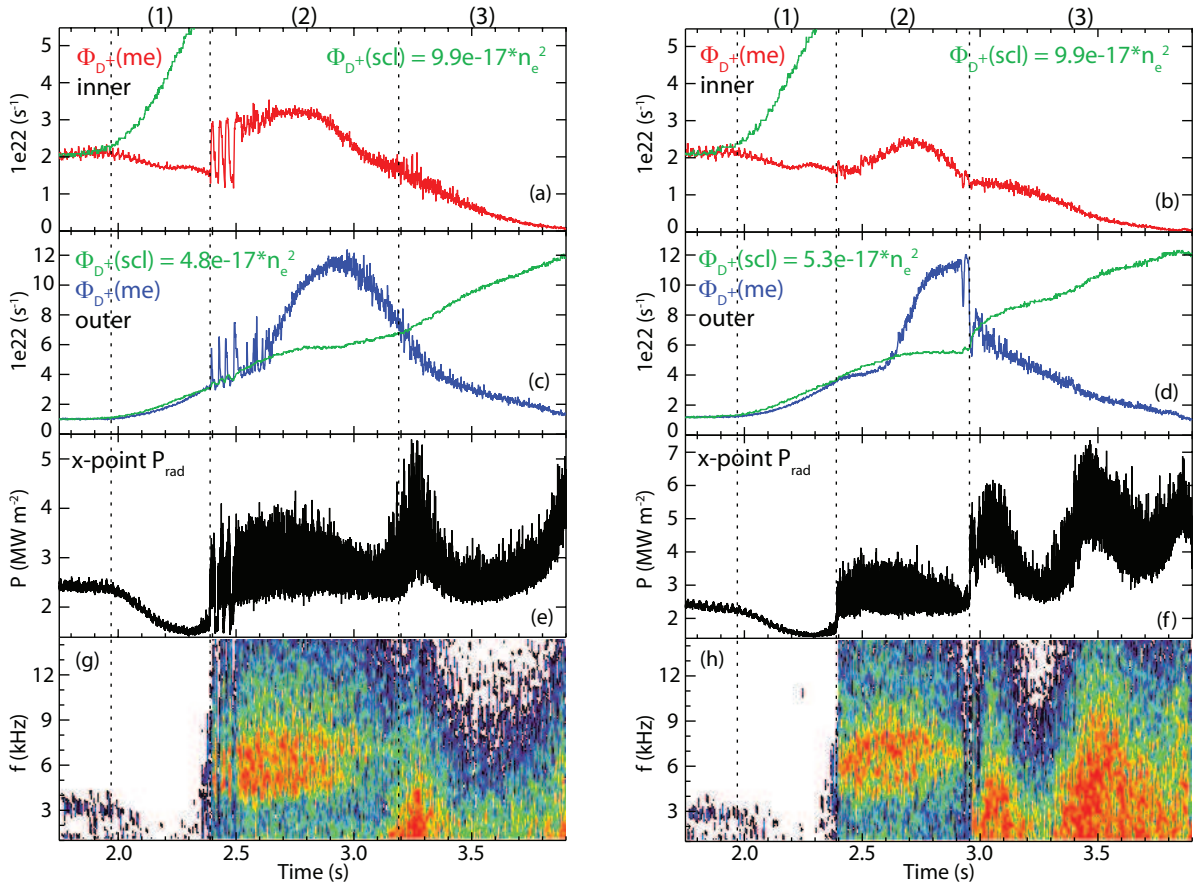

Figure 5.20: Calculated and measured total ion flux to the inner (a,b) and outer target (c,d), line integrated radiated power (e,f) measured by an AXUV diode (orange chord in Figure 5.2b) and its power spectrum (g,h) without (left column, #27101) and with (right column, #27102) MP, respectively. The three detachment states are marked.

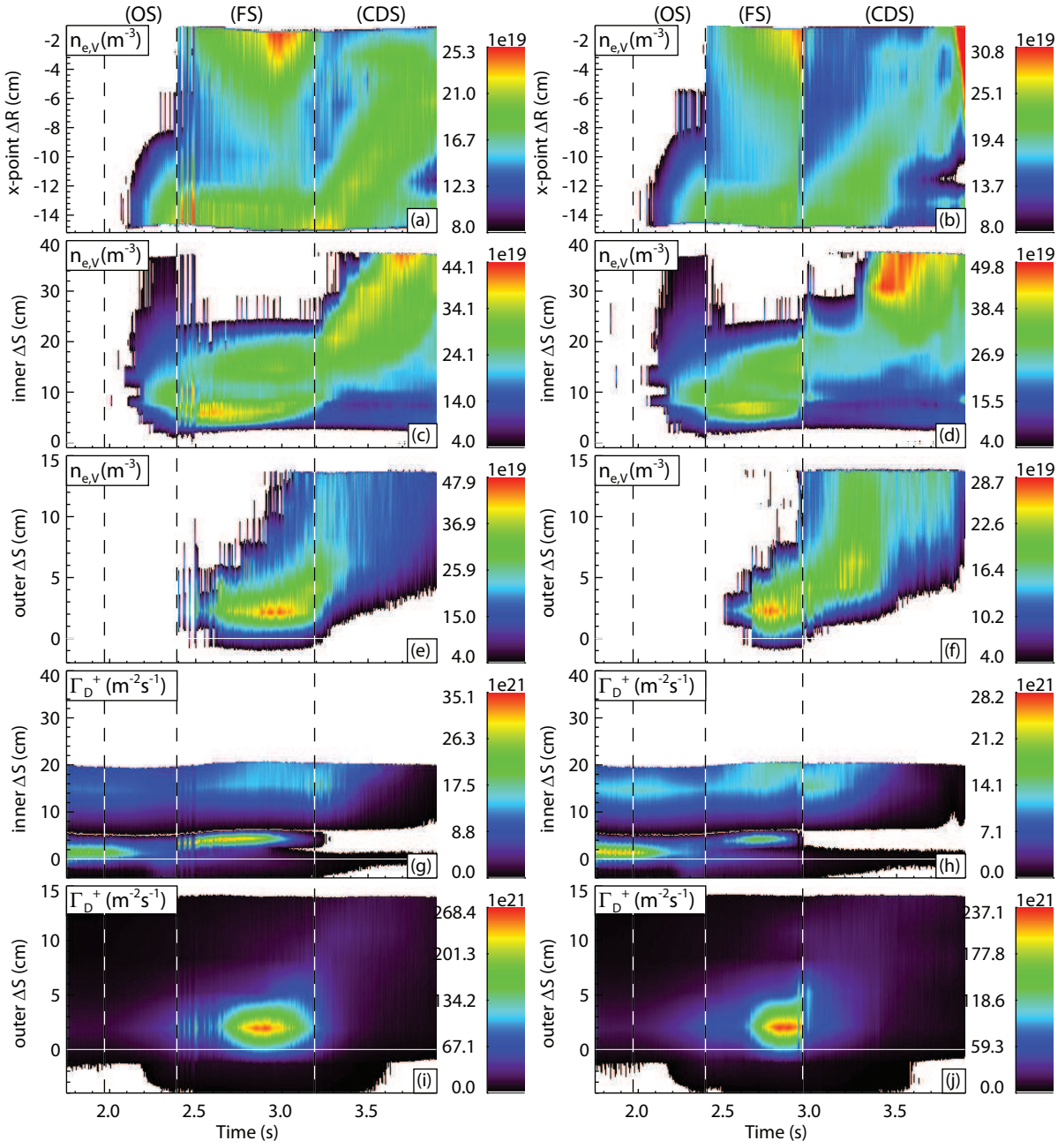

Figure 5.21: Horizontal (a,b) and vertical (c,d) line integrated $n_{e,V}$ profile and Γ_{D^+} (g,h) in the inner divertor. Vertical (e,f) line integrated $n_{e,V}$ profile and Γ_{D^+} (i,j) in the outer divertor without (left column, #27101) and with (right column, #27102) MP, respectively. The three detachment states are marked.

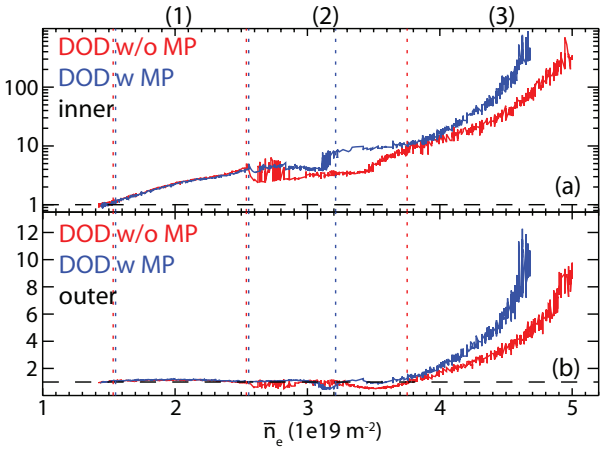

Figure 5.22: DOD as a function of the line integrated peripheral plasma density for the inner (a) and outer (b) divertor without (red, #27101) and with (blue, #27102) MP. Note the logarithmic scale of (a). The three detachment states for both cases are marked.

state (Fig. 5.20h). In the case without MP, the end of the fluctuating state occurs when the measured Γ_{D^+} falls below the TPM scaling (Fig. 5.20d). The complete detachment state with MP can be divided into two parts. At the beginning of the complete detachment state the high density fronts in the inner far SOL and X-point region disappear (Fig. 5.21b,d). The plasma is completely detached from the inner strike point region ($\Gamma_{D^+}(\Delta S < 8\,\mathrm{cm}) < 1 \cdot 10^{21}\,\mathrm{m^{-2}s^{-1}}$, but the peak Γ_{D^+} in the far SOL shifts towards the strike point (Fig. 5.21f). The peak Γ_{D^+} at the outer strike point drops at the beginning of the complete detachment state to $\Gamma_{D^+} \approx 6.9 \cdot 10^{22}\,\mathrm{m^{-2}s^{-1}}$, which is comparable to the case without MP (Fig. 5.21i,j). The high density front in the outer divertor moves upstream ($\Delta S = 2\,\mathrm{cm}$ to $\Delta S = 5\,\mathrm{cm}$) and, contrary to the case without MP, stays in this region (compare Fig. 5.21g,h, $\geq 3.2\,\mathrm{s}$). During the second part of the complete detachment state with MP this outer high density front moves out of the region covered by the Stark diagnostic. The DOD with and without MP is shown in Figure 5.22. It can be seen that the outer divertor detaches slightly earlier with MP. Furthermore, with MP detachment in the inner and outer divertor proceeds faster with respect to the upstream density. Consequently, the density limit occurs earlier with MP, i.e. at $\bar{n}_e^{edge} = 4.6 \cdot 10^{19}\,\mathrm{m^{-2}}$ compared to $\bar{n}_e^{edge} = 5 \cdot 10^{19}\,\mathrm{m^{-2}}$ without MP.

5.3.3 Divertor plasma oscillations

At medium to high main plasma densities and the heating power close to the L-H transition threshold the divertor plasma oscillates back and forth between two different states. This situation was observed for example in discharge #27101 of the density ramp series (Fig. 5.23,5.24). The oscillations start at $t = 2.4\,\mathrm{s}$ and, as the main plasma density is steadily increased, disappear at $t = 2.5\,\mathrm{s}$. When all plasma parameters are kept

constant, these oscillations do not disappear and can be maintained throughout the discharge (#24664, not shown here). In the first state, the D_α radiation is high in the inner divertor and low in the outer divertor, the neutral fluxes are high in the inner divertor and low in the private flux region and the line integrated plasma density is low (Fig. 5.23, left side). In the second state, the conditions are the other way around (D_α radiation in the inner divertor is low and high in the outer divertor, etc). For this particular discharge the frequency of this oscillations is $f \approx 40\,\mathrm{Hz}$. Overall frequencies in the range of $25\,\mathrm{Hz} < f < 60\,\mathrm{Hz}$ for this kind of oscillations were found at ASDEX-Upgrade.

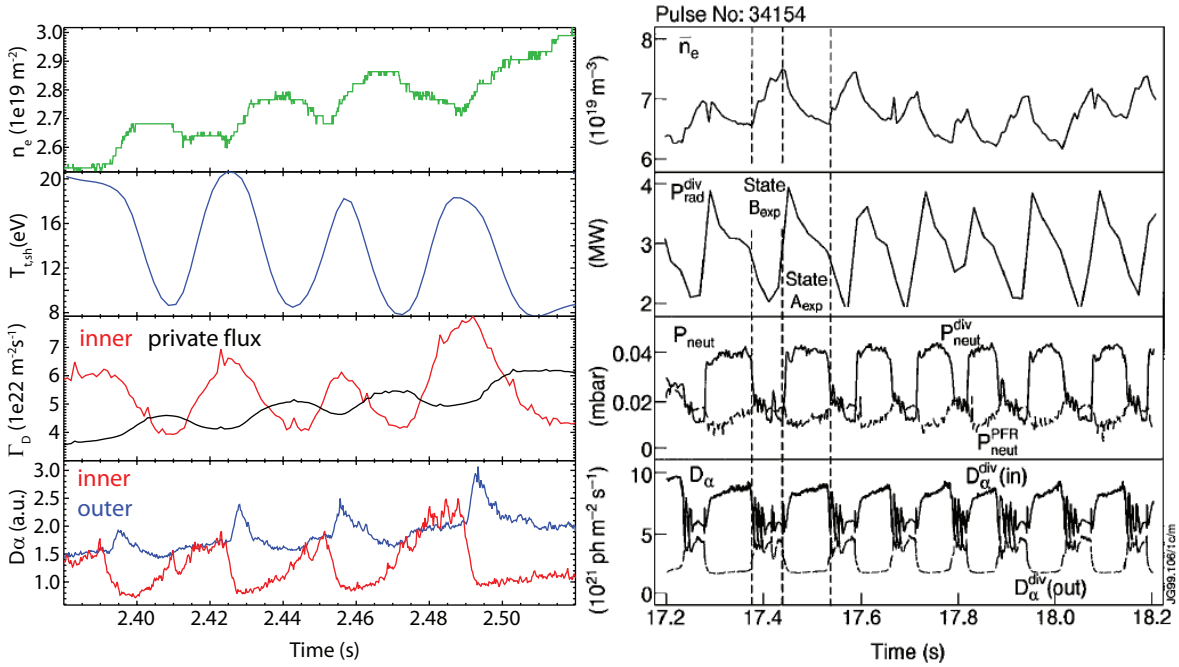

Figure 5.23: Left side from top to bottom: Time traces of line integrated plasma density, $T_{t,sh}$ in the outer divertor, Γ_D in the inner divertor (red) and private flux region (black), D_α emission in the inner (red) and outer (blue) divertor of ASDEX Upgrade discharge #27101. Right side from top to bottom (taken from [86]): Time traces of line averaged plasma density, total radiation in the divertor, neutral pressure in the inner divertor and private flux region, D_α emission in the inner and outer divertor of JET discharge #34154.

Divertor plasma oscillations were previously found at JET with the MkI divertor [86]. The conditions under which these oscillations appear (medium to high densities and heating power close to the L-H threshold) and the characteristics of the two states between which the plasma oscillates (Fig. 5.23, right side taken from [86]) are similar to those reported here.

With the previously given characterization of the three detachment states (section 5.2) the two states between which the plasma oscillates can be identified, namely the onset and the fluctuating state. Before the oscillations ($t < 2.4\,\mathrm{s}$), the divertor plasma is in the onset state. With the first oscillation the plasma is in the fluctuating state. This

means that the, for this state distinctive, high density front appears in the inner far SOL and X-point region (Fig. 5.24b,a) as well as in the outer strike point region (Fig. 5.24c). Consequently Γ_{D^+} also increases in the inner and outer divertor (Fig. 5.24d,e). Then the divertor plasma oscillates between both states. After the oscillations ($t > 2.5\,\mathrm{s}$) the divertor is in the fluctuating detachment state. While the main plasma density is steadily increased, the divertor plasma develops further as described in section 5.2 and enters the complete detachment state.

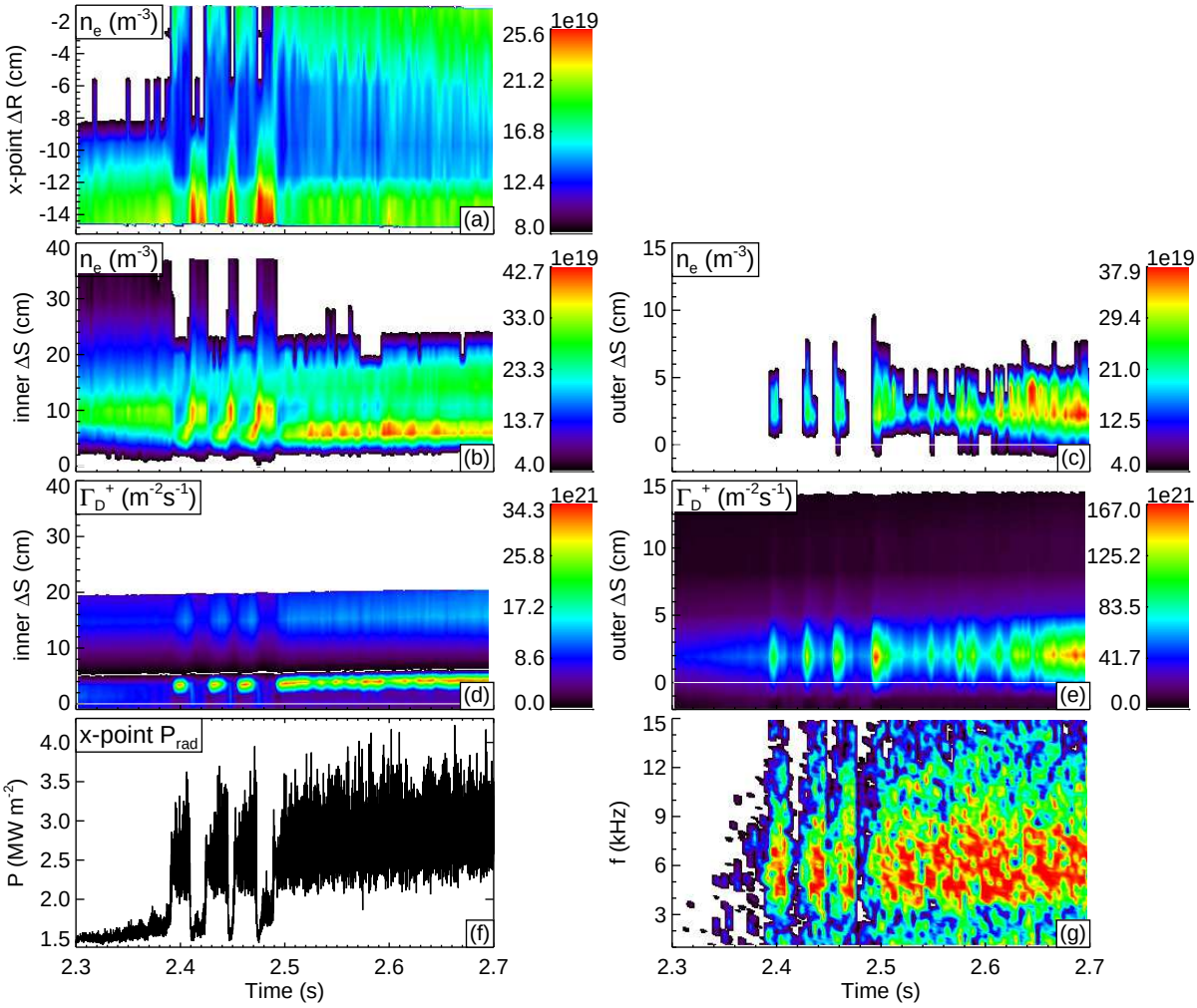

Figure 5.24: Horizontal (a) and vertical (b) line integrated $n_{e,V}$ profile and Γ_{D^+} (d) in the inner divertor. Vertical (c) line integrated $n_{e,V}$ profile and Γ_{D^+} (e) in the outer divertor. Line integrated radiated power (f) measured by an AXUV diode (orange chord in Figure 5.2b) and its power spectrum (g) of #27101.

The oscillations are also apparent in the spectrogram of the AXUV diode signal (Fig. 5.24f,g). If the divertor plasma is in the fluctuating state, the radiative X-point fluctuations appear. When the divertor plasma oscillates back into the onset state, the fluctuations disappear. During the fluctuating state the D_α radiation and the neutral

pressure in the inner divertor is low (Fig. 5.23). It is remarkable that in JET during the same state sub-oscillations in the D_α signal with much higher frequency (with respect to the frequency of the plasma oscillations) were observed, as stated in [86].

Chapter 6

Summary and discussion of the experimental results

6.1 Summary

During the evolution of divertor detachment three different distinct states where found wherein the behaviour of the inner and outer divertor is strongly coupled. The characteristics of these detachment states will be summarized with respect to the forward field case, which was the most extensively investigated case.

The start of the first detachment state, the *onset state*, is defined when the first deviation from the Two-Point-Model (TPM) scaling occurs. This happens in the inner divertor with the roll over of the ion flux density, Γ_{D^+}, (DOD$>$ 1) and the target electron density, $n_{e,t}$, close to the strike point. Associated with this roll over, the electron density in the inner divertor volume, $n_{e,V}$, starts to increase. The outer divertor follows the TPM scaling (DOD$=$ 1) throughout this state, i.e. Γ_{D^+} and $n_{e,t}$ increases with increasing upstream density, whereas the target temperature, $T_{e,t}$, decreases (consistent with equations 2.26-2.28).

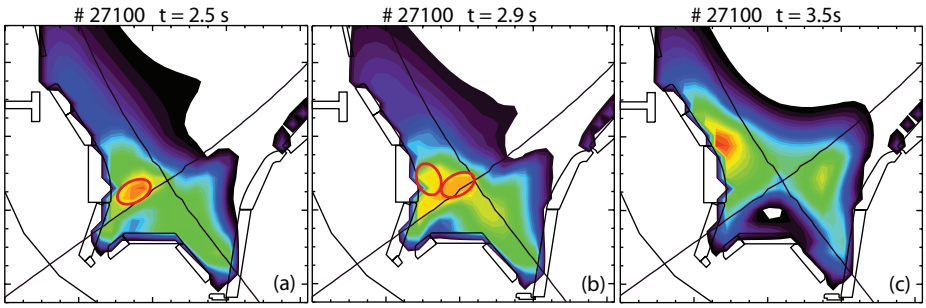

Figure 6.1: Total radiation distribution from foil bolometry in the divertor for three different time points of #27100. See text for explanations.

The appearance of radiative fluctuations characterizes the start of the second, the *fluc-*

tuating detachment state. These fluctuations have a mean frequency of $f \approx 5.5\,\mathrm{kHz}$, a width of $\Delta f \approx 3\,\mathrm{kHz}$ and are situated in the inner SOL close to the X-point. In hydrogen, the mean frequency is increased by the square root of the mass ratio of both species, i.e. $f \approx 8\,\mathrm{kHz}$. At the beginning of this state, the total ion flux, Φ_{D^+}, to the inner divertor and Γ_{D^+} and $n_{e,t}$ close to the inner strike point suddenly increase. In addition, there is a jump of the peak Γ_{D^+} and $n_{e,t}$ position in the strike point region from $\Delta S \approx 1\,\mathrm{cm}$ to $\Delta S \approx 5\,\mathrm{cm}$ at the transition to the fluctuating state. With increasing upstream density, Γ_{D^+} and $n_{e,t}$ at the strike point region ($\Delta S \approx 5\,\mathrm{cm}$) roll over. After the roll over of Γ_{D^+} and $n_{e,t}$ at the strike point region, $T_{e,t}$ in this region increases. This behaviour is consistent, since the momentum loss factor, which accounts for the momentum, and therefore Γ_{D^+} and $n_{e,t}$, removal in equation 2.24, causes an increase of the temperature (eq. 2.26). After the roll over, $n_{e,V}$ increases further. In order to remove momentum via CX-collisions, a high neutral density (gas-target) must exist in front of the target (sec. 2.2.3). At the boundary of this gas-target in the SOL, the plasma parameters still follow the TPM scaling (e.g $n_e \propto \bar{n}_e^3$, eq. 2.27). The density in the divertor volume should therefore continue to increase with increasing upstream density, being in agreement with the measured evolution. The position and spatial extend of this high density front can be approximated by the distribution of the total radiation in the inner divertor (red circle in Fig. 6.1a).

During the fluctuating detachment state, high density fronts develop also in the inner far SOL and X-point region, whose estimated positions are indicated by the red circles in Figure 6.1b. According to the bolometric measurement, it is also possible that this is just one density front rather than two. In any case, however, the density front in the inner divertor expands into the inner far SOL at $\Delta S \approx 15\,\mathrm{cm}$, consistent with the measured increase of the ion flux and target electron density in this region. Therefore, a mechanism must exists, which brings more particles to the far SOL, possibly caused by an increase of the turbulent radial transport (eq. 2.44) in this region.

At the end of the fluctuating state, the fuelling of the main plasma becomes less efficient, i.e. although the fuelling puff is constantly increased, the main plasma density almost saturates. Based on the stability theory of detached plasmas (sec. 2.2.3), the main plasma density cannot be increased further by gas puffing at a certain point. Then, the dense plasma buffer in the SOL must increase and move towards the X-point (sec. 2.2.3). Indeed, a decrease of $n_{e,V}$ at the inner strike point region and an increase of $n_{e,V}$ in the inner far SOL and X-point region is measured during the phase in which the main plasma density increases less strongly than the fuelling puff (compare also Fig.6.1a,b).

The total ion flux to the outer divertor first increases more strongly than the TPM scaling (DOD<1) and then rolls over during the fluctuating detachment state. Consequently, $n_{e,V}$ steadily increases. The effect of DOD<1, namely the flux enhancement, will be discussed below.

The transition to the complete detachment state is defined when the radiative X-point fluctuations vanish. At this transition, the inner and outer divertor simultaneously start to detach completely from the strike point region. The complete detachment is defined here when the target parameters Γ_{D^+}, $n_{e,t}$ and $T_{e,t}$ drop to significant lower values and, the main point, when the high density front in the strike point region decreases (In contrast, the onset of detachment is defined here by the roll over of the total ion flux, Φ_{D^+}). In the outer divertor, the high density front moves out of the area covered by the SBD diagnostic. In the inner divertor, the movement of the high density front during this state from the target towards and even above the X-point can be monitored. This is consistent with the total radiation distribution before the complete detachment state (6.1b) and at the end of this state (6.1c). It was shown by means of spectroscopy, that, once the high density front has moved away from the target, recombination is dominant and temperatures are below $\approx 1\,\mathrm{eV}$ in the region between the high density front and the target. This is expected, as first a high density is necessary in order to remove momentum from the plasma, slowing down the plasma flow to the target. This triggers, in combination with temperatures below $\approx 1\,\mathrm{eV}$, the recombination process. In addition, the total radiated power in the main plasma and SOL almost equals the total applied heating power at the end of the complete detachment state (Fig. 5.1c). This indicates that more than $\approx 90\%$ of the power entering the SOL is radiated before reaching the target.

The main differences between the forward field case and the reversed field case are summarized in the following. In reversed field, the radiative X-point fluctuations consist of two frequency bands of $f \approx 4.5\,\mathrm{kHz}$ and $f \approx 9\,\mathrm{kHz}$, their width of $\Delta f \approx 3\,\mathrm{kHz}$ is similar to the forward field case. The spatial extent of the fluctuations is larger compared to forward field and seems to expand into the outer divertor SOL. In reversed field, their amplitude grows already in the onset state and the maximum amplitude is reached in the fluctuating state.

In forward field, before the onset of detachment, the total ion flux, Φ_{D^+}, to the inner target is larger than to the outer target. In reversed field the total ion flux to the outer target is larger. The first deviation from the TPM scaling is, in forward field, a less steep rise of Φ_{D^+} compared to the scaling (DOD > 1) and in reversed field a stronger increase (DOD < 1, the flux enhancement). The finally achieved DOD is for both field directions larger in the inner than in the outer divertor. The ratio of DOD(in)/DOD(out) becomes more symmetric in reversed field (≈ 50 in forward field, ≈ 1.5 in reversed field).

Furthermore, the effect of N_2 seeding during the fluctuating state in forward field was investigated. With additional N_2 seeding during the fluctuating detachment state, the n_e values of the high density fronts in the inner far SOL, inner X-point region and outer strike point region are reduced by $\approx 50\%$. Φ_{D^+} to the inner and outer target is reduced by $\approx 25\%$. Also the frequency of the radiative X-point fluctuations is reduced

to $f \approx 1\,\mathrm{kHz}$ with N_2 seeding. A similar effect is observed in high power, high density H-Mode discharges. Here, the density reduction of the high density front in the inner far SOL is confirmed with a vertical interferometer measurement. In addition, a reduction of the neutral fluxes by $\approx 50\%$ is measured in the far SOL with N_2 seeding compared to non seeding phases.

Finally, the effect of an additional magnetic perturbation, MP, on the detachment process was studied. Detachment proceeds similarly with and without MP until the outer Φ_{D^+} rolls over. With MP, this roll over is followed by an abrupt and strong drop of Φ_{D^+} in the outer divertor, and by the disappearance of the radiative X-point fluctuations and the high density fronts in the inner far SOL and X-point region. Moreover, the detachment of the inner and outer divertor proceeds faster with MP.

6.2 Discussion

The observations, summarized above, gave rise to questions, for which possible theories will be discussed in the following.

Ion flux asymmetry Before the onset of detachment, in forward field, the ratio of the total ion flux reaching the inner and outer divertor is asymmetric and in favour of the inner divertor ($\Phi^{in}_{D^+}/\Phi^{out}_{D^+} = 1.9$). When the field direction is changed, this ratio is still asymmetric but now being in favour of the outer divertor ($\Phi^{out}_{D^+}/\Phi^{in}_{D^+} = 3.5$). A possible explanation of this, as proposed in [43], is the combination of the radial drift, Γ^{dr}_r, and the poloidal drift in the private flux region (PF), Γ^{dr}_Θ, induced by $\vec{E} \times \vec{B}$ forces (sec. 2.3.2). In forward field, Γ^{dr}_r is directed from the outer SOL across the separatrix into the PF and from the PF into the inner SOL (Fig. 2.2b). The poloidal drift flow, Γ^{dr}_Θ, in the PF is directed from the outer to the inner divertor (Fig. 2.2a). For similar conditions, such a flow in the PF has been measured in JT-60U [87] and ASDEX Upgrade [88] and was associated with Γ^{dr}_Θ. Thus, the combination of both Γ^{dr}_r and $E_r \times B$ in the private flux region brings more particles to the inner divertor in forward field and more particles to the outer divertor in reversed field and can explain these asymmetries.

Furthermore, the finally achieved DOD is, for both field directions, larger in the inner divertor. This is consistent, as these $\vec{E} \times \vec{B}$ drifts should become less important or even negligible at high densities (sec. 2.3.2). In addition, for both field directions the roll over of Φ_{D^+} happens first in the inner divertor. The ratio of the peripheral line integrated plasma density at the roll over in the inner and outer divertor is in reversed field $\bar{n}_{e,in}/\bar{n}_{e,out} \approx 2.1/2.5 = 0.84$. In forward field this ratio is $\bar{n}_{e,in}/\bar{n}_{e,out} \approx 1.5/3.3 = 0.76$. Taking the second roll over (see next point) in forward field, the ratio is $\bar{n}_{e,in}/\bar{n}_{e,out} \approx 2.9/3.3 = 0.88$, which is comparable to reversed field and indicates that

the influence of the $\vec{E} \times \vec{B}$ drifts became negligible.

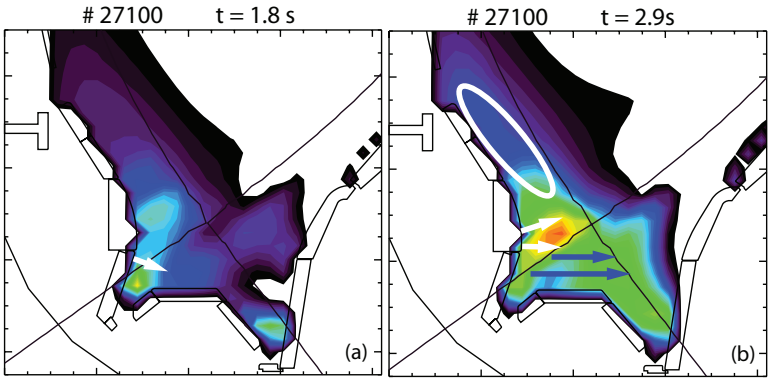

Figure 6.2: Total radiation distribution in the divertor for two different time points of #27100. See text for explanations.

The two roll overs in forward field In forward field, two roll overs of Γ_{D^+} are observed in the inner divertor strike point region, one at the onset state and one at the fluctuating detachment state.

A possible reason for the early first roll over followed by a second roll over in the inner divertor in forward field could be a geometric effect of the divertor structure. The lower tile of the inner divertor target is tilted towards the separatrix, i.e. the angle between the target normal and the horizontal axis is negative (white arrow in Fig. 6.2a). In the onset state the ion flux profile is radially not very broad, which is supported by the total radiation distribution (Fig. 6.2a). Recycled neutrals are released from the lower inner target and released in a $\cos^2$ distribution cone around the target normal, hence back to the strike point region (white arrow in Fig. 6.2a). This would enhance the neutral pressure in the inner strike point region, which increases the probability for CX-collisions to remove momentum, thus the ion flux would decrease, as observed. At the transition to the fluctuating state, a mechanism sets in which brings more particles to the far SOL, i.e. to the upper tile of the inner target (Fig. 6.2a). Once the ion fluxes to this upper tile are strong, and therefore recycling from this tile becomes strong, the situation should change. The upper tile curves backwards, i.e. the angle between the target normal and the horizontal axis becomes positive. If recycling takes place at this upper tile (high ion fluxes are measured in this region during the fluctuating state, confirmed by the radiation distribution Fig. 6.2b), neutrals will be released into regions further upstream (white arrows in Fig. 6.2b). This should change the divertor plasma conditions and could be the reason for the second increase and roll over of the ion flux in the inner divertor. In order to verify this theory, similar discharges can be made with different positions of the strike point. With a lower strike point, a higher density would be needed to push the ion flux to the upper tile of the inner divertor.

Most of the outer target, however, is constantly tilted away from the separatrix. In reversed field, Φ_{D^+} in the outer divertor[1] scales longer with the TPM compared to forward field, then rolls over and decreases continuously. No second roll over is observed, which is consistent with this divertor geometry model.

In the high density, high power H-mode, discussed in section 5.3.1, high densities, target ion fluxes and neutral fluxes are measured at the entrance of the inner divertor (indicated with the white circle in Fig. 6.2b) without N_2 seeding. Recycled neutrals originating from this target region should have a much higher probability to reach the main plasma, where they are ionized and cool the main plasma, than the neutrals which are released from the strike point area and mainly ionize in the SOL. With N_2 seeding, the high density region at the entrance of the inner divertor was measured to shrink, which should result in less recycled neutrals reaching the main plasma. This then could allow for higher pedestal temperatures, which where observed in improved H-Modes with N_2 seeding [83] and suggested to be the explanation for the increased confinement of improved H-Modes with N_2 seeding.

Flux enhancement The flux enhancement, which is defined here when the total ion flux is larger than the Two-Point-Model scaling, occurs in the outer divertor in forward field and in the inner divertor in reversed field. In forward field[2], during the fluctuating state, a high electron density is measured in the inner far SOL and X-point region, while the density in the strike point region is reduced (see the radiation distribution 6.2b as an indication). Recycled neutrals, originating from the strike point region, could therefore pass the inner SOL, the private flux region and reach the outer SOL. Namely, the inner divertor strike point region becomes transparent for neutrals (blue arrows in Fig. 6.2b). It has been shown previously at ASDEX Upgrade [89] that, under similar conditions, the inner divertor becomes transparent for neutrals and the neutral fluxes measured in the inner divertor and private flux region are equal. These neutrals, which reach the outer divertor SOL, will ionize there. This leads to additional radiation losses ($f_{pow} > 0$ in equation 2.25) in the outer SOL. As a consequence, the ion flux at the target increases (eq. 2.28), consistent with the observations. In addition, these ionized neutrals should provide an additional particle source in the outer SOL, resulting in a fraction of power being convected ($f_{conv} > 0$). This may explain the increase of the outer target temperature (eq. 2.26) during the flux enhancement phase, while the target ion flux and density also increase. In total, this would then be a combination, or competition, of the $f_{pow} > 0$ and $f_{conv} > 0$ effects.

[1] As in forward field the inner divertor receives the higher ion flux before the onset of detachment while in reversed field this is the outer divertor, these two cases are compared

[2] In the explanation for reversed field, the inner and outer divertor would simply change

Radiative X-point fluctuations Once the X-point fluctuations are triggered, a high electron density is measured at the X-point region. This indicates, that a certain fraction of recycled neutrals reaches the X-point and are ionized there, connected with the appearance of the fluctuations. Whether this is a necessary condition to trigger the fluctuations cannot, however, be proven here. But once the fluctuations are triggered, also a higher recycling is taking place at the upper tile of the inner divertor (white arrows in Fig. 6.2b). As mentioned before, recycled neutrals originating from the upper tile have a higher probability to reach the X-point than recycled neutrals coming from the strike point region. It was shown that, with N_2 seeding the frequency can be reduced and the necessary amount of injected N_2 depends on the heating power. As with power removal in the SOL due to N_2 seeding, a lower hydrogen recycling is needed to sustain the same target parameters (sec. 2.2.3) and a reduction of the ion flux to the upper tile of the inner divertor with N_2 seeding was measured. This indicates that there is a connection between the recycling taking place at the upper tile of the inner divertor and the radiative X-point fluctuations.

Furthermore, the frequency of the fluctuations depend on the square root of the mass of the fuelling species and the ion sound speed c_s is inversely proportional to the square of the mass (eq.2.7). One may assume that ions or filaments, originating at the X-point due to the ionization of recycled neutrals, flow with c_s from the X-point to the inner or outer target. An assumption of $T_i = T_e = 15\,\mathrm{eV}$ and $\alpha = 1$ gives $c_s \approx 38\,\mathrm{km/s}$. With the connection length from the inner X-point to the outer divertor along the SOL, $L_c \approx 84\,\mathrm{m}$, this yields a characteristic frequency of $f \approx 0.5\,\mathrm{kHz}$ which is by far too slow. The connection length to the inner divertor is $L_c \approx 15\,\mathrm{m}$, yielding a characteristic frequency of $f \approx 2.5\,\mathrm{kHz}$. This is still a factor of ≈ 2.5 too low but of the same order of magnitude and possibly within the uncertainties (The determination of L_c close to the X-point is uncertain due to the large flux expansion there). It cannot be verified, however, whether the density oscillates with the frequency of the fluctuations between the high density front at the X-point and the inner strike-point region, as the time resolution of the Stark broadening diagnostic and the Langmuir probes is too slow. New, or faster, diagnostics are therefore needed to gain more information on this topic.

Divertor plasma oscillations Finally at medium to high densities, with the heating power close to the L-H transition threshold, a situation occurs where the divertor plasma oscillates back and forth between the onset state and the fluctuating detachment state. A possible explanation of these oscillations is, that, although no H-mode is achieved, a better confinement is reached. This would lead to a better particle confinement of the main plasma, to a decrease of the upstream density and to the re-attachment of the inner divertor. This then may change the recycling properties of the inner divertor, which can influence the main plasma properties as discussed above. Thus the better confinement

is lost, the upstream density increases, the inner divertor detaches and a kind of limit cycle is established. This theory is rather speculative and should be verified with further experiments. A theory exists, however, which states that a minimum neutral density at the X-point is necessary to achieve the H-mode [90].

Moreover, the characteristics how the various plasma parameters oscillate are similar to those of the divertor plasma oscillations previously found at JET. It is therefore likely that the two states of the divertor plasma oscillations are the same for ASDEX Upgrade and JET. Furthermore, in JET high frequent sub oscillations (with respect to the frequency of the plasma oscillations) in the D_α signal were found during one state, as stated in [86]. Compared to the oscillations found here, this is the fluctuating detachment state where the radiative X-point fluctuations are observed. All together this is a strong hint that these divertor plasma oscillations are the same for AUG and JET. As a consequence, the onset and fluctuating detachment states should also have existed at JET. The experiments in JET where carried out with the Mk I divertor which was an open horizontal carbon divertor. The actual ASDEX Upgrade divertor is a closed vertical tungsten divertor. If theses states have existed in these JET experiments, then the presented classification of divertor detachment is independent of machine size, divertor geometry and divertor material. In order to confirm this, dedicated experiments at different machines need to be performed.

Chapter 7

Conclusions and outlook

The next-step fusion experiment, ITER, must rely on the divertor being detached in order to avoid damage on the divertor material. Therefore, an understanding of the detachment process is crucial. This thesis focuses on the experimental investigation of the process of divertor detachment.

Divertor detachment is achieved by a reduction of the temperature in the divertor via increasing the main plasma density or seeding of additional impurities. With a reduction of the temperature, volumetric processes such as charge exchange collisions and recombination become dominant. These processes lead to a strong reduction of the ion flux and plasma pressure in front of the divertor target. As a consequence, the region of high electron density is retracted from the target and a knowledge of the electron density distribution in the divertor volume is necessary to understand the detachment process.

The first part of this thesis was the installation and verification of a diagnostic determining the electron density in the divertor volume, which is based on the spectroscopic measurement of the Stark broadening of the Balmer lines. Initial problems with reflected stray-radiation have been solved and first measurements were successfully compared for consistency with other diagnostics, such as Langmuir probes and neutral pressure gauges. Thereby, neutral hydrogen fluxes in detached conditions have been evaluated from spectroscopy for the first time, yielding good agreement with neutral fluxes measured by the pressure gauges.

The detachment process was then, as the main part of this thesis, investigated with an extensive set of density ramp L-mode discharges with different heating powers, fuelling species and magnetic field directions. Usually, divertor detachment was studied by comparing upstream parameters, such as electron density and temperature, with target parameters, without having knowledge of the distribution of these parameters between the upstream region and the target. Furthermore, it was mainly focused on the outer divertor, because the outer divertor is the more crucial one in terms of power deposited on the target. In this thesis, emphasis was put on the evolution of the electron density

distribution in the divertor volume, and the detachment process was investigated in the inner and outer divertor simultaneously. This information was combined with all other available divertor diagnostics and a consistent picture of the detachment process was obtained.

The main result of this thesis is that a new classification of divertor detachment can be given. The detachment process is not continuously evolving but undergoes three different states, which are called the onset, the fluctuating and the complete detachment state. Within these states, the plasma conditions of the inner and outer divertor are strongly coupled, which was observed for the first time. During the fluctuating state, high frequent radiative fluctuations, combined with electron densities being one order of magnitude higher than the line averaged main plasma density, were found close to the X-point. This indicates that the recycling front of the inner divertor expands to the X-point, which may result in an unstable situation. In addition, high electron and ion flux densities develop close to the inner target far away from the strike point. This means that a mechanism sets in which leads to a strong increase of the radial transport in the inner divertor, maybe in combination with a change of the parallel transport. In order to investigate this further, diagnostics are needed which can measure the electron density and temperature with a sampling rate high enough to resolve the $\approx 5\,\mathrm{kHz}$ radiative X-point fluctuations and trace them back to the electron density and temperature. As a further outlook, it is of major interest to know whether the density or temperature at the inner or outer target and at the inner far SOL fluctuates according to the X-point fluctuations. This is necessary in order to gain more information on the radial and parallel transport in the inner divertor X-point region.

Another important result is that the inner divertor, once it is in the fluctuating state, influences the outer divertor. The inner divertor becomes transparent for neutrals which are recycled close to the strike point. These neutrals reach the outer divertor, are ionised there, cool the outer divertor plasma and drive the outer divertor detachment. Present day simulation codes cannot reproduce this measured broad distribution of the electron density or the X-point fluctuations in the inner divertor. As a consequence, these codes will not be able to simulate the conditions of the outer divertor during the fluctuating and complete detachment state in agreement with the experiment, as these are enforced by the conditions in the inner divertor. In order to simulate in the future divertor detachment correctly and to make predictions for ITER, the physical origin of the increased radial transport and of the radiative X-point fluctuations in the inner divertor has to be understood.

Once, with increasing density, the radiative X-point fluctuations disappear, both the inner and outer divertor plasma start to completely detach at the strike point region. Complete detachment is defined in this thesis when, besides the ion flux and the electron density at the target, the electron density in the divertor volume at the target region is

reduced to very low values. The fact that complete detachment occurs simultaneously in the inner and outer divertor was observed for the first time.

Furthermore it was found that, by puffing additional N_2 into the divertor plasma during the fluctuating state, the frequency of the fluctuations and the value as well as the spatial extent of the high density in the inner divertor volume are reduced. The reduction of the high density region changes the recycling distribution at the target. This may allow for an explanation of the higher pedestal temperatures, which were observed during high density, high power H-mode discharges with N_2 seeding. Therefore, the detached divertor plasma could influence the confined plasma. This would be of interest with respect to ITER, as it will be operated with the divertor being in the detached regime.

Although this thesis focused on ohmic and L-mode discharges, indications were found that the presented classification of divertor detachment is also valid for H-mode discharges as well as for other machines. In order to verify this, dedicated experiments at different machines need to be carried out.

Finally, this classification of divertor detachment, obtained within this thesis, provides a very good experimental basis for this complex field in plasma physics. Based on this, existing theories can be tested and improved, or new models, describing divertor detachment, can be developed.

Bibliography

[1] M. Kaufmann. *Plasmaphysik und Fusionsforschung*. B. G. Teubner GmbH, 2003.

[2] F. Troyon, R. Gruber, H. Saurenmann, S. Semenzato, and S. Succi. MHD-Limits to plasma confinement. *Plasma Phys. Control. Fusion*, 26(1A):209–215, 1984. URL http://dx.doi.org/10.1088/0741-3335/26/1A/319.

[3] The ITER Project. URL http://www.iter.org.

[4] F. Wagner. Regime of improved confinement and high beta in neutral-beam-heated divertor discharges of the ASDEX Tokamak. *Phys. Rev. Lett.*, 49:1408–1412, 1982. URL http://dx.doi.org/10.1103/PhysRevLett.49.1408.

[5] Y.R. Martin, Takizuka T., and the ITPA CDBM H-mode Threshold Database Working Group. Power requirement for accessing the H-mode in ITER. *Journal of Physics: Conference Series*, 123(1):012033, 2008. URL http://dx.doi.org/10.1088/1742-6596/123/1/012033.

[6] H. Zohm. Edge localized modes (ELMs). *Plasma Phys. Control. Fusion*, 38:105–128, 1996. URL http://dx.doi.org/10.1088/0741-3335/38/2/001.

[7] ITER Physics Basis. Chapter 4: Power and particle control. *Nucl. Fusion*, 39:2391, 1999. URL http://dx.doi.org/10.1088/0029-5515/39/12/304.

[8] M. Wischmeier, M. Groth, S. Wiesen, S. Potzel, L. Aho-Mantila, D.P. Coster, R. Dux, C. Fuchs, A. Kallenbach, H.W. Müller, D. Reiter, A. Scarabosio, and the ASDEX Upgrade Team. Assessment of edge modeling in support of ITER. *J. Nucl. Mater.*, 415:S523–S529, 2011. URL http://dx.doi.org/10.1016/j.jnucmat.2011.02.020.

[9] P.C. Stangeby. *The Plasma Boundary of Magnetic Fusion Devices*. Institute of Physics Publishing Bristol and Philadelphia, 2000.

[10] C.S. Pitcher and P.C. Stangeby. Experimental divertor physics. *Plasma Phys. Control. Fusion*, 39:779–930, 1997. URL http://dx.doi.org/10.1088/0741-3335/39/6/001.

[11] R. Schneider, X. Bonnin, K. Borras, D. Coster, H. Kastelewicz, D. Reiter, V.A. Rozhansky, and J. Braams. Plasma edge physics with B2-Eirene. *Contrib. Plasma Phys.*, 46:3–191, 2006. URL http://dx.doi.org/10.1002/ctpp.200610001.

[12] K.U. Riemann. Plasma-sheath transition and Bohm criterion. *Contrib. Plasma Phys.*, 32(3–4):231–236, 1992. URL http://dx.doi.org/10.1002/ctpp.2150320309.

[13] D. Bohm. *The Characteristics of electrical discharges in magnetic fields*. McGraw-Hill Book Company, 1949.

[14] I. Langmuir. The interaction of electron and positive ion space charges in cathode sheaths. *Phys. Rev.*, 33:954–989, 1929. URL http://dx.doi.org/10.1103/PhysRev.33.954.

[15] R. Chodura. *Physics of plasma-wall interactions in controlled fusion*. Plenum Press, 1999.

[16] A. Herrmann, M. Laux, D. Coster, J. Neuhauser, D. Reiter, R. Schneider, M. Weinlich, and the ASDEX-Upgrade Team. Energy transport to the divertor plates of ASDEX-Upgrade during ELMy H-mode phases. *J. Nucl. Mater.*, 220–222:543–547, 1995. URL http://dx.doi.org/10.1016/0022-3115(94)00536-2.

[17] J. Marki, R.A. Pitts, T. Eich, A. Herrmann, J. Horacek, F. Sanchez, and G. Veres. Sheath heat transmission factors on TCV. *J. Nucl. Mater.*, 363–365:382–288, 2007. URL http://dx.doi.org/10.1016/j.jnucmat.2007.01.197.

[18] S.I. Braginskii. *Reviews of Plasma Physics*. Consultants Bureau, 1965.

[19] L. Spitzer and R. Härm. Transport phenomena in a completely ionized gas. *Phys. Rev.*, 89:977–981, 1953. URL http://dx.doi.org/10.1103/PhysRev.89.977.

[20] F. Wagner and K. Lackner. Physics of plasma-wall interactions in controlled fusion. In D.E. Post and R. Behrisch, editors, *Proceedings of the NATO Advanced Study Institute*, volume 131 of *Series B: Physics*. Plenum Press, New York, 1986.

[21] Keilhacker. *Plasma Physics and Controlled Nuclear Fusion Research*, III:183, 1982.

[22] P.C. Stangeby. Can detached divertor plasmas be explained as self-sustained gas targets? *Nucl. Fusion*, 33:1695, 1993. URL http://dx.doi.org/10.1088/0029-5515/33/11/I10.

[23] K. Borrass, D. Coster, D. Reiter, and R. Schneider. Study of recombining gas targets. *J. Nucl. Mater.*, 241–243:250–254, 1997. URL http://dx.doi.org/10.1016/S0022-3115(97)80044-X.

[24] S.I. Krasheninnikov. Physical mechanisms in divertors and their impact on the core. *Czech. J. Phys.*, 48(S2):97–112, 1998.

[25] J. Wesson. *Tokamaks*. Clarendon Press, 1997.

[26] R.J. Goldston and P.H. Rutherford. *Introduction to Plasma Physics*. Bristol: Institute of Physics Publishing, 1997.

[27] B. LaBombard and M.V. Umansky. Cross-field plasma transport and main-chamber recycling in diverted plasmas on Alcator C-Mod. *Nucl. Fusion*, 40:2041–2060, 2000. URL http://dx.doi.org/10.1088/0029-5515/40/12/308.

[28] G.D. Porter, S.L. Allen, M. Brown, M.E. Fenstermacher, and D.N. Hill. Simulation of exerimentally achieved DIII-D detached plasmas using the UEDGE code. *Phys. Plasmas*, 3:1967–1975, 1996. URL http://dx.doi.org/10.1063/1.871993.

[29] A. Loarte. Understanding the edge physics of divertor experiments by comparison of 2D edge code calculations and experimental measurements. *J. Nucl. Mater.*, 241–243:118–134, 1997. URL http://dx.doi.org/10.1016/S0022-3115(97)80037-2.

[30] R. Schneider, D. Reiter, H.P. Zehrfeld, B. Braams, M. Baelmans, J. Geiger, H. Kastelewicz, J. Neuhauser, and R. Wunderlich. B2-Eirene simulations of ASDEX and ASDEX-Upgrade scrape-off layer plasmas. *J. Nucl. Mater.*, 196–198: 810–815, 1992. URL http://dx.doi.org/10.1016/S0022-3115(06)80147-9.

[31] S.I. Krasheninnikov. On scrape off layer plasma transport. *Physics Letters A*, 283: 368, 2001.

[32] J.A. Bodeo, D. Rudakov, R. Moyer, S. Krasheninnikov, D. Whyte, G. McKee, G. Tynan, M. Schaffer, P. Stangeby, P. West, S. Allen, T. Evans, R. Fonck, E. Hollmann, A. Leonard, A. Mahdavi, G. Porter, M. Tillack, and G. Antar. Transport by intermittent convection in the boundary of the DIII-D tokamak. *Phys. Plasmas*, 8: 4826, 2001. URL http://dx.doi.org/10.1063/1.1406940.

[33] P.C. Stangeby and A.V. Chankin. Simple models for the radial and poloidal $E \times B$ drifts in the scrape-off layer of a divertor tokamak: Effects on in/out asymmetries. *Nucl. Fusion*, 36:839–852, 1996. URL http://dx.doi.org/10.1088/0029-5515/36/7/I02.

[34] A.V. Chankin, D.P. Coster, N. Asakura, G. Corrigan, S.K. Erents, W. Fundamenski, H.W. Müller, R.A. Pitts, P.C. Stangeby, and M. Wischmeier. A possible role of radial electric field in driving parallel ion flow in scrape-off layer of divertor tokamaks. *Nucl. Fusion*, 47:762–772, 2007. URL http://dx.doi.org/10.1088/0029-5515/47/8/006.

[35] S.I. Krasheninnikov. Reverse flow and parameter profiles in a dense tokamak divertor plasma. *Nucl. Fusion*, 32:1927–1934, 1992. URL http://dx.doi.org/10.1088/0029-5515/32/11/I04.

[36] A. Loarte. Effects of divertor geometry on tokamak plasmas. *Plasma Phys. Control. Fusion*, 43:R183–R224, 2001. URL http://dx.doi.org/10.1088/0741-3335/43/6/201.

[37] B. LaBombard, J.A. Goetz, and I. Hutchinson. Experimental investigation of transport phenomena in the scrape-off layer and divertor. *J. Nucl. Mater.*, 241–243: 149–166, 1997. URL http://dx.doi.org/10.1016/S0022-3115(97)80037-2.

[38] A.V. Chankin, D.P. Coster, G. Corrigan, S.K. Erents, W. Fundamenski, A. Kallenbach, K. Lackner, J. Neuhauser, R. Pitts, the ASDEX Upgrade Team, and JET-EFDA Contributors. Fluid code simulations of radial electric field in the scrape-off layer of JET. *Plasma Phys. Control. Fusion*, 51:065022, 2009. URL http://dx.doi.org/10.1088/0741-3335/51/6/065022.

[39] A.W. Leonard, C.J. Lasnier, J.W. Cuthbertson, T.E. Evans, M.E. Fenstermacher, N. Hill, D, R.A. Jong, W.H. Meyer, T.W. Petrie, and G.D. Porter. Power balance in DIII-D during single-null ELMing H-mode plasmas. *J. Nucl. Mater.*, 220–222: 325–329, 1995. URL http://dx.doi.org/10.1016/0022-3115(94)00495-1.

[40] A.V. Chankin, D.J. Campell, S. Clement, S.J. Davies, L.D. Horton, J. Lingertat, A. Loarte, G.F. Matthews, R.D. Monk, R. Reichle, G. Saibene, M. Stamp, and P.C. Stangeby. Toroidal field reversal effects on divertor asymmetries in JET. *Plasma Phys. Control. Fusion*, 38:1579–1592, 1996. URL http://dx.doi.org/10.1088/0741-3335/38/9/001.

[41] G.M. Staebler. The critical point for the onset of divertor energy flux asymmetry in tokamaks. *Nucl. Fusion*, 36:1437–1453, 1996. URL http://dx.doi.org/10.1088/0029-5515/36/11/I01.

[42] M. Shimada and T. Ohkawa. Effect of gyro-motion of incident ions on inboard-outboard asymmetry in divertor plasmas. *J. Nucl. Mater.*, 266–269:906–910, 1999. URL http://dx.doi.org/10.1016/S0022-3115(98)00679-5.

[43] R.A. Pitts. Edge and divertor physics with reversed toroidal field in JET. *J. Nucl. Mater.*, 337–339:146–153, 2005. URL http://dx.doi.org/10.1016/j.jnucmat.2004.10.111.

[44] A. Huber. The effect of field reversal on the JET MkIIGB-SRP divertor performance in L-mode density limit discharges. *J. Nucl. Mater.*, 337–339:241–245, 2005. URL http://dx.doi.org/10.1016/j.jnucmat.2004.10.123.

[45] M. Groth, J.A. Boedo, N.H. Brooks, R.C. Isler, A.W. Leonard, G.D. Porter, J.G. Watkins, W.P. West, B.D. Bray, M.E. Fenstermacher, R.J. Groebner, R.A. Moyer, D.L. Rudakov, J.H. Yu, and L. Zeng. Effect of cross-field drifts on flows in the main scrape-off-layer of DIII-D L-mode plasmas. *Nucl. Fusion*, 49(11):115002, 2009. URL http://dx.doi.org/10.1088/0029-5515/49/11/115002.

[46] S.K. Erents, R.A. Pitts, W. Fundamenski, J.P. Gunn, and G.F. Matthews. A comparison of experimental measurements and code results to determine flows in the JET SOL. *Plasma Phys. Control. Fusion*, 46(11):1757, 2004. URL http://dx.doi.org/10.1088/0741-3335/46/11/006.

[47] W. Fundamenski. *Power Exhaust in Fusion Plasmas*. Cambridge University Press, 2010.

[48] J.A. Boedo, D. Rudakov, and R. Moyer. Transport by intermittent convection in the boundary of the DIII-D tokamak. *Phys. Plasmas*, 8:4826–4834, 2001. URL http://dx.doi.org/10.1063/1.1406940.

[49] J.P. Graves, J. Horacek, R.A. Pitts, and K.I. Hopcraft. Self-similar density turbulence in the TCV tokamak scrape-off layer. *Plasma Phys. Control. Fusion*, 47: L1–L9, 2005. URL http://dx.doi.org/10.1088/0741-3335/47/3/L01.

[50] S. Wiesen, W. Fundamenski, M. Wischmeier, M. Groth, S. Brezinsek, V. Naulin, and JET EFDA contributors. Relevance of collisionality in the transport model assumptions for divertor detachment multi-fluid modelling on JET. *J. Nucl. Mater.*, 415: S535–S539, 2011. URL http://dx.doi.org/10.1016/j.jnucmat.2010.12.010.

[51] D.R. Bates, A.E. Kingston, and R.W.P. McWhirter. Recombination between electrons and atomic ions. I. Optically thin plasmas. *Proc. R. Soc. A*, 267(1330):297–312, 1962.

[52] R.W.P. McWhirter and H.P. Summers. Atomic radiation from low density plasmas. *Applied Atomic Collision Physics Vol 2: Fusion*, chapter 3:52, 1984.

[53] H.P. Summers, W.J. Dickson, M.G. O'Mullane, N.R. Badnell, A.D. Whiteford, D.H. Brooks, J. Lang, S.D. Loch, and D.C. Griffin. Ionization state, excited populations and emission of impurities in dynamic finite density plasmas: I. The generalized collisional-radiative model for light elements. *Plasma Phys. Control. Fusion*, 48(2): 263, 2006. URL http://dx.doi.org/10.1088/0741-3335/48/2/007.

[54] The ADAS Project. URL http://www.adas.ac.uk/.

[55] O. Schmitz, I.L. Beigman, L.A. Vainshtein, B. Schweer, M. Kantor, A. Pospieszczyk, Y. Xu, M. Krychowiak, M. Lehnen, U. Samm, B. Unterberg, and the TEXTOR team. Status of electron temperature and density measurement with beam emission spectroscopy on thermal helium at TEXTOR. *Plasma Phys. Control. Fusion*, 50(11):115004, 2008. URL `http://dx.doi.org/10.1088/0741-3335/50/11/115004`.

[56] K. Behringer, H. P. Summers, B. Denne, M. Forrest, and M. Stamp. Spectroscopic determination of impurity influx from localized surfaces. *Plasma Phys. Control. Fusion*, 31:2059–2099, 1989.

[57] S. Potzel. *Bestimmung der Elektronendichte im Divertorplasma mittels Starkverbreiterung der Balmerlinien.* Diplomarbeit, Universität Bayreuth, Januar 2009.

[58] S. Potzel, R. Dux, H.W. Müller, A. Scarabosio, M. Wischmeier, and the ASDEX Upgrade Team. Electron density measurements in detached divertor plasmas of ASDEX Upgrade via Stark broadening of the Balmer lines. In A. Becoulet, T. Hoang, and U. Stroth, editors, *Europhysics Conference Abstracts (CD-ROM, Proc. of the 38th EPS Conference on Plasma Physics, Strasbourg, France, 2011)*, volume 35G of *ECA*, page O2.303. European Physical Society, Geneva, 2011. URL `http://ocs.ciemat.es/EPS2011PAP/pdf/O2.303.pdf`.

[59] A. Unsöld. *Physik der Sternatmosphären.* Springer-Verlag, 1955.

[60] T. Holstein. Pressure broadening of spectral lines. *Phys. Rev.*, 79:744, 1950.

[61] H.R. Griem. *Plasma Spectroscopy.* McGraw-Hill Book Company, 1997.

[62] M. Baranger. Atomic and molecular processes. *Academic Press Inc.*, Kapitel 13 in D.R. Bates, 1962.

[63] Nguyen-Hoe, H.W. Drawin, and L. Herman. Effet d'un champ magnetique uniforme sur les profiles des raies de l'hydrogene. *J. Quant. Spectrosc. Radiat. Transfer*, 7: 429–474, 1967.

[64] E. Schrödinger. Quantisierung als Eigenwertproblem. *Annalen der Physik*, 80:437–490, 1926.

[65] J. Holtsmark. Über die Verbreiterung von Spektrallinien. *Annalen der Physik*, 58: 577–630, 1919.

[66] B. Mozer and M. Baranger. Electric field distribution in an ionized gas I. *Physical Review*, 115:521–531, 1959.

[67] B. Mozer and M. Baranger. Electric field distribution in an ionized gas II. *Physical Review*, 118:626–631, 1960.

[68] A. Brissaud and U. Frisch. Theory of Stark broadening II - exact line profile with Model Microfield. *J. Quant. Spectrosc. Radiat. Transfer*, 11:1767–1783, 1971.

[69] J. Seidel. Hydrogen stark broadening by different kinds of Model Microfields. *Z. Naturforsch.*, 35a:679–689, 1980.

[70] A. Brissaud and U. Frisch. Solving linear stochastic differential equations. *J. Math. Phys.*, 15:524–534, 1974.

[71] A. Brissaud, C. Goldbach, L. Leorat, A. Mazure, and G. Nollez. On the validity of the Model Microfield Method as applied to Stark broadening of neutral lines. *J. Phys. B: At. Mol. Phys.*, 9:1147–1162, 1976.

[72] C. Stehlé. Stark broadening of hydrogen Lyman and Balmer in the conditions of stellar envelopes. *Astron. Astrophys. SuppL. Ser.*, 104:509–527, 1994.

[73] C. Stehlé and R. Hutcheon. Extensive tabulations of stark broadened hydrogen line profiles. *Astron. Astrophys. SuppL. Ser.*, 140:93–97, 1999.

[74] R. Neu, V. Bobkov, R. Dux, J. C. Fuchs, O. Gruber, A. Herrmann, A. Kallenbach, H. Maier, M. Mayer, T. Pütterich, V. Rohde, A.C.C. Sips, J. Stober, K. Sugiyama, and the ASDEX Upgrade Team. Ten years of W programme in ASDEX Upgrade - challenges and conclusions. *Phys. Scr.*, T138:014038 (6pp), 2009. URL `http://dx.doi.org/10.1088/0031-8949/2009/T138/014038`.

[75] J. Harhausen, A. Kallenbach, C. Fuchs, and the ASDEX Upgrade Team. Interpretation of D_α video diagnostics data as a contribution to plasma edge characterization. *Plasma Phys. Control. Fusion*, 53:025002, 2011. URL `http://dx.doi.org/10.1088/0741-3335/53/2/025002`.

[76] G.M. McCracken, R.D. Monk, A. Meigs, L. Horton, L.C. Ingesson, J. Lingertat, G.F. Matthews, M.G. O'Mullane, R. Prentice, M.F. Stamp, and P.C. Stangeby. Volume recombination and detachment in JET divertor plasmas. *J. Nucl. Mater.*, 266–269:37–43, 1999.

[77] A. Scarabosio and G. Haas. Behaviour of the ASDEX pressure gauge at high neutral gas pressure and applications for ITER. *AIP Conference Proceedings*, 988(1):238–242, 2008. URL `http://dx.doi.org/10.1063/1.2905075`.

[78] B. Reiter, G. Pautasso, T. Eich, J.C. Fuchs, L. Giannone, R. Dux, J. Neuhauser, M. Maraschek, V. Igochine, A. Herrmann, T. Lunt, and the ASDEX Upgrade Team.

Application of AXUV Diodes for broad-band plasma radiation studies in ASDEX Upgrade. In M Mateev and E Benova, editors, *Europhysics Conference Abstracts (CD-ROM, Proc. of the 36th EPS Conference on Plasma Physics, Sofia, Bulgaria, 2009)*, volume 33E of *ECA*, pages P–1.161. European Physical Society, Geneva, 2009. URL http://epsppd.epfl.ch/Sofia/pdf/P1_161.pdf.

[79] A. Loarte. Plasma detachment in JET Mark I divertor experiments. *Nucl. Fusion*, 38:331, 1998.

[80] G.D. Porter, S. Davies, B. LaBombard, A. Loarte, K. McCormick, R. Monk, M. Shimada, and M. Sugihara. Analysis of separatrix plasma parameters using local and multi-machine databases. *J. Nucl. Mater.*, 266–269:917–921, 1999. URL http://dx.doi.org/10.1016/S0022-3115(98)00621-7.

[81] A. Kallenbach, R. Dux, J.C. Fuchs, R. Fischer, B. Geiger, L. Giannone, A. Herrmann, T. Lunt, V. Mertens, R. McDermott, R. Neu, T. Pütterich, S. Rathgeber, V. Rohde, K. Schmid, J. Schweinzer, W. Treutterer, and the ASDEX Upgrade Team. Divertor power load feedback with nitrogen seeding in ASDEX Upgrade. *Plasma Phys. Control. Fusion*, 52:055002, 2010. URL http://dx.doi.org/10.1088/0741-3335/52/5/055002.

[82] O. Gruber, A.C.C. Sips, R. Dux, T. Eich, J.C. Fuchs, A. Herrmann, A. Kallenbach, C.F. Maggi, R. Neu, T. Pütterich, J. Schweinzer, J. Stober, and the ASDEX Upgrade Team. Compatibility of ITER scenarios with full tungsten wall in ASDEX Upgrade. *Nucl. Fusion*, 49:115014, 2009. URL http://dx.doi.org/10.1088/0029-5515/49/11/115014.

[83] J. Schweinzer, A.C.C. Sips, G. Tardini, P.A. Schneider, R. Fischer, J.C. Fuchs, O. Gruber, J. Hobirk, A. Kallenbach, R.M. McDermott, R. Neu, T. Pütterich, S.K. Rathgeber, J. Stober, J. Vicente, and the ASDEX Upgrade Team. Confinement of 'improved H-modes' in the all-tungsten ASDEX Upgrade with nitrogen seeding. *Nucl. Fusion*, 51:113003, 2011. URL http://dx.doi.org/10.1088/0029-5515/51/11/113003.

[84] K. McCormick, R. Dux, R. Fischer, A. Scarabosio, and the ASDEX Upgrade Team. Main chamber high recycling on ASDEX Upgrade. *J. Nucl. Mater.*, 390–391:465–469, 2009. URL http://dx.doi.org/10.1016/j.jnucmat.2009.01.145.

[85] W. Suttrop, O. Gruber, S. Günter, D. Hahn, A. Herrmann, M. Rott, T. Vierle, U. Seidel, M. Sempf, B. Streibl, E. Strumberger, D. Yadikin, O. Neubauer, B. Unterberg, E. Gaio, V. Toigo, P. Brunsell, and the ASDEX Upgrade Team. In-vessel saddle coils for MHD control in ASDEX Upgrade. *Fusion Eng. and Des.*, 84(2-6): 290–294, 2009. URL http://dx.doi.org/10.1016/j.fusengdes.2008.12.044.

[86] A. Loarte, R.D. Monk, A.S. , Kukushkin, E. Righi, D.J. Campbell, G.D. Conway, and C.F. Maggi. Self-sustained divertor plasma oscillations in the JET Tokamak. *Phys. Rev. Lett.*, 83:3657, 1999. URL http://dx.doi.org/10.1103/PhysRevLett.83.3657.

[87] N. Asakura, H. Takenaga, S. Sakurai, G.D. Porter, T.D. Rognlien, M.E. Rensink, K. Shimizu, S. Higashijima, and H. Kubo. Driving mechanism of sol plasma flow and effects on the divertor performance in JT-60U. *Nucl. Fusion*, 44:503–512, 2004. URL http://dx.doi.org/10.1088/0029-5515/44/4/004.

[88] M. Tsalas, A. Herrmann, A. Kallenbach, H.W. Müller, J. Neuhauser, V. Rhode, N. Tsois, M. Wischmeier, and the ASDEX Upgrade Team. Divertor plasma flow near the lower X-point in ASDEX Upgrade. *Plasma Phys. Control. Fusion*, 49: 857–872, 2007. URL http://dx.doi.org/10.1088/0741-3335/49/6/012.

[89] A. Scarabosio, G. Haas, H. W. Müller, R. Pugno, M. Wischmeier, and the ASDEX Upgrade Team. Measurements of neutral gas fluxes under different plasma and divertor regimes in ASDEX Upgrade. *J. Nucl. Mater.*, 390–391:494–497, 2009. URL http://dx.doi.org/10.1016/j.jnucmat.2009.01.057.

[90] S. Toda, S.I. Itoh, M. Yagi, and Y. Miura. A theoretical model of H-mode transition triggered by condensed neutrals near X-point. *Plasma Phys. Control. Fusion*, 39 (2):301, 1997. URL http://dx.doi.org/10.1088/0741-3335/39/2/007.

Acknowledgements

The work presented here would not have been possible without the help and motivation of many colleagues of the ASDEX Upgrade team, not least through the significant support of the people I do thankfully acknowledge in the following.

First of all my sincere thank is owed to Prof. M. Kaufmann for giving me the opportunity to perform this thesis at the IPP under his academic supervision. I also want to thank Prof. A. Peeters for his considerate willingness to judge my work.

My special gratitude goes to my advisors Dr. M. Wischmeier and Dr. A. Scarabosio who guided me through the challenges of my work. With their continuous encouragement, dedication and consolidated knowledge about SOL physics they were always available to give advice.

I extend my deepest thanks to my group leader Dr. R. Dux who introduced me to the world of spectroscopy and has always been willing to answer each and every one of my questions.

I am very grateful to Dr. H.W. Müller who was in charge of the Langmuir probes and evaluating the probe data.

I thank M. Bernert for operating the AXUV diodes and for the valuable discussions on tomographic reconstructions and fluctuations.

For the development and maintenance of the SBD diagnostic and the in-vessel work, I am indebted to the Gefässmannschaft, in particular M. Ebner and F. Springer, and especially to our spectroscopy group technician A. Mayer.

I am also grateful to Prof. A. Kallenbach, Dr. W. Suttrop and Dr. C. Fuchs for fruitful discussions and helpful comments.

For the proof-reading of the manuscript a special thank goes to M. Dunne and Dr. R. McDermott.

I also want to thank my room mates S. Fietz, B. Geiger, P. de Marné, P.A. Schneider, the daily visitors J. Boom, I. Classen, M. Willensdorfer, E. Viezzer, C. Vorpahl and the Skat crew T. Happel and P. Sauter for creating a nice atmosphere and having interesting, not only scientific, discussions.